Spectroscopic Investigation of Novel Optogenetic Tools

Dissertation
zur Erlangung des Grades eines
Doktors der Naturwissenschaften (Dr. rer. nat.)
im Fachbereich Physik der Freien Universität Berlin

vorgelegt von
Silke Kerruth

Berlin 2014

Erster Gutachter: Prof. Dr. Joachim Heberle
Zweiter Gutachter: Prof. Dr. Enrica Bordignon

Tag der Dissputation: 13. November 2014

Die vorliegende Arbeit wurde in der Arbeitsgruppe von Prof. Dr. Joachim Heberle am Fachbereich Physik der Freien Universität Berlin durchgeführt.

Das Projekt wurde im Rahmen der Forschergruppe 1279 “Protein-based Photoswitches as optogenetic tools” durch die Deutsche Forschungsgemeinschaft gefördert.

Parts of this work were already published:

S. Kerruth, K. Ataka, D. Frey, I. Schlichting and J. Heberle.
Aureochrome 1 illuminated: Structural changes of a transcription factor probed by molecular spectroscopy. *PLOS one*, 2014, Vol. 9, e103307. DOI:10.1371/journal.pone.0103307.g001

Abstract

Optogenetics is a fairly young scientific field that uses the expression of light-sensitive proteins in particular cell types, referred to as optogenetic tools, to modulate their response by light.
In this work two different optogenetic tools were investigated. The transmembrane protein KcsA was converted to an artificial light-gated ion channel by an azobenzene photoswitch that carried a tetraethyl ammonium group blocking the ion flow. Interactions of KcsA with different types of photoswitches were investigated by thermophoresis, surface-enhanced infrared absorption spectroscopy (SEIRAS), and impedance spectroscopy. Microscale thermophoresis (MST) indicated low affinity of KcsA to the majority of probed photoswitches. Thus, a maleimide-labeled azobenzene (MAQ) was bound covalently to the P55C variant of KcsA. Surface-enhanced infrared spectroscopy indicated the successful establishment of a tethered KcsA P55C monolayer reconstituted into lipids. However, impedance spectroscopy did not confirmed the closing and opening of the KcsA channel mediated by the MAQ, although vibrational changes where detected in the SEIRA spectrum. Thus, fast degeneration of the maleimide group probably prevented the reaction with the cysteine of the KcsA and did not lead to a functional artificial system.
In the second part of this work, the mechanisms of signal transduction of blue-light photoreceptors containing LOV domains were investigated. Aureochrome 1 from *Vaucheria frigida* acts as a blue-light activated transcription factor, while mPAC from *Microcoleus chthonoplastes* is a light activated adenylyl cyclase (AC). The kinetics of the photocycle intermediates LOV_{715}, which is a red-shifted triplet state, and the blue-shifted signaling state LOV_{390} were determined by time-resolved UV/Vis spectroscopy. In case of aureochrome 1 the presence of the bZIP domain was found to prolong the lifetime of the LOV_{390} signaling state as compared to the isolated LOV domain, while the binding of DNA did not influence the photocycle kinetics. For mPAC, lifetime of the triplet state was significantly shorter than all other reported LOV domains, while the decay of the adduct state was in the normal range.
The light-dark FTIR difference spectra indicated characteristic features of the flavin mononucleotide (FMN) chromophore. Furthermore, the S-H stretching vibration of the reactive cysteines involved in formation of the thio-adduct state have been detected. For aureochrome 1 the frequency was shifted to lower wavenumbers, while in mPAC this band was asymmetric, suggesting the presence of rotational isomers. Furthermore, mPAC showed a negative band that was attributed to an O-H stretch vibration of an amino acid side chain of the adenylyl cyclase domain, which is probably involved in dimerization of this domain.

The light-induced FTIR difference spectrum of aureochrome 1 in presence of its target DNA contained vibrations that were assigned to lysine, arginine and phosphate-backbone groups. Thus, a model of the binding complex was determined that shows the critical interactions between the transcription factor and the DNA molecule.

Zusammenfassung

In der Optogenetik werden Licht-sensitive Proteine in bestimmten Zellen exprimiert, um diese mit Hilfe von Licht zu manipulieren und zu untersuchen. Diese Proteine werden optogenetische Werkzeuge ("optogenetic tools´´) genannt.
In dieser Arbeit wurden diese Werkzeuge studiert. Der membranständige KcsA-Kanal wurde mit Hilfe eines Azobenzen-basierten Photoschalters in einen künstlichen Licht-sensitiven Ionenkanal verwandelt. Dabei wird der Ionenfluss durch eine Tetraethyl Ammoniumgruppe am Photoschalter geblockt. Die Interaktionen vom KcsA mit verschiedenen Photoschalter-Molekülen wurde mittels Thermophorese, oberflächenverstärkter Infrarot Spektroskopie (SEIRAS) und Impedanz Spektroskopie untersucht. Die Thermophoresemessungen ergaben dabei für die meisten Photoschalter eine geringe Affinität zum KcsA. Deshalb wurde in einem zweiten Ansatz mit MAQ ein alternatives Azobenzene Konjugat an die KcsA P55C Variante gebunden. MAQ enthält eine Maleimid-Gruppe, die eine kovalente Bindung mit dem Thiol des neueingeführten Cysteins eingeht. Im SEIRA Differenzspektrum wurden zwar Banden des Photoschalters detektiert, jedoch konnte durch Impedanz Spektroskopie das Öffnen und Blockieren des Kanals durch den Photoschalter in der Monolage aus Lipiden nicht nachgewiesen werden. Dies begründet sich wahrscheinlich in der schnellen Degeneration der Maleimidgruppe des MAQ wodurch eine Reaktion mit dem Cystein nicht mehr möglich ist.
Im zweiten Teil wurde die Signaltransduktion von Blaulichtrezeptoren, die eine LOV Domäne enthalten, untersucht. Aureochrome 1 aus *Vaucheria frigida* ist ein Blaulicht aktivierter Transkriptionsfaktor, während mPAC aus *Microcoleus chthonoplastes* als Licht-aktivierte Adenylyl Cyclase (AC) fungiert. Die Kinetiken der Photozyklus Intermediate LOV_{715}, welches einen rotverschobenen Triplett Zustand darstellt, und des blauverschobene Signalzustandes LOV_{390} wurden mittels Blitzlichtphotolyse bestimmt. Für Aureochrome 1 wurde gezeigt, dass die bZIP-Domäne die Lebenszeit des Signalzustandes verlängert, während die Bindung an die Ziel-DNA keinen Einfluss auf die Photozyklus-Kinetik hat. Für mPAC lag der Zerfall des Addukt Zustandes im normalen Bereich, jedoch war die Lebenszeit des Triplett Zustandes im Vergleich zu allen bekannten LOV-Proteinen um den Faktor 3 verkürzt.
Licht-Dunkel FT-IR Differenzspektren zeigten für Aureochrome 1 und mPAC die charakteristischen Banden des Flavin Mononukleotid (FMN) Chromophores. Außerdem konnten die S-H Streckschwingungen der reaktiven Cysteine detektiert werden, die im Addukt Zustand eine kovalente Binding mit dem FMN eingehen. Für Aureochrome 1 war die Frequenz dieser Bande zu niedrigeren Wellenzahlen verschoben, während sie in mPAC asymmetrisch war. Dies ist auf die Präsenz von Rotationsisomeren des Cysteins zurückzuführen.

Des Weiteren wurde im mPAC Spektrum eine charakteristische, negative Bande detektiert, die der O-H Streckschwingung einer alkoholischen Seitenkette der Adenylylcyclase Domäne zugeordnet werden kann. Dabei handelt es sich wahrscheinlich um ein Threonin oder Serin, das an der Dimerisierung dieser Domäne beteiligt ist. Das Licht-Dunkel FT-IR Differenzspektrum von Aureochrome 1 in Anwesenheit der Ziel-DNA enthielt für Lysin und Arginin, wie auch für das Phosphat-Rückgrat charakteristische Banden. Somit konnte ein Modell des Bindungskomplex erstellt werden, das die kritischen Interaktionen zwischen dem Transkriptionsfaktor und der DNA zeigt.

Contents

List of Figures

List of Abbreviations

AAQ acrylamide-azo-quarternary ammonium
AC adenylyl cylcases
ANTA Nα,Nα-bis(carboxymethyl)-*L*-lysine
APC diphosphomethylphosphonic acid adenosyl ester
ATP adenosine-5'-triphosphate
ATR attenuated total reflection
BHI brain heart infusion
BL blue-light
BLAST basic local alignment search tool
BLUF sensors of blue-light using FAD
bO bacterioopsin
bR bacteriorhodopsin
BzAQ Benzoyl-Azo-Quarternary ammonium
bZIP basic zipper
cAMP 3'-5'-cyclic adenosine monophoshate
ChR channelrhodopsin
DDM dodecylmaltoside
DMPC 1,2-dimyristoyl-sn-glycero-3-phosphocholine
DMSO dimethylsulfoxid
DNA deoxyribonucleic acid
DTSP 3',3-Dithio-bis(N-succinimidylpropionate)
DTT dithiothreitol
EDTA ethylenediaminetetraacetic acid
EPR electron paramagnetic resonance
FAD flavin adenine dinucleotide
FMN flavin mononucleotide
Fp forward primer
FTIR Fourier transform infrared
FWHM full width at half maximum
GAP GTPase activating protein
GCN4 General Control Protein 4
GPCR G-protein coupled receptor

GTP guanosine-5'-triphosphate
IPTG isopropyl-β-D-thiogalactopyranoside
IR infrared
ISC intersystem crossing
LED light-emitting diode
LOV light-, oxygen- and voltage-sensitive
MAQ maleimide-Azo-Quaternary ammonium
MSP membrane scaffold protein
MST microscale thermophoresis
ND nanodisc
Nd:YAG neodymium-doped yttrium aluminum garnet
NHS N-hydroxysuccinimide
Ni-NTA nickel nitrilotriacetic acid
NTA nitrilotriacetic acid
OG octyl glycoside
OPO optical parametric oscillator
PAC photoactivated adenylyl cyclase
PAS Per Arnt Sim
PBS phosphate buffered saline
PCR polymerase chain reaction
PMSF phenylmethanesulfonylfluoride
PMT photomultiplier
POPC 1-palmitoyl-2oleoyl-*syn*-glycero-3-phoshocholine
POPG 1-palmitoyl-2oleoyl-*syn*-glycero-3-phosho-(1'-*rac*-glycerol
OCP open circuit potential
OD optical density
Rp reverse primer
SAM self assambled monolayer
SDS sodium dodecyl sulfate
SEC size exclusion chromatography
SEIRA surface-enhanced infrared absorption
SEIRAS surface-enhanced infrared absorption spectroscopy
SERS surface-enhanced Raman scattering
SPARK synthetic photoisomerizable azobenzene-regulated K^+
STAS sulfate transporter anit-sigma factor agonist
TCEP tris(2-carboxyethyl)phosphine
TEA tetraethylammonium
TM transmembrane
Tris tris-(hydroxymethyl)-aminomethan
TSP thio-(N-succinimidylpropionate)
VVD Vivid, LOV protein from *Bacillus amyloliquefaciens*

Chapter 1

Optogenetics

In the beginning of the 21^{st} century a new method was introduced in neuroscience, Optogenetic - that uses the expression of light-sensitive proteins in particular cell types to modulate their response by light. Over the years this technique has found applications in a wide variety of scientific fields, culminating in being elected as the "Method of the Year" in 2010 by the Nature journals. Few important applications based on this technique includes the development of new optogenetic tools, methods to transfer the encoding DNA into target cells, methods for specific illumination and finally, suitable report systems to detect the responses of cells, tissue, and animal behavior [1].
Study of the selective activation of a specific cell type using optogenetic methods has four basic requirements. Firstly, a suitable tool is necessary. Secondly, this tool has to be transfered into the specific cells. The third step is to achieve a controlled illumination, while the final step is to readout the response. The last decade has witnessed a constant growth in the variety of optogenetic tools. The discovery of channelrhodopsin (ChR) 2 in 2003, a light-gated cation-selective ion channel, was the fundament of optogenetics [2]. Today there are several ways of manipulating cellular pathways by light. One way involves the application of chemical compounds such as caged ligands or photoswitches. While caged ligands are released by a light flash and then act as normal ligands that activate receptors on the cell surface, photoswitches modify membrane receptors or channels to make them light sensitive. Another group of optogenetic tools is enfold microbial rhodopsins. These rhodopsin related proteins carry retinal as a cofactor and work as ion pumps or ion channels. Thus channelrhodopsins can be used to depolarize neurons and firing action potentials, while pumps like halorhodopsin (Cl^--pump) and bacteriorhodopsin (H^+-pump) hyperpolarize neurons and therefore block them.
Other approaches combine light sensitive domains with reaction domains that initiate a reaction inside the cells. An example of a tool based on this approach is OptoXR, a fusion protein of rhodopsin with the intercellular domain of the β adreneric G-protein

coupled receptor (GPCR), is one of these tools. Water soluble photoreceptors like light-, oxygen- and voltage-sensitive (LOV) proteins, cryptochromes and phytochromes are used in optogenetics. Due to their tendency to dimerize they can be cloned to Rac domains, thereby activating the PAK1 signiling pathway. Finally, photoactivated adenylyl cyclase (PAC) that convert ATP into cAMP an important second messenger can be used to directly modulate cell signalling.
In optogenetics the neurons and cells that are observed are themselves producing the light-sensitive proteins. There are several existing methods by which the genes encoding for the proteins can be delivered. For example, the genes can be transfered into cells directly for example by electroporation. Viral transduction utilizes specific viruses to transfect specific types of cells. The cells are targeted by choosing proper casing proteins. For animal studies creation of transgenic animals is necessary. The expression of the optogenetic tool in selective cells then can be initiated with the help of suitable promotors.
Controlled illumination is assured by the use of ultrafast shutter with a continous light source, fast switching LEDs or one-photon laser scanning microscopy. These techniques ensure well-defined spatial and temporal resolution. The use of optical fibers and miniturized LEDs are also widely disposed. Finally the response is readout by electrodes or fluorescent biosensors or simply by behaviorial tests.
The area of application of optogenetic is constantly growing. It is the first method that allowed scientists to observe how neuros behave with each other or how neuronal networks are connected. Recent studies also illustrated other applications of optogenetics such as controlled “firing” of heart cells, cell movement and extensions, moving of proteins, and activating gene transcription [3].

Understanding the functioning of these light-sensitive proteins at a molecular level is vital for the development of new optogenetic tools, thus motivating the study of their reaction mechanisms using a variety of spectroscopic methods.

Chapter 2

Novel Optogenetic Tools

2.1 Blue-light receptors

The blue and ultraviolet light collectively represent the high energy end of the spectrum of radiation emitted by the sun. Thus, all species have developed proteins to recognize and react to these lights. These proteins are called blue-light (BL) receptors. Blue-light can be sensed by several types of chromophores such as retinal (channelrhodopsin II, sensory rhodopsin II), flavin mononucleotide (LOV proteins) and flavin adenine dinucleotide (BLUF proteins, cryptochromes). Especially organisms performing photosynthesis need to react to light to choose a suitable settlement habitat and orientation toward the optimal light intensity. In plants the photoreceptor used for phototropism is phototropin. This BL receptor is known to mediate, besides phototropism, opening of the stomatal for gas exchange, chloroplast movement for suitable alignment and also leaf flattening [4]. Algae that are living in a marine environment also exhibit BL receptors, like aureochromes.

2.1.1 LOV domain

The light-, oxygen- and voltage-sensitive (LOV) photoreceptors are widely distributed among prokaryotic and eukaryotic organisms. They are a subgroup of the Per Arnt Sim (PAS) superfamily and reveal the classical α,β fold, namely AβBβCαDαEαFαGβHβIβ [5]. The β scaffold is formed by a five-stranded antiparallel β-sheet that functions as an interface between the chromophore binding pocket and the environment. On one side it interacts directly with the flavin mononucleotide (FMN) cofactor, while the other side is either docked to helical regions (N-terminal cap and/or Jα-helix) or directly to the effector interface [6]. LOV domains are typically very small domains of about 100-110 amino acids.

For sensing blue-light they use oxidized FMN as a cofactor that is non-covalently bound inside the PAS fold (see fig.2.1). Flavin mononucelotide consists of an isoalloxazine ring attached on the N(10) position to ribitol, whose terminal alcohol group forms an ester with a phosphate (see fig. 2.1 right). The chromophore binding pocket is mostly hydrophobic around ring I, while O(4), N(3) and O(2) of ring III of the FMN are hydrogen bonded to amino acid side chains such as asparagines and glutamine, which are conserved among the LOV domains.

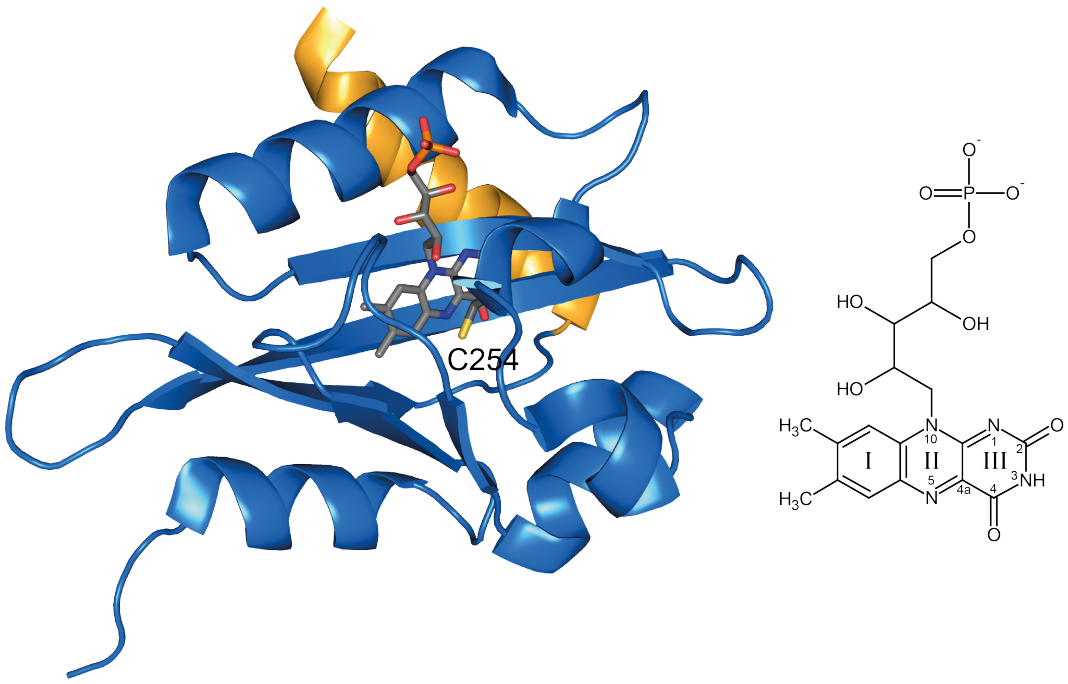

Figure 2.1: Left: Structure of the aureochrome 1 LOV domain [7]. The structure shows the typical PAS domain fold with the 5-fold β-sheet and α-helices. The α-helix in the back (colored in orange) is the Jα-helix that exhibits a special role in signal transduction towards the effector domain. The FMN cofactor and the reactive cysteine C254 are shown as sticks. Right: Chemical structure of the FMN cofactor with the nomenclature of the atoms in the isoallaxazine ring.

Photocycle of the LOV domain

In the ground state the FMN shows an absorption band around 447 nm with vibronic fine structure and is therefore called LOV_{447}. Absorption of a blue photon initiates the photocycle of the LOV domain (see fig.2.2). The FMN is excited to the S_1 state. From this state it converts within a few nanoseconds via intersystem crossing (ISC) into the triplet state, called LOV_{715} [8]. The quantum yield of triplet formation is similar to that of free FMN chromophore in solution at pH 7 and is about 0.6 [9]. The triplet species undergoes a reaction with the apoprotein during which a covalent bond between a nearby cysteine and the C(4a) atom of the isoallaxazine ring is formed. The resulting intermediate is called adduct intermediate or LOV_{390} due to its absorption maximum at 390 nm.

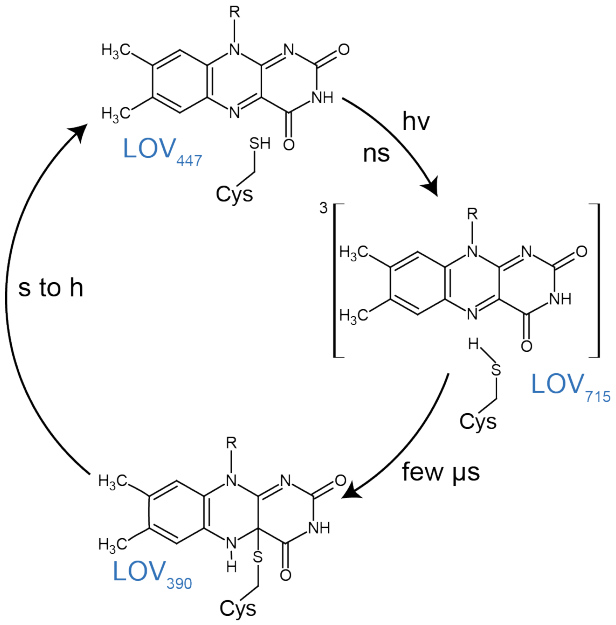

Figure 2.2: Photocycle of the LOV domain with its three intermediates LOV_{447}, LOV_{715} and LOV_{390}. In the ground state LOV_{447} the flavin mononucleotide is oxidized. By absorbing a blue photon the FMN gets excited and forms via intersystem crossing the triplet state, called LOV_{715}. Within several hundreds ns to few μs a covalent bond between C(4a) and a nearby cysteine is formed. This so called adduct state LOV_{390} decays within seconds to hours.

The process of conversion of LOV_{715} to LOV_{390} is still inconclusive although few mechanisms have been proposed. Initially, based on the available crystal structures and quantum mechanical calculations, a concerted mechanism was proposed in which a triplet-singlet conversion, bond formation as well as proton transfer would take place at the same time [10, 11]. However, this transition requires a intersystem crossing in parallel to a bond formation which has been shown to be unlikely [12]. Alternatively, the bond formation could happen via an ionic mechanism. In this mechanism, the

cysteine would transfer a proton to the N(5) which will then be followed by its anionic attack on the C(4a) atom. This hypothesis was supported by ultra-fast spectroscopic measurements [9]. However, further electron paramagnetic resonance (EPR) studies showed that no proton transfer is necessary for the adduct formation and hinted at the presence of a neutral radical [13, 14]. Also FTIR measurements provided evidence for a protonated cysteine and a deprotonated FMN in the triplet state [15, 16], thus excluding the ionic mechanism as well.

A third hypothesis states that the reaction takes place via a radical mechanism. This can happen in three different ways. If the first step of the reaction is an electron transfer from the cysteine to the FMN, then an anionic FMN^{*-} is generated [13]. Following this step, either a proton is transferred first, followed by the bond formation or vice versa. A second pathway would lead to a zwitterionic species ($FMN\text{-}SH^{+-}$). In both cases the cysteine stays protonated during adduct state formation. This is in agreement with spectroscopic data where S-H is stronger hydrogen bonded in the triplet state, probably to the N(5) of the isoalloxazine ring, than in the ground state [15]. However, it is also possible that first a H-atom transfer takes place followed by triplet-singlet conversion and covalent bond formation. This reaction pathway would create a neutral radical pair. The existence of a neutral radical pair was supported by FTIR and time-resolved UV/vis studies [16, 17] as well as theoretical calculations [18].

The adduct state is the signaling state and activates the effector domain. Its lifetime can vary from seconds to hours. In LOV_{390} the isoallaxazine ring is poor in electrons that leads to a loss of the vibrationally resolved blue absorption as well as its fluorescence. LOV_{390} decays thermally to the ground state. The driving force of this process is the high energy of LOV_{390}, about 110-140 $kJ{\cdot}mol^{-1}$, due to a strained protein conformation [19, 20].

LOV Signal Transduction

Besides the blue-light sensing domain most LOV proteins contain an additional domain known as effector domain. This is normally located on the C-terminus, but in some cases also found at the N-terminus, e.g. aureochrome 1 (see fig. 2.3). These effector domains include a variety of different domains, like histidine kinase, sulfate transporter anit-sigma factor agonist (STAS), adenylyl cyclase or bZIP [21, 22, 23, 24], and are activated by the LOV sensor domain.

The LOV domains tend to dimerize. It was shown for several LOV domains that they form dimers in solution as well as in crystals. There are mainly two interfaces suitable for dimerization, the β-scaffold (YtvA from *Bacillus subtilis*) and the N-terminal helical cap (Vivid, LOV protein from *Bacillus amyloliquefaciens* (VVD)). Also light activation can influence the dimerization state, as observed in case of LOV1 from oat

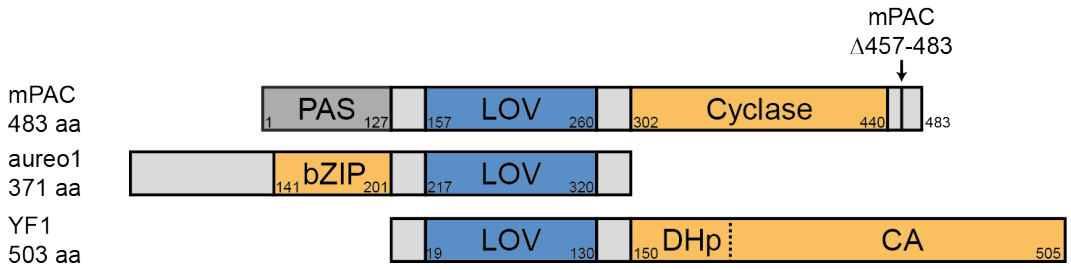

Figure 2.3: Schematic domain presentation of the LOV domains that are investigated in this study. mPAC, aureochrome 1 and YF1 reveal one LOV domain with a size of about 110 amino acids (shown in blue). Additionally they consists of different effector domains (colored orange), like adenylyl cyclase, basic zipper (bZIP) and phosphoacceptor (DHp) with catalytic (CA) subdomain. Little numbers indicate the amino acid position of each domain. Instead of full-length mPAC a truncated version mPAC $\Delta 457 - 483$, which misses the last 26 residues, was investigated in this work.

phototropin [25]. For aureochrome 1 there are dimers as well as monomers reported in solution [26, 27, 28]. The Jα-helix as well as light activation seem to be important parameters influencing the quaternary structure in solution. Considering the fact that aureochrome 1 is a transcription factor that binds DNA via dimerization of the bZIP domain, dimerization of the full-length protein seems obvious. For the light-activated adenylyl cyclase mPAC dimerization has not been yet investigated. Nevertheless other photoactivated cyclases like bPAC, PACα and PACβ where shown to form heterodimers [29]. The physiological function of these dimerizations for the full-length proteins and their importance in signal transduction are still unclear.

Up to now it seems that signal transduction from the LOV domain to the effector domain does not take place via an unique mechanism valid for all LOV proteins. Nevertheless the central β-sheet plays a major role for signal transduction. Within this β-sheet a conserved glutamine (aureochrome 1: Q317, mPAC: Q257) seems to propagate the signal from the FMN to the outer surface. This so called "switching glutamine" forms a hydrogen bond to the C(4)=O of FMN. On the outer side of the β-scaffold a conserved tryptophan (aureochrome 1: W295, mPAC: W235) is involved in internal interactions, most probably between the LOV core and the linker region to the effector domain. The crystal structure of YtvA LOV domain and of the full-length YF1 showed that the N-terminal cap as well as the Jα-helix form a coiled-coil structure in the dimer and that the signal is transmitted by a rotary-switch mechanism [30, 31]. For phototropins it is reported that light activation leads to a partially unfolding and detaching of the Jα-helix from the β-scaffold [32]. In consequence the histidine kinase domain is activated and autophosphorylation is enhanced. However, the Jα-helix seems not to be mandatory for signal transduction. For example in VIVID the N-terminal cap can take over the functional role of the Jα helix [33]. This also might be true for

aureochromes that feature an inverted arrangement of LOV and effector domain. In aureochromes the effector domain is located N-terminally to the LOV domain. Thus, the Jα-helix is no longer a connector between the two domains, although partially unfolding upon light activation was observed as well [27]. Like in VIVID, the N-terminal helical cap might be responsible for signal transmission from the sensor to the effector domain.
There is an alternative mechanism proposed involving a salt bridge that is formed between a lysine (mPAC: K229, YtvA: K97) and a glutamate (mPAC: E188, YtvA: E56)[34]. These residues lie on the surface of the LOV domain but are connected by conserved amino acids with the FMN binding pocket. Strengthening of this salt bridge during the LOV_{390} formation leads to the stabilization of the Gβ-Hβ loop. However, while this salt bridge is important in phototropin LOV1, it is not influencing the signal transduction of LOV2 or YtvA and is even completely missing in aureochrome 1 [19, 35].

2.1.2 bZIP domain

Aureochromes are recently discovered BL receptors from the algae *Vaucheria frigida*. This stramenopile owes two different species of this protein, aureochrome 1 and 2. While aureochrome 1 mediates BL-induced branching of cell/filaments [36], aureochrome 2 controls the development of the sex organ [24]. Both aureochromes consist, beside the light-, oxygen- and voltage-sensitive domain, of a basic zipper (bZIP) domain that acts as effector domain [24] and is located at the N-terminus. bZIP domains are characterized by a 30-amino-acid region rich of basic amino acids followed by a 30-40 long sequence containing a leucine zipper. This leucine zipper has a leucine residue at each seventh amino acid (minimum three of a kind) and can form a coiled-coil structure [37, 38]. The basic region is responsible for DNA recognition and binding. It was shown that the target sequence of aureochrome 1 is TGACGT [24] and thus, aureochrome 1 belongs to the S-type class of bZIP domains [28, 39]. All bZIP domains contain the typical N-x_7-R/K-x_9-L-x_6-L-x_6-L sequence that is also conserved in aureochrome 1. Overall bZIP domains reveal a long α-helical structure. By dimerization of the leucine zipper in the form of a coiled-coil the domain reveals a Y-shaped structure. With this structure it can dock to the DNA with one helix on each side located in the major grove (see fig. 2.4) [40].

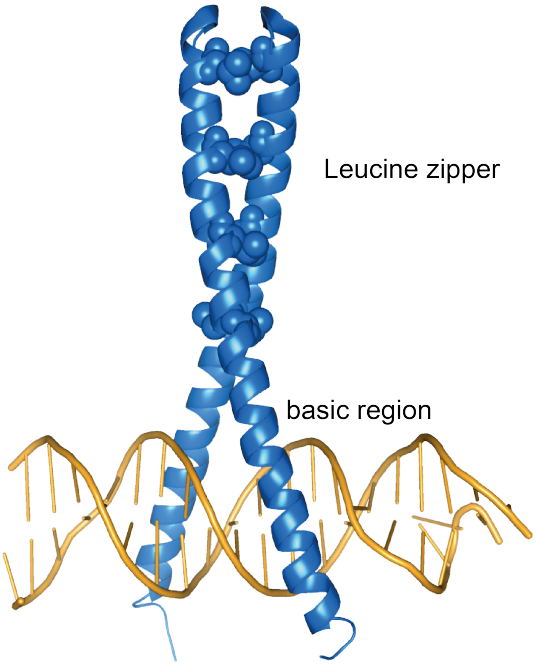

Figure 2.4: Model of the bZIP domain of GCN4 redrawn from [40]. The protein is shown in blue and DNA in orange. Leucine residues that form the hydrophobic zipper are drawn as spheres.

2.1.3 Adenylyl cyclase domain

Adenylyl cyclases (AC) convert adenosine-5'-triphosphate (ATP) into 3'-5'-cyclic adenosine monophoshate (cAMP), an important second messenger that plays a crucial role in regulation of various cell processes. There are five known classes of adenylyl cyclases distinguished according to their primary structure of the catalytic domain. Within these classes, class III is the biggest and most important, because these AC are widely distributed from bacteria to mammals. mPAC is a photoactivated soluble adenylyl cyclase from the cyanobacterium *Microcoleus chthonoplastes* [23]. The mammalian cyclases are mostly membrane proteins, with only one subclass being water soluble.
Cyclases act as dimers with the binding pockets for two ATP molecules formed between the interface of the two monomers. In mammalian membrane bound AC the dimer of the catalytic domains is formed intramolecular between the homolog domains C1 and C2. At the interface of the dimer ATP is bound specifically. The adenosine is recognized by mainly three amino acids: lysine, aspartic acid and the main chain of a leucine residue (mPAC: K353, D422, L423). Variation of these lysine and aspartate into glutamate and arginine with an additional cysteine (mPAC: S420) transforms adenylyl cyclases into guanylyl cyclases [44]. The ribose and phosphate groups are bound in a complex hydrogen bond network that also contains two metal ions (see fig. 2.5). The metal ions are chelated by two aspartate residues (mPAC: D313, D357) and a carbonyl

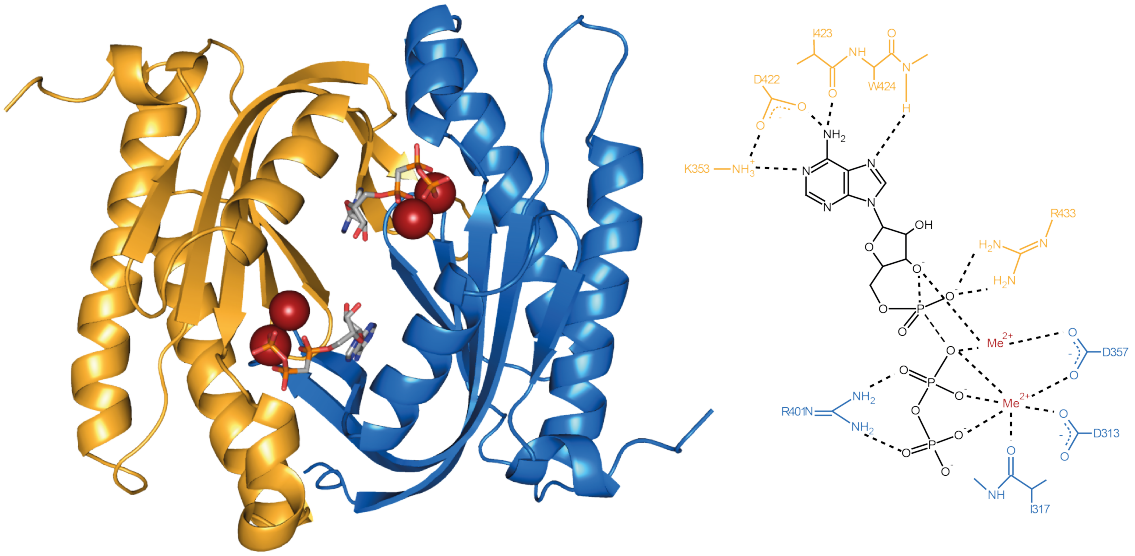

Figure 2.5: Left: Homology model of mPAC adenylyl cyclase domain. The two monomers are colored in blue and orange. The ATP analog diphosphomethylphosphonic acid adenosyl ester (APC) is shown as sticks and the metal ions as red spheres. The model based on the structure of CyaC from *S. platensis* (PDB:1WC5) [41, 42, 43]. Right: Schematic view of the ATP binding pocket. The involved amino acids and hydrogen bonds (dotted lines) are shown as well as the metal ions (red). The color scheme of the residues corresponds to the single monomers.

oxygen of isoleucine (I317). Additionally two arginine residues are involved in binding (mPAC: R401, R433). The arrangement of ATP inside the protein facilitates catalysis via the two metal ion mechanism [45]. The metal ion bound to the α-phosphate also binds to the hydroxyl group of the ribose and lowers its pK_a. This leads to a proton transfer presumably to the solvent. Furthermore the metal ions stabilize the transition state by binding to the oxygen bound between α- and β-phosphate.

2.2 KcsA, a potassium channel

Potassium channels are integral membrane proteins that are found in all kingdoms of life. They play a major role in conduction of electrical signals in nerve cells and in the maintenance of the cellular osmotic pressure. All potassium channels share homology in the pore forming domain and it was shown that this ion conductive pore is conserved among potassium channels [46]. KcsA is a bacterial potassium channel found in *Streptomyces lividans*. It is the first potassium channel whose structure was solved by X-ray crystallography [47]. X-ray data elucidates on the alignment of the conductive pore. The channel is a tetramer with each monomer consisting of two transmembrane (TM) helices with a pore helix and a loop containing the so called selectivity filter in between. The selectivity filter is formed by the conserved amino acids TVGYG. These residues point into the pore with their carboxyl oxygen and hydroxyl group of threonine and form closely spaced sites suitable for coordinating K^+ ions [47]. The carbonyl oxygen of the last glycine points out to the extracellular site and helps to re- and dehydrate the outcoming and incoming ions. The rigid arrangement of amino acids allow these channel to be highly selective towards K^+ ions compared to other ions such as Na^+ (10,000 more [47]). Below the selectivity filter the inner cavity is located. The cavity is comprised of four inner transmembrane helices of the monomers that leads to an inverted tepee structure. The cytosolic domain is connected to the inner TM helix and forms a bundle of four long helices pointing into the cytosol [48]. The N-terminus of the channel has an amphiphatic helix that is located at the membrane/cytosol interface.

Channel opening and closing

KcsA is a pH-dependent potassium channel [49]. The channel starts to open if the cytosolic pH is below 5. Several studies identified a charged cluster around the inner gate of the channel that acts as pH sensor [50]. At neutral pH the basic residues at the cytosolic membrane interface create a positive potential. This positive potential is compensated by the negatively charged residues E118 and E120. At acidic pH the glutamates become protonated and create a positive potential at the subunit interface that is large enough to open the channel by electrostatic repulsion [51]. The opening is connected with a large hinge-bending motion of the inner transmembrane helix that leads to an overall opening of about 21 Å at T112. Thus, windows are opened close to the cytosolic helix bundle that allow ions to enter the inner cavity and flow through the selectivity filter [52].

It is known that tetraethylammonium (TEA) can block potassium ions [53]. There are two binding sites for TEA in the channel: an external and an internal one. The external blocking site is located directly above the selectivity filter where TEA can interact with

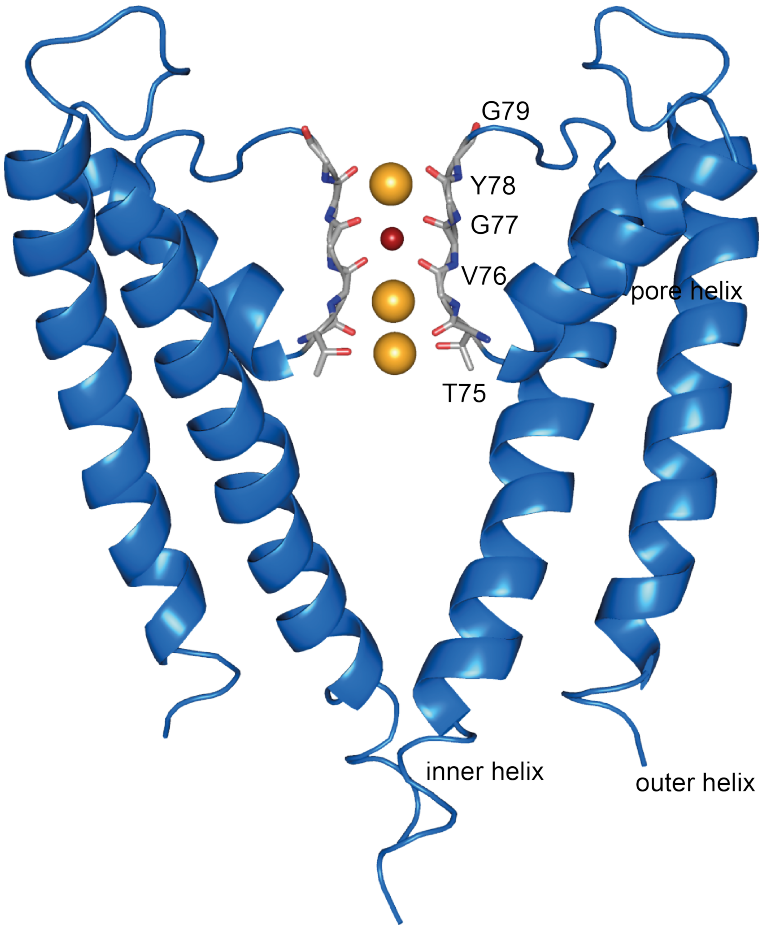

Figure 2.6: Structure of the pore domain of KcsA (PDB:1BL8[47]). The image shows the membrane part of two monomers. The selectivity filter is located at the loop between the inner helix and the pore helix (grey sticks). The K^+ ions are shown in orange and water in red.

Y82. The internal blocking site is located at the inner cavity, crated by the hydrophobic ring of I100 and F103 [54].

2.2.1 Engineering light-gated ion channels

Channelrhodopsins (ChR) are prominent and already widely used optogenetic tools [55]. Unfortunately, there are only a few ChR variants that can be used for optogenetic studies. Additionally, to use these light-gated ion channels in cells, the cells have to be infected with the encoding DNA by a virus or other methods and then the membrane protein has to be expressed by the host cells. However, even if these steps are successful, scientists often face the problem of low synthesis rates and therefore low response to light activation. To overcome these hurdles, the idea of modifying membrane proteins that are naturally expressed in the cells by an artificial chromophore was developed several years ago. These chromophores, called photoswitches, have to meet several general criteria. First the photoswitching must occur on the time scale of protein and cellular function (generally between micro- and milliseconds) using light intensities and wavelength that are not harmful for cells. Second the quantum yield as well as photoconversion has to be sufficiently high. However, it is more important to obtain a complete "off" response than a complete "on" response because persistent partial activation of proteins like receptors or channels can be toxic for cells.

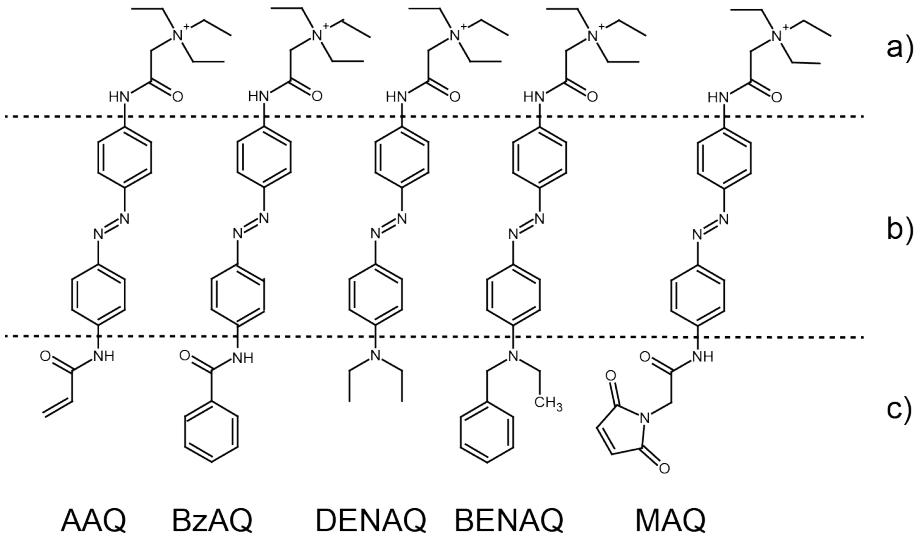

Figure 2.7: Lewis structure of the used photoswitches. All photochromic ligands contain the quaternary ammonium blocking group a) and the azobenzene b), while they differ in the variable group c). The AAQ, BzAQ, DENAQ and BENAQ can bind to either the external or internal TEA blocking site. The MAQ contains as its rest a maleimide group that can react with a cysteine side chain to form a channel with a covalently bound photoswitch that blocks from the external site [56].

The photoswitches activate/deactivate their target proteins by changing electric field, tethering components, moving blockers or antagonists, or by inducing conformational changes deep inside the protein. Thus, azobenzenes that undergo a large change in length and geometry upon *cis-trans* isomerisation, or spiropyrans that increase their polarity by photo-induced ring opening and retinal analog that also show a light induced isomerisation are examples of suitable systems for photoswitch engineering.
In this work different azobenzenes, synthesized by the Trauner group at the LMU in Munich, are used to block the bacterial potassium channel KcsA. All of the photoswitches consists of three basic parts: a) a channel blocking group: quaternary ammonium that binds to the TEA blocking site inside b) a photoactive group: azobenzene that switches between *cis* and *trans* configuration upon light illumination and c) the functional group: depending on the modification the photoswitch shows different properties. In this work five photoswitches were studied. Their Lewis structures are shown in figure 2.7.

Chapter 3

Spectroscopic Methods

3.1 UV/Vis spectroscopy

If UV or visible light passes through a sample the light can be absorbed or scattered by the molecules inside. The absorbance A of a sample is defined as the negative decadic logarithm of the intensity of the light before passing through the sample I_0 divided by the intensity of the light after the sample I.

$$A = -lg\frac{I}{I_0} = c \cdot \epsilon_\lambda \cdot d \quad \text{(Lambert-Beer law)} \tag{3.1}$$

The absorbance is proportional to the concentration of absorbing molecules c, the wavelength-dependent extinction factor ϵ_λ and the path length of the light through the sample d. UV/Vis absorption spectroscopy is used to determine the concentration of the protein in the sample. In proteins only aromatic amino acids like tyrosine, phenylalanine and tryptophan show absorption in the UV, around 280 nm. For proteins that carry a cofactor or chromophore with an extended π-system, an additional absorption in the visible range is observed. The absorption maximum of a chromophore depends on chemical modification of the π-system, the length of the conjugated π-system as well as the protein surrounding. Therefore it is possible to determine the amount of fully chromophore assembled protein with UV/Vis spectroscopy, if the extinction coefficient of the protein as well as of the chromophore is known.

3.1.1 Time-resolved UV/Vis spectroscopy

Most photoactive proteins undergo photocycles after excitation by a photons of suitable energy. During this photocycle protein and chromophore are subject to structural or configural changes which leads to a shift in the absorption maximum. To detect these

changes and probe different intermediates time-resolved measurements are mandatory. A flash photolysis setup form Applied Photophysics is used. This setup contains of a pulsed tunable laser (neodymium-doped yttrium aluminum garnet (Nd:YAG) laser with optical parametric oscillator (OPO), pulse length: 10 ns) to excite the sample, a lamp with a broad spectrum in the visible range, two monochromators and a photomultiplier (PMT) as a detector (see fig. 3.1). The white light source is a Xenon arc lamp that can run in a pulsed way for fast measurements up to 3 ms.

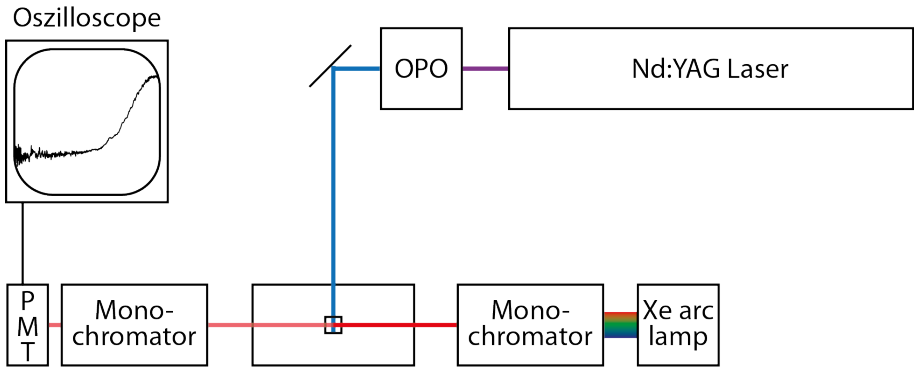

Figure 3.1: Flash photolysis setup. The sample is excited by a pulsed Nd:YAG laser that is tunable via the OPO. The absorption changes of each wavelength are followed by a PMT.

3.2 Vibrational spectroscopy

Vibrational spectroscopy monitors the frequency of molecular vibrations. The frequency of this vibration depends on the atomic mass and bonding strength and lies in the infrared region of the electromagnetic spectrum. In infrared (IR) absorption spectroscopy absorption leads to an excitation of higher vibrational modes. However, only oscillations that change the dipole moment of the vibration can be excited. The vibrational frequency ν is equal to the frequency of the absorbed light and defined by the speed of light c, the bond strength k and the reduced mass μ.

$$\nu = \frac{1}{2\pi c}\sqrt{\frac{k}{\mu}} \tag{3.2}$$

This correlation makes vibrational spectroscopy a powerful technique to observe structural changes of functional groups as well as the properties of hydrogen bonds. It is also possible to distinguish between protonation dynamics and electronic states. These informations allow to elucidate mechanisms of protein function by observing changes of ligands or chromophore, of the protein structure and interaction of amino acid side

chains.

The infrared absorption spectrum of a protein contains a number of overlapping vibrations. Each of them is coupled with an amide bond, thus C=O and N-H vibrations dominate the spectrum. Therefore IR absorption spectra of proteins (see fig. 3.2) look quiet similar and contain three dominant bands, named amide A and B (around 3300 and 3100 cm^{-1}), amide I (around 1650 cm^{-1}) and amide II (around 1550 cm^{-1}). The amide A/B band corresponds to a Fermi resonant doublet of the N-H stretching vibration overlapping with an overtone vibration of the amide II band. The amide II band contains mainly C=O stretching vibration with C-N stretching contributions. The amide II band is mainly caused by N-H bending and C-N stretching modes.

In proteins the amino acid chain forms secondary structure elements like α-helices, β-sheets or loops. Within these structure amino acids form hydrogen bonds with each other governed by the C=O and N-H groups of the amide bond. This arrangement leads to a coupling of the vibrations and therefore to a shift that can be used for secondary structure analysis. For an overview of secondary structure analysis see [57, 58, 59].

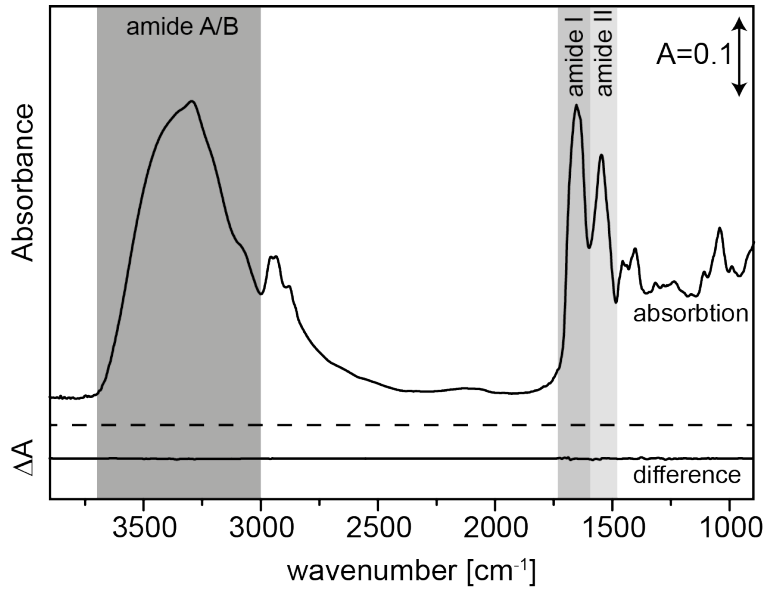

Figure 3.2: Absorption and difference spectra of a protein. The absorption spectrum shows the typical bands due to vibration of the protein backbone. The lower trace shows the difference spectrum of a light-minus-dark state of a photoactive protein. The changes of the vibration are so small that they are not visible in comparison to the absorption spectrum.

The change in the vibration of a protein while performing a reaction are normally very small. By taking the difference of the absorption spectrum of the protein in one state and that of the protein in another state it is possible to cancel out all vibrations that are not involved in the reaction. A difference spectrum is obtained that shows small contributions of groups that changed during the reaction (see fig. 3.2, lower trace). In this

spectrum negative peaks belong to one state while positive ones correspond to another. With this technique it is possible to distinguish between protonation changes or even changes in the hydrogen bonding network.

3.2.1 Fourier transform infrared spectroscopy

Fourier transform infrared spectroscopy (FTIR) is an advanced technique that comprises three advantages in comparison to standard IR absorption spectroscopy. Due to probing the sample with the whole infrared spectral range at the same time, the measurement time is drastically reduced (Felgett advantage). Furthermore the setup uses pinholes instead of slits that leads to a higher light intensity for the measurement (Jaquinot advantage). Additionally the helium neon (HeNe) laser guaranties for a high wavelength accuracy (Connes advantage).
The heart of a FTIR spectrometer is the interferometer that divides the beam into two parts that passes different path length before they are combined again and interfere. The most common interferometer is the Michelson interferometer (see fig. 3.3). It consists of a beam splitter and two mirrors. The position of one mirror is fixed while the position of the other is varied. The beam is split at the beam splitter and reflected to both mirrors. Light is reflected and guided back to the beam splitter where both beams are rejoined. Due to the movable mirror the beams are shifted in phase so they interfere at the beam splitter. The result is a interferogram that shows the intensity I in dependence of the movement of the mirror p. Due to constructive or destructive interference the intensity oscillates depending on the frequency of the irradiation. The interferogram is related to the intensity in dependence of the wavenumber $\tilde{\nu}$ by the following equation:

$$I(p) = \int_0^\infty I(\tilde{\nu})(1 + cos2\pi\tilde{\nu}p)d\tilde{\nu} \tag{3.3}$$

By using the mathematical method of Fourier transformation the interferogram can be converted in a single channel spectrum. Two single channel spectra of the background and the sample are mandatory to calculate an absorption spectrum according to Lambert-Beer's law (see eq. 3.1). Typically vibrational spectra are plotted with absorbance against wavenumbers. Wavenumbers are correlated with wavelength and frequency given by:

$$\tilde{\nu} = \frac{\nu}{c} = \frac{1}{\lambda} \tag{3.4}$$

For exact determination of the mirror position a HeNe Laser is coupled in the interferometer. The interferogram of a single wavelength is a cosines function. By detection of the zero crossings the mirror position as well the interferometer sampling points are defined. The maximal detectable frequency ν_{max} is 15802.8 cm^{-1} given by the Nyquist

theory and the wavelength of the HeNe laser.

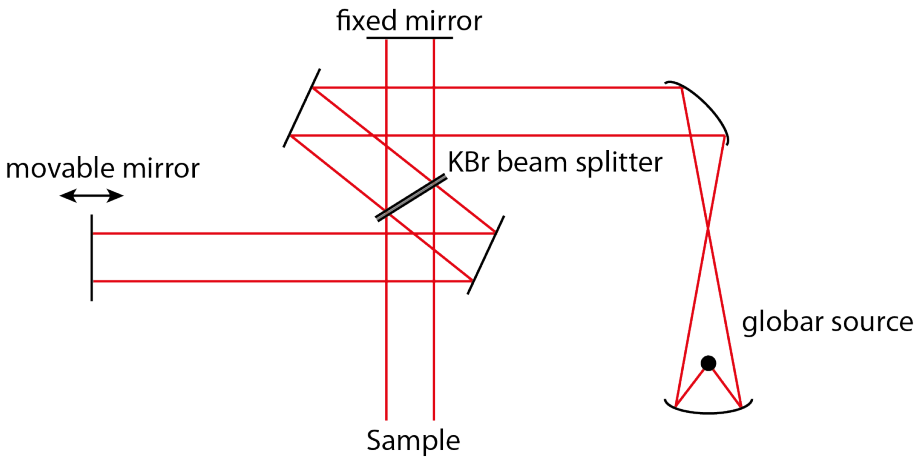

Figure 3.3: Scheme of the Michelson interferometer inside a Vertex 80v from Bruker®. The IR radiation is emitted by a globar and then directed into a KBr beam splitter. One part is reflected to a fixed mirror, the other one to a movable mirror. By moving the mirror the two beams can interfere at the beam splitter either constructively or destructively. Afterwards the beam passes the sample and hits the Detector.

3.2.2 Surface-enhanced infrared absorption spectroscopy

The infrared absorption of molecules is remarkably increased when they are absorbed in close vicinity of metal thin films. This effect was first describe in 1980 by Hartstein et al. [60]. According to the well-known phenomenon of surface-enhanced Raman scattering (SERS) this effect was called surface-enhanced infrared absorption (SEIRA). The mechanism of enhancement is not fully understood yet. However, experiments showed that the enhancement is highest when the metal surface reveals an island structure of elliptical particles of a size from 10 to 100 nm. In such metal films absorption broadens into the infrared region due to the coupling of the induced dipoles or higher multipoles of aggregated metal particles [61]. Absorption leads to an amplified electromagnetic (EM) field by absorption of light that excite a collective electron resonance (localized plasma oscillation) of the small "islands". This effect leads to an enhancement factor of about ϵ_{EM}=20 - 30. Furthermore the electric field decreases exponential with the distance to the surface which leads to an enhancement only of species in close vicinity of about 10 nm.

Experimentally enhancement factors of 500 - 600 were observed [61]. These are explained by chemical enhancement which is independent of absorption in the infrared and only has an effect on molecules in short distance. It is proposed that molecules will change their vibrational polarizability due to chemical interactions with the metal surface like

charge transfer. This interaction leads to another enhancement factor of ϵ_{short}=20-30. Therefore the total enhancement is predicted by $\epsilon_{total} = \epsilon_{EM} \cdot \epsilon_{short}$.
It was observed that the intensity of some bands are increased while others are not enhanced at all [62]. In the close vicinity the electric field that excites the molecules is perpendicular to the local surface of the metal. Therefore only vibrations with a dipole vector perpendicular to the surface are enhanced. This phenomenon was named surface selection rule. The intensity of a vibration in a SEIRAS spectrum is proportional to the scalar product of the electric field $\vec{E}$ and the derivation of the dipole moment $\frac{d\vec{\mu}}{dQ}$:

$$I \propto \left| \frac{d\vec{\mu}}{dQ} \vec{E} \right|^2 = \left| \frac{d\vec{\mu}}{dQ} \right|^2 \left| \vec{E} \right|^2 \cos \alpha^2 \tag{3.5}$$

Here α corresponds to the angle between the electric field vector and the vector of the dipole moment.

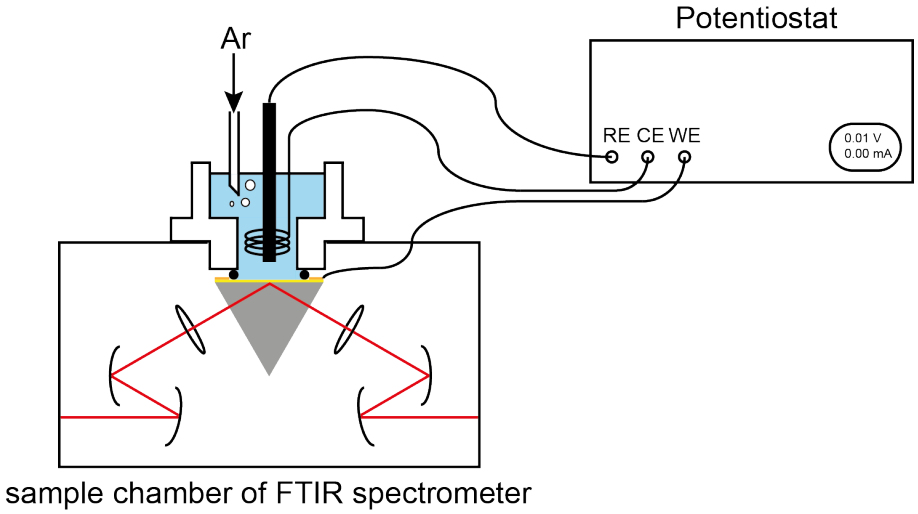

Figure 3.4: SEIRAS setup with three electrode system. The picture shows the inside of the sample chamber of the FTIR spectrometer. The IR beam is reflected by two concave mirrors and then focused on the silicon prism in a 60° angle. Then the beam is reflected by ATR and focused by a lens and two concave mirrors to the detector. The electro chemical cell is mounted on the top of the silicon prism. This configuration facilitates the exchange of the solution. The gold surface used for plasmonic enhancement can be exploited as working electrode. With a reference and counter electrode a three electrode setup is build up that is used to apply an electric field across the layer on the gold surface or inject electrons to bound molecules.

For this work a SEIRAS setup using attenuated total reflection was used (see fig. 3.4). In this setup a silicon prism is chemically modified with a thin gold film and build into a cell that can be reached from the top to facilitate solution exchange. The IR beam is guided by two concave mirrors to the silicon prims where it is reflected and then again guided by another two concave mirrors to the detector. For higher photon density the

beam is focused by lenses before and after passing the silicon prism. The cell can be used as an electrochemical cell by adding counter and reference electrodes with the gold surface as working electrode. Additionally a LED can be mounted to illuminate the surface.

3.2.3 Chemical gold deposition on silicon

The deposition of gold onto a silicon prism occurs according to Hiroto et al [63]. Briefly, remaining gold on the silicon surface was removed by boiling the prism in a 1:1:1 solution of 37 % HCl, 30 % H_2O_2 and water for about 10 min. After rinsing the prisim with water it is polished for several minutes with alumminium oxide on a microfaser tissue to remove the oxide layer on the surface. Then the silicon prism is incubated in a 40 % NH_4F solution for 1 min. Deposition of gold is performed at 60 °C by adding a 1:1:1 mixture of a reducing solution (0.3 M Na_2SO_3, 0.1 M $Na_2S_2O_3$ and 0.1 M NH_4Cl), 2 % HF and 0.03 M $NaAuCl_4$ to the surface for about 1.5 min. The reaction is stopped by rinsing with water.
To clean the freshly prepared gold surface from contamination cyclic voltammetry is performed. For this the prism is set into a solution of 0.1 M H_2SO_4 (ultra pure) and a three electrode setup with a Ag/AgCl electrode as a reference, a platin wire as a counter and a gold wire in contact to the gold surface as working electrode is installed. Then the potentiostat runs three cycles from 0.1 to 1.4 V vs Ag/AgCl with a speed of 0.025 V/s. The last cycle only give potential of the reduction and oxidation of gold. The prism is build into a measuring cell and fixed to the spectrometer (see fig. 3.4).

3.2.4 Modification of the surface

Establishment of the nickel nitrilotriacetic acid (Ni-NTA) layer on the gold surface is done in three steps. First thio-(N-succinimidylpropionate) (TSP) is bound via a sulfur bond to the surface. For this a 2.5 mM solution of 3',3-Dithio-bis(N-succinimidylpropionate) (DTSP) in water-free DMSO is placed on the surface for about 20 min. The solution is taken out and the surface is rinsed with water-free DMSO three times after the bands in the spectrum do not increase anymore (see 5.2). Afterwards a 150 mM solution of Nα,Nα-bis(carboxymethyl)-*L*-lysine (ANTA) in 0.5 M K_2CO_3 is added to the surface. The amide bond formation takes about 1 h. The surface is rinsed three times with water before the nickel is bound by adding a 50 mM solution of $NiSO_4$ to the cell for about 15 min. For protein binding the surface is rinsed with water and buffer. The surface is covered with buffer and the protein is added to a final concentration of about 5 μM. Depending on the protein sample, saturation of the surface is finished after 6–24 h.

Membrane proteins are purified by dissolving the membrane with detergents that build an artificial surrounding for the hydrophobic parts of the protein. For a nature like environment membrane proteins are embedded into a lipid bilayer by adding suitable lipids and removing the detergent. This process is called reconstitution. For reconstitution of the KcsA 1 mL of a 1 mg/mL 3:1 POPG/POPC mixture in chloroform/methanol is dried in a rotational evaporator. The lipid film is resuspended into the same volume of buffer containing 50 mM Tris pH 8, 150 mM KCl and 5 mM octyl glycoside (OG). By tip sonication the multilayer vesicles inside are converted into huge unilaminar vesicles. For reconstitution lipids are added to a final concentration of 0.1 mg/mL. After incubation for 20 min, biobeads that are washed with ethanol once and twice with water are added in three steps to the solution. First 10 mg are added, then 1 h later the next 10 mg and finally 20 mg are added and incubated for another hour. The biobeads are removed and the cell is filled with KcsA buffer without detergent.

3.3 Impedance spectroscopy

The electrical resistance is the ability of a circuit element to resist the flow of electrical current. It is defined by Ohm's law as the ratio between voltage E and current I:

$$R \equiv \frac{E}{I} \tag{3.6}$$

This equation is only valid for a ideal resistor that has several simplifying properties:

- It follows Ohm's law at all current and voltage levels
- Its resistance value is independent of frequency
- AC current and voltage signals through a resistor are in phase with each other

Typically circuit elements do not fulfill these conditions. Therefore the impedance, as a complex quantity, is a measure of the ability of a circuit to resist the flow of electrical current without limiting properties.
ting properties.
Electrochemical impedance is measured by applying an AC potential to an electrochemical cell and then measuring the output current. If a sinusoidal potential is applied the resulting current is a sum of sinousidal function (a Fourier series). To achieve pseudo-linearity the variation of the potential should be small. In a linear system the current response to a sinusoidal potential will be a sinusoidal at the same frequency but shifted

in phase.
The AC potential can be described by the following equation

$$E(t,\omega) = E_0 e^{i\omega t} \tag{3.7}$$

where $E(t,\omega)$ is the potential at time t, E_0 is the amplitude of the signal, ω is the radial frequency ($\omega = 2\pi f$) and $i = \sqrt{-1}$. In a linear system the responding current $I(t,\omega)$ is shifted in phase ϕ and has a different amplitude I_0.

$$I(t,\omega) = I_0 e^{i\omega t - \phi} \tag{3.8}$$

The impedance is then represented as a complex number,

$$Z(\omega) = \frac{E}{I} = Z_0 e^{i\phi} = Z_0(\cos\phi + i\sin\phi) \tag{3.9}$$

with Z_0 as the magnitude of the impedance that is defined by the imaginary Z^{Im} and real Z^{Re} part of the impedance:

$$Z_0 = \sqrt{(Z^{Re})^2 + (Z^{Im})^2} \tag{3.10}$$

and the phase shift ϕ:

$$\phi = \arctan\left(\frac{Z^{Im}}{Z^{Re}}\right) \tag{3.11}$$

3.3.1 Data presentation and analysis

To plot impedance spectra there are two different ways. If the imaginary part is plotted against the real part of the impedance the resulting plot is a half cycle, the so called Nyquist plot (see fig. 3.5).
With this plot Z_0 can be determined by the length of the vector from origin to the cycle and ϕ by the angle between the x-axis and this vector. Additionally the resistance of the whole system can be read out where the cycle cuts the x-axis at $\omega \to 0$. The disadvantage of this plot is that it is not possible to see which frequency was used to record the data points.
The second possibility is the Bode plot (see fig. 3.6). There magnitude of the impedance Z_0 and phase shift ϕ are plotted against frequency f. With this plot the parameter of the circuit can be determine directly. As an example the circuit (R_2C)R_1 with two resistances and one capacitor will be discussed.
In I and III the impedance is frequency-independent, so that R_1 and R_2 can be calculated. The impedance in area III is consistent with R_1 and the impedance in area I with the

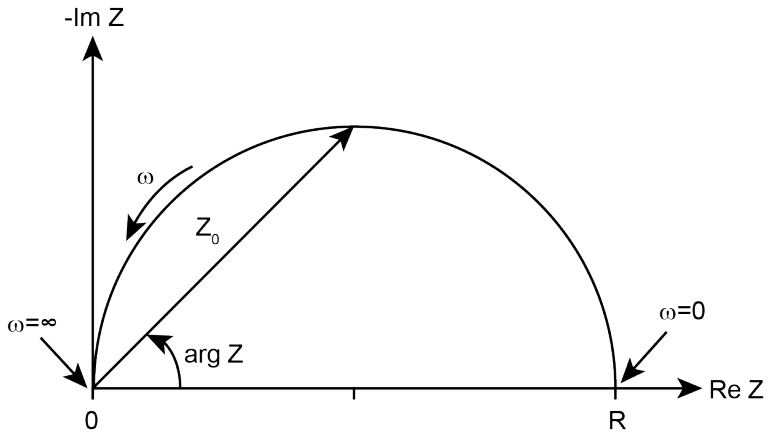

Figure 3.5: Niquist plot with impedance vector

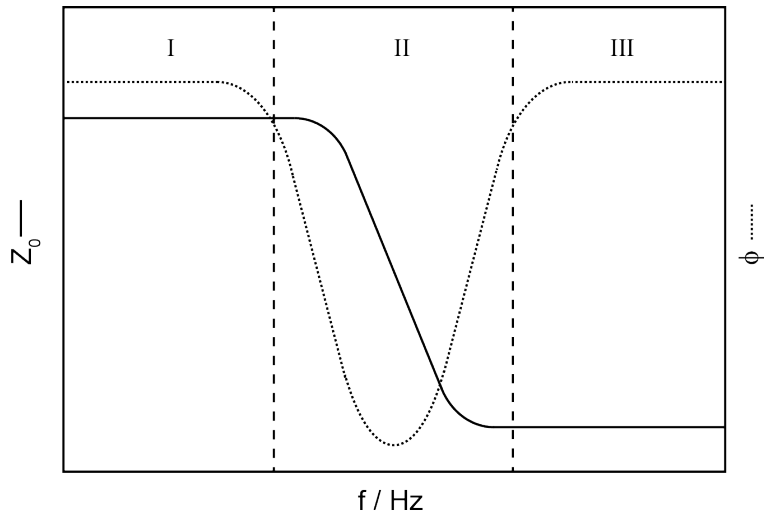

Figure 3.6: Scheme of a Bode plot for the circuit $(CR_2)R_1$. The solid line shows the plot of the magnitude of impedance and the dashed line the phase shift.

sum of R_1 and R_2. The capacitance can be calculated with the following equation: $\log Z_0 = -\log(2\pi f C)$. For more complex systems the exact analysis of the impedance spectra is done by a non-linear last square fit of the parameter.

3.3.2 Impedance spectroscopy of lipid bilayers

The right interpretation of an impedance measurement critically depends on the electric circuit that is chosen for the system to be analyzed. Considering the most important electric properties of an artificial membrane a simple equivalent circuit like shown in figure 3.7 is chosen. The simplicity of this circuit prevents possible misinterpretation of the recorded data. Electrically a membrane is comparable with a plate condenser. The

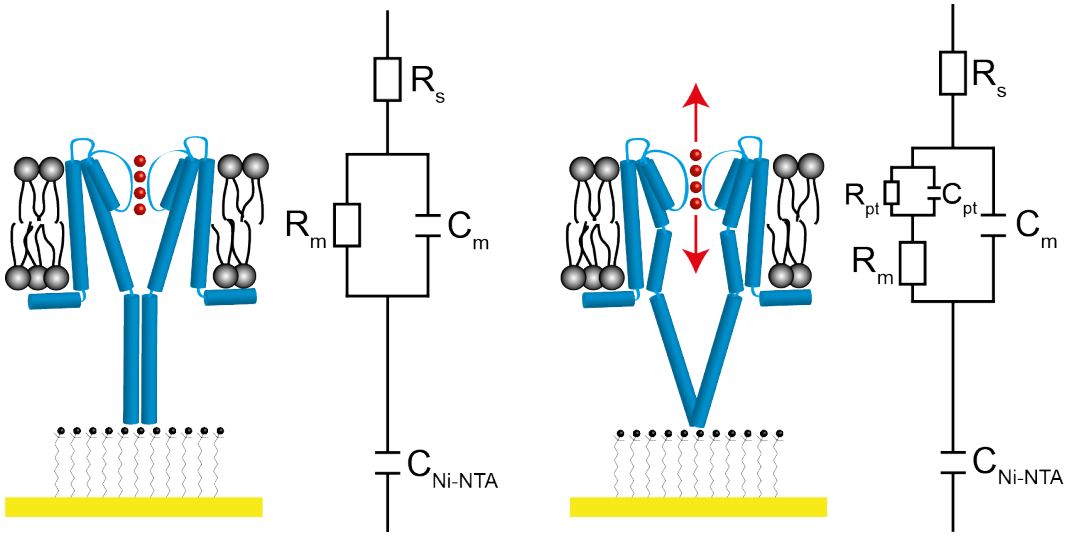

Figure 3.7: Equivalent circuit for the KcsA reconstituted into lipids on a SEIRAS gold surface. The equivalent circuit for the closed (left) and open (right) state are shown. Both circuits contain the solution resistance R_s, the capacitance of the Ni-NTA layer C_{Ni-NTA} and the parameters for the membrane R_m and C_m. Due to the ion flux while the channel is open an additional sub-circuit is added. It contains a resistance R_m that describes the ion flux through the membrane and the parallel RC-circuit (R_{pt},C_{pr}) representing the situation at the interface [64].

electrolyte solution represents the plates while the carbon hydrogen chains of the lipids correspond to the dielectric media in between with a layer thickness d and a dielectric constant ϵ_m. Therefore the capacitance of a membrane C_m is calculated by equation 3.12 with ϵ_0 as the dielectric constant in vacuum and A as the area of the membrane.

$$C_m = \epsilon_0 \epsilon_m \frac{A}{d} \tag{3.12}$$

With a relative membrane thickness of 4 nm and a dielectrical constant $\epsilon_m = 2$ (corresponding to carbohydrates) a specific membrane capacitance per area is determine to

be about 0.44 μF/cm^2. Experimentally this value was measured to be about 1 μF/cm^2 for different cell types. The difference between the theoretical and experimental value is probably due to the change in the dielectrical constant by proteins inserted into the cell membrane. However, besides the capacity a membrane is defined by a resistance. The resistance can vary in comparison to the capacity a lot and depends on the tightness and the composition of the membrane. Normally cell membranes have a resistance of about 1-1000 Ωcm^2. Artificial membranes without proteins can reach values up to 10^8 Ωcm^2 that corresponds to a very tight membrane. It is know that solid supported membranes like in our experiments normally have a much smaller resistance in the kΩ region because of considerable amounts of defects in the bilayer and lower lipid packing density. Figure 3.7 shows a scheme of the KcsA reconstituted into a lipid bilayer immobilized via a Ni-NTA layer to a gold surface. The channel exhibit depending on the pH two conformational states: the open state and the close state. These states only differ in the arrangement of the water cavity. If the pH drops from neutral or basic to acidic the helices change their conformation and open the water cavity that leads to an ion flow through the channel. Thus, the closed channel can be described by a simple equivalent circuit that defines the membrane part only with two parameters like a normal solid supported membrane (see 3.7 left). If the channel opens the ion flux through the channel is described by the former membrane resistance R_m and an additional sub-circuit (R_{pt},C_{pr}) representing the situation at the interface (see 3.7 right). In addition to the elements of the circuit that describe the situation of the reconstituted KcsA both equivalent circuit also contain the capacity of the Ni-NTA layer and the solution resistance. These parameters can be determined separately and are therefore kept constant for the fitting.

3.3.3 Operating impedance spectroscopy

The impedance spectroscopy is operated in parallel to the SEIRAS spectroscopy. Therefore the SEIRAS cell is filled with the buffer (either 50 mM Tris, 150 mM KCl, pH 7.5 or 50 mM Citrate, 150 mM KCl, pH 4) and a three electrode setup like shown in figure 3.4 is installed. Before every measurement the solution is gassed with argon to replace the oxygen. Then the open circuit potential is determined. If the OCP is stable, the impedance measurement is started. A small sinusoidal a.c. voltage with a constant amplitude of 25 mV with 50 frequencies in the range from 0.01 to 100,000 Hz is applied and the current response is recorded. The data is recorded with an Metrohm Autolab potentiostat/galvanostat (PGSTAT302N) ran by the NOVA software 1.5.0025 (Eco Chemie BV). The NOVA software is also used for analysis and fitting of the measured data.

3.4 Microscale thermophoresis

In 1856 Carl Ludwig and Charles Soret described first the effect of thermophoresis [65]. They observed that molecules tend to move from a hot region into a cooler one and vice versa depending on the molecules itself and the fluid. This thermodiffusion, also called Soret effect, is the basis of microscale thermophoresis (MST). Although the theoretical background of this phenomena is not understood fully yet, there is a generally assumption for describing thermophoresis by treating it as a transport phenomenon using microscopic particle-particle potentials, hydrodynamics or effective force fields [66]. For diluted concentrations the thermophoretic transport in a temperature gradient combined with the back diffusion of the molecule can be described by a drift current density j.

$$j = j_D + j_{TD} = -D\nabla c - D_T c \nabla T \tag{3.13}$$

The drift current density contains the normal diffusion j_D due to the concentration gradient ∇c and the thermal diffusion j_{DT} due to the temperature gradient ∇T. This effects are described by the diffusion coefficient D and the thermal diffusion coefficient D_T, respectively. The molecular drift velocity is defined as $j = c\nu$ that leads to a linear dependence of the drift velocity and the temperature gradient:

$$\nu = -D_T \nabla T \tag{3.14}$$

In the thermal equilibrium the normal diffusion compensate the thermal one and there is no effective flux ($j = 0$). For small temperature differences dT equation 3.13 is reduced to

$$\frac{dc}{c} = -S_T dT \tag{3.15}$$

with the Soret coefficient $S_T = D_T/D$. For small temperature differences a constant Soret coefficient is assumed. Therefore arbitrarily defined locations $\vec{x_0}$ with a concentration c_0 and a temperature T_0 can be defined to integrate this equation that leads to an exponential steady state distribution.

$$\frac{c(\vec{x})}{c_0(\vec{x_0})} = e^{-S_T(T(\vec{x})-T_0(\vec{x_0}))} \tag{3.16}$$

Equation 3.16 shows that the ratio of starting and end concentration of the molecule only depends on the temperature difference $T(\vec{x}) - T_0(\vec{x_0}) = \Delta T$ in case of a constant Soret coefficient.

The thermophoretic behavior of a molecule is mostly depended on the solvent particle interface and the particle charge. Normally a binding event has influence on the size, conformation or charge of a molecule and therefore will change the thermophoretic behavior

of that molecule. microscale thermophoresis uses this change in the thermophoretic response to determine binding events and also binding constants [67]. The MST setup is shown in figure 3.8A. It consists of an IR laser and a LED that are focus via an objective to a capillary. The capillaries contain a mixture of the two interacting molecules. One of the molecules is labeled with a commercial fluorescence dye and its concentration is keep constant in all capillaries. The concentration of the binding partner varies by a dilution series. The concentration of the molecule in the focal point can then be measured by the fluorescence signal. During a measurement of one capillary (see fig. 3.8B) the IR laser is first turn off and the fluorescence is recorded. After a few seconds the IR laser is turned on which leads to a heating in the focal point of about 1-2 K. The thermal gradient causes a temperature jump that relaxes within micro seconds. Afterwards the thermal difference leads to movement of molecules. Mostly away from the hot part. Within a few seconds the diffusion compensate the thermophoresis and a equilibrium is reached. The fluorescence is stable. By turning off the IR laser the molecules move back to the focal spot and the starting concentration is recovered.

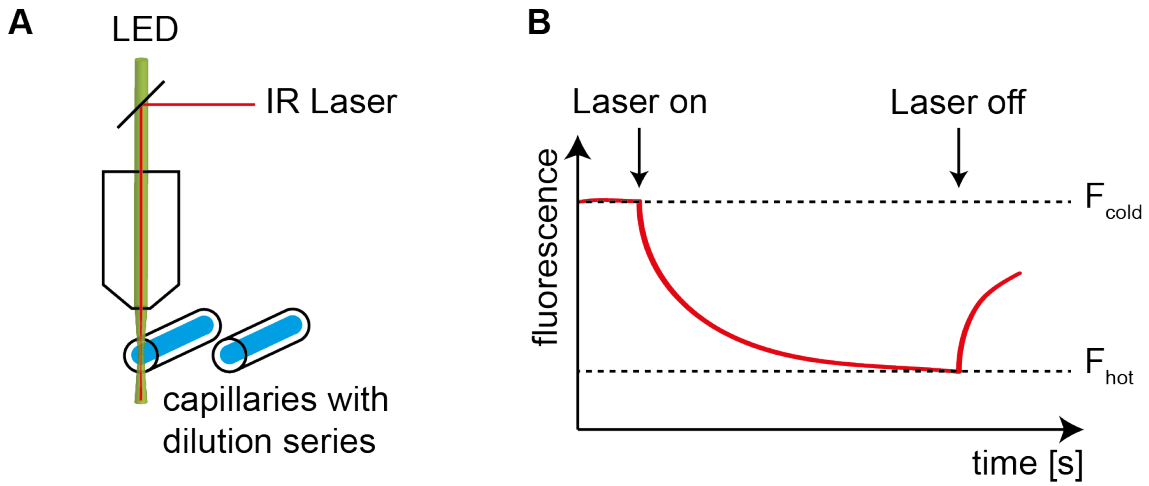

Figure 3.8: (A) Setup of the MST device. An IR laser is used to heat up a small spot of the sample that is filled into capillaries. The thermal movement of the molecules is followed by fluorescence with an either green or red LED. The capillaries contain a constant concentration of the labeled molecule and a dilution series of the interaction partner. (B) Example for one thermophoresis measurement. The fluorescence is recorded over time. The first 5 seconds the IR laser is switch off and the molecules in the focus are equally distributed. After switching on the laser the solution is heated up. Within the first microseconds an abrupt temperature jump occurs (relaxation time $\approx$ 50 ms), followed by thermal movement. After a few seconds the normal diffusion compensate the thermal one and a equilibrium is reached (after around 25 s). When the laser is switch off diffusion sets up the homologous distribution.

3.4.1 Binding constant

A binding constant is a measure how strongly two molecules are interacting with each other. For the binding reaction between component A and B we can set up the following reaction equation:

$$A + B \rightleftharpoons AB \tag{3.17}$$

The dissociation constant K_d of this equilibrium is defined by the law of mass action:

$$K_d = \frac{[A] \cdot [B]}{[AB]} \tag{3.18}$$

$[A]$,$[B]$ and, $[AB]$ are the concentration of the corresponding components. To determine binding constants from this measurements the thermophoresis curves (shown in fig. 3.8B) are recorded for different concentration of the binding partner. The fluorescence is normalized by dividing the intensity of fluorescence in the equilibrium F_{hot} by the intensity when the IR laser is switch off F_{cold}. The normalized fluorescence F_{norm} can be expressed by the concentration ratio from equation 3.16:

$$\frac{c_{hot}}{c_{cold}} = e^{-S_T \Delta T} \approx 1 - S_T \Delta T \tag{3.19}$$

Besides the thermophoresis the temperature jump $\frac{\delta F}{\delta T}$ is included in the normalized fluorescence and therefore is added to the equation.

$$F_{norm} = \frac{F_{hot}}{F_{cold}} = 1 + \left(\frac{\delta F}{\delta T} - S_T \right) \Delta T \tag{3.20}$$

The normalized fluorescence for each starting concentration of the binding partner $[B]^0$ $F_{norm}([B]^0)$ is a mixture of the normalized fluorescence of the free labeled molecule A and the pure complex AB. Depending on the fraction of molecules that are in the bound state $\chi = \frac{[AB]}{[A]}$ it can be expressed by:

$$\chi = \frac{F_{norm}([B]^0) - F_{norm}(A)}{F_{norm}(AB) - F_{norm}(A)} \tag{3.21}$$

By defining the concentration of the two components in the equilibrium as the difference of the initial concentration and the concentration of the complex, the equation for the

dissociation constant K_d and χ are set equal to determine the final fitting equation for the thermophoresis data.

$$\begin{aligned} F_{norm}([B]^0) =& F_{norm}(A) + [F_{norm}(AB) - F_{norm}(A)] \\ & \cdot \frac{[A]^0 + [B]^0 + K_d - \sqrt{([A]^0 + [B]^0 + K_d)^2 - 4[A]^0[B]^0}}{2[A]^0} \end{aligned} \tag{3.22}$$

By plotting the determined normalized fluorescence against the concentration of the binding partner [B]^0 a sigmoidal curve is obtained. The fluorescence $F_{norm}(A)$ corresponds to the fluorescence with very low concentration of B while the fluorescence $F_{norm}(AB)$ can be read out at high concentration of B where it is expected that almost all labeled molecules are bound in the complex AB. With the know starting concentration $[A]^0$ and $[B]^0$ the K_d value can be calculated.

Chapter 4

Biochemical Methods

4.1 Expression of KcsA

Spectroscopic measurements require highly purified protein. Therefore the protein is expressed and purified from *E. coli* cells (stain: RP). The procedure is explained in detail in the following section.
The plasmid pQE60 containing the KcsA gene (kindly delivered by Prof. Dr. Martin Biels group from the Ludwig-Maximilians-Universität München) is used to transform the cells by electroporation. Therefore 1 μL of DNA (concentration of $\sim$100 ng/μl) is added to 50 μl of competent cells on ice. The cells are transfered into a electroporation cuvette with a slit width of 2 mm. A potential of 1.8 kV is applied for about 5 ms to transfer the plasmid into the cells. Then cells are resuspended into 1 ml of warm brain heart infusion (BHI) medium and set to shake at 140 rpm and 37 °C for 1 h. The whole suspension is plated on BHI agar (diameter 140 mm) with 200 μM ampicillin to grow over night at 37 °C. The next day the plate is washed with 25 ml of dYT media. Each of the six 2 l flask containing 500 ml dYT medium with 200 μM ampicillin are inoculated with 4 ml of bacteria suspension from the agar plate. Bacteria grow at 37 °C until the medium reaches an optical density (OD) of 0.8 (660 nm). The expression is induced with 0.5 mM isopropyl-β-D-thiogalactopyranoside (IPTG) and cells grow for additional 3 h. Cells are harvested by centrifugation at 5700g for 25 min. The cell pellet is resuspended in fourfold volume of phosphate buffered saline (PBS) with a protease inhibitor tablet (cOmplete, Mini, EDTA-free, Roche). Afterwards cells are cracked with a cell disrupter (TS Series Benchtop, Constant System Ltd®) by pressing them twice through a valve with 1.7 bar. A tip of spatula of DNase is added to the suspension. Centrifugation at 35000g for 45 min collects the membrane fragments. Then the membrane pellet is dissolved in solubilization buffer with a tip of spatula of phenylmethanesulfonylfluoride (PMSF) by the help of a Potter-Elvehjem homogeniser. Solubilization takes place over night at

4 °C. Additional cell debris are removed by centrifugation at 35000g for 45 min. The supernatant, which includes the solubilized KcsA, is placed on a Ni-NTA column (∼3 mL) that was equilibrated with solubilization buffer before. The flow-through is again placed on the column. The first washing step includes 10 ml of solubilzation buffer. Then loosely bound proteins are removed by washing with 50 ml washing buffer. To release the KcsA from the column 10 ml of elution buffer is used and ten fractions of each 1 ml are collected. For each washing and elution fraction 15 μl are mixed with 5 μl sodium dodecyl sulfate (SDS) sample buffer and heated up for 5 min at 95 °C. The samples are placed on a 15 % SDS gel together with 5 μl SDS PageRuler Plus Prestained Protein Ladder (Thermo scientific®) that runs at 120 V for 30 min. The elution fractions that contain KcsA are merged and washed until the imidazole concentration is below 10 μM.

4.2 KcsA P55C variant

For covalent binding of MAQ to the KcsA channel a cysteine is incorporated at the conserved position according to Shaker, Kv1.3, Kv3.1, KCNQ2 and SK2 (see [68] and figA.1). Therefore a quick exchange polymerase chain reaction (PCR) is performed with plasmid pQE60 containing the wild-type KcsA gene.
The following primers are used (three bases encoding for cysteine are marked red):
Fp: GTCCTGGCTGAGCGCGGCGCATGCGGCGCGCAGCTGATCACGTATC
Rp: GATACGTGATCAGCTGCGCGCCGCATGCGCCGCGCTCAGCCAGGAC
For the PCR the following regencies are mixed in a PCR tube:

1.5 μl	forward primer (10 pM)
1.5 μl	reverse primer (10 pM)
2.0 μl	pQE60 KcsA wt (90 ng/μl)
2.5 μl	DMSO
0.5 μl	Phusion polymerase (Thermo scientific®)
10 μl	buffer HF (5x)
32 μl	water

The PCR is performed by a MJ Mini Thermal cycler (Bio Rad®) with this program:

Process	Temperature	Duration	
First denaturation	98 °C	3 min	
Denaturation	98 °C	1 min	18x
Annealing	60 °C	1 min	
Elongation	72 °C	2 min	
Final Elongation	72 °C	4 min	
Storage	4 °C	forever	

The old plasmid is digested within one hour at 37 °C by 1 μl DpnI that is added to the PCR mix. To remove primer and chopped template 6 μl Green fast digest buffer (10x) is added and the solution is applied onto a 1 % agarose gel together with GeneRuler DNA Ladders (Thermo Sientific®). The gel runs at 120 V for about 30 min. The plasmid band at 3.4 kb is cut out from the gel. The DNA is extracted from the gel by using QIAquick Gel Extraction Kit (Quiagen®). The recieved plasmid is directly transfered into *E.coli* (strain: NEB turbo) via electroporation like for KcsA (see chapter4.1). Bacteria suspension is plated on a BHI agar plate (diameter 70 mm) with 200 μM ampicillin to grow over night at 37 °C. The next day four clones are picked from the plate and grown in 3 ml BHI medium with ampicilline for 10 h at 37 °C. The plasmids are purified from these cells by using Plasmid Purification Kit (Quiagen®) and then sequence by eurofins®company.

The synthesis of the P55C variant is performed similar to the wild-type protein (see chapter 4.1). However, after the Ni-NTA column 10 mM DTT is added to each fraction to prevent aggregation by formation of disulfide bonds.

4.3 Expression of mPAC

The gene encoding for mPAC $\Delta 457-483$ was provided by Sarah Raffelberg from the Max Planck Institute in Mülheim (group of Prof. Dr. W. Gärtner) and it is cloned into the Vector pET-28a(+). The vector is transfered into competent *E. coli* cells (stain: RP) by electroporation like for the KcsA (see chapter 4.1). Transformed cells are grown on a BHI agar plate (diameter 140 mm) with 200 μM kanamycin over night at 37 °C. The next day the plate is washed with 25 ml of dYT media. Six 2 l flasks containing 500 ml dYT medium with 200 μM kanamycin are inoculated with 4 ml of bacteria suspension from the agar plate. The bacteria grow at 37 °C until the medium reaches an OD of 0.8 (660 nm). The expression is induced with 0.4 mM IPTG and protein is synthesized at 18 °C for 48 h at 400 rpm. Harvesting the cells is done by centrifugation at 5700g for 25 min. The pellet is resuspended in mPAC lysis buffer (1 ml/1 g cell pellet) with 500 μM PMSF protease inhibitor. Afterwards the cells are cracked with a cell disrupter (TS Series Benchtop, Constant System Ltd®) by pressing them twice through a valve with 1.7 bar. A tip of spatula of DNase is added to the suspension. Centrifugation at 22000g for 30 min separates cell debris from the soluble fraction. The supernatant is placed on Ni-NTA column (∼5 mL) that was equilibrated with lysis buffer before. The flow through is saved for SDS gel analysis. The first washing step includes 10 ml of mPAC column buffer (wash 1). Then loosely bound proteins are removed by two washing steps with 10 and 20 mM imidazole each in 10 mL (wash 2 and 3). To release mPAC $\Delta 457-483$ from the column 10 ml of mPAC elution buffer is used. A single fraction is collected. To remove the rest of the protein from the column 10 mL of mPAC buffer with 200 mM imidazole is used to rinse the column. Afterwards 4 mM DTT is added to each fraction to avoid protein aggregation. For each washing and elution fraction 15 μl are mixed with 5 μl SDS sample buffer and heated up for 5 min at 95 °C. The samples are placed on a 15 % SDS gel together with 5 μl SDS PageRuler Plus Prestained Protein Ladder (Thermo scientific®) that runs at 120 V for 30 min. The fractions that contain mPAC $\Delta 457-483$ are merged and concentrated. For final purification size exclusion chromatography (SEC) is performed with a Superdex 200 operated by an Äkta avant 25 (GE healthcare®). For this purpose 500 μl mPAC $\Delta 457-483$ (20 g/l) is placed on the column. The mPAC buffer flows through the column with 0.5 mL/min and protein concentration in the 0.5 mL fractions is monitored by visible absorption at 280 and 450 nm. At 280 nm armonatic side chains absorb, while at 450 nm FMN chromophore has an absorption maximum. Finally the fractions with the highest absorption at 450 nm are merged. Protein concentration as well as qualitive ratio is determined by UV/vis absorption spectroscopy.

4.4 Microscale thermophoresis measurements

For the microscale thermophoresis (MST) measurements the protein is labeled with a fluorescence dye NT-647. This dye contains a N-hydroxysuccinimide (NHS) ester group that reacts with primary amines like lysine residues. Therefore the Tris buffer solution is exchange to an amine-free labeling buffer (Nanotemper®labeling kit) supplemented with 10 mM DDM. The exchange is done by concentration of the protein in a Amicon Ultra-0.5 mL Centrifugal Filter (Merck Millipore®) to a volume of 100 μl and then adding 400 μl of the labeling buffer with DDM. This step is repeated five times until the Tris concentration is less than 50 μM. Afterwards the dye is added to the protein solution in threefold excess. The reaction takes place for 35 min at room temperature in the dark to preserve the dye. To separate free dye from labeled protein the mixture is added to a pre-equilibrated PD-10 desalting column. In this step the buffer is exchanged to the KcsA open buffer. Labeling efficiency is determined by UV/vis spectroscopy.
The MST device can measure 16 capillaries in one measurement. A dilution series is set up by placing 16 200 μl vials in a rack. In the first vial 20 μl of the photoswitch (2-20 mM) is placed. In the vials 2-16, 10 μl of the reaction buffer (KcsA open buffer) is added. Then 10 μl are transfered to the next vial mixed by pipetting up and down ten times. Finally 10 μl are taken out to repeat the procedure with the next vial. This process creates a 1:1 dilution. Finally 10 μl of the labeled KcsA (end concentration 80 nM), that was centrifuged for 10 min at 10000g to sediment aggregates, is added to each vial and mixed carefully. The solution is soaked into the capillaries and placed in the MST device. Shortly before the measurement all capillaries are illuminated with a 505 nm LED to ensure that the photoswitches are in the *trans* configuration that can bind the channel.

4.5 Chemicals, solutions and buffers

- dYT medium (per 5 l):
  80 g trypton
  50 g yeast extract
  25 g NaCl
- PBS 10x:
  1.37 M NaCl
  27 mM KCl
  100 mM Na_2HPO_4
  20 mM KH_2PO_4
  pH 7.4

- KcsA Solubilisation buffer:
  50 mM Tris
  150 mM KCl
  10 mM dodecylmaltoside (DDM)
  pH 7.5
- KcsA Washing buffer:
  50 mM Tris
  150 mM KCl
  10 mM DDM
  150 mM imidazole
  pH 7.5
- KcsA Elution buffer: 50 mM Tris
  150 mM KCl
  10 mM DDM
  500 mM imidazole
  pH 7.5
- KcsA buffer:
  50 mM Tris
  150 mM KCl
  10 mM DDM
  pH 7.5
- KcsA open buffer:
  50 mM Citrate
  150 mM KCl
  10 mM DDM
  pH 4
- KcsA P55C buffer:
  50 mM Tris
  150 mM KCl
  10 mM DDM
  20 mM tris(2-carboxyethyl)phosphine (TCEP)
  pH 7.5
- mPAC lysis buffer:
  100 mM Tris
  600 mM NaCl
  10 % Glycerol
  pH 8

- mPAC Ni-NTA washing buffers:
  50 mM Tris
  200 mM NaCl
  5 % Glycerol
  10 and 20 mM imidazole
  pH 8
- mPAC Ni-NTA elution buffers:
  50 mM Tris
  200 mM NaCl
  5 % Glycerol
  130 mM imidazole
  pH 8
- mPAC buffer:
  50 mM Tris
  200 mM NaCl
  5 % Glycerol
  4 mM DTT
  pH 8
- SDS sample buffer (2x):
  123.8 mM tris base
  138.7 mM SDS
  1.43 M 2-mercaptoethanol
  20 % glycerol
  2.9 mM bromphenol blue

Chapter 5

Results

5.1 Expression of KcsA

The expression of KcsA and its variant P55C were performed in *E. coli*. First, the bacteria carrying plasmid encoding for the protein are cultured in dYT medium laced with antibiotics. After induction the bacteria express KcsA. The cells are harvested and then broken to separate soluble fraction from membrane and cell debris by centrifugation. The total cell mass of 1 l culture is about 7-8 g. After soluble fraction was removed a mass of 2.5 to 3 g of cell debris and membranes remains. The membranes are then solubilized to dissolve membrane proteins. This solubilisate is separated from the pellet and KcsA is purified via a Ni-NTA column using the C-terminal His-tag of the protein. Each fraction of the different steps are applied on a SDS gel to follow purification and to make visible which fractions contain the KcsA channel. Figure 5.1 shows the SDS gels of the different fractions. The soluble fraction as well as the flow-through contain several bands of expected weight, because it includes all soluble protein of the *E. coli* cell, while the flow-through includes all membrane proteins. Only KcsA has a His-tag that can bind the column. The washing steps show that some proteins interact loosely with the column but can be washed away by small concentrations of imidazole (150 mM), e.g. see lane wash 2 in figure 5.1. After washing the protein is eluted in ten different fraction each about 1 ml. The gel shows that fractions 2-10 only contain one protein with a molecular mass of about 70 kDa. The concentration is highest in elution fraction 4 and 5. This mass corresponds well with the theoretical value of 75.3 kDa of the KcsA tetramer.
The overall yield of the expression was determine by UV/vis spectroscopy by using Lambert-Beer law. The extinction coefficient at 280 nm was calculated by the Protein Calculator v3.3[1] with the method of Gill and von Hippel [69]. it was determine to be $\epsilon_{280} = 34850\ \mathrm{M^{-1}cm^{-1}}$. This leads to an expression yield of about 1 mg/l culture.

[1] www.scripps.edu/ cdputam/protcalc.html

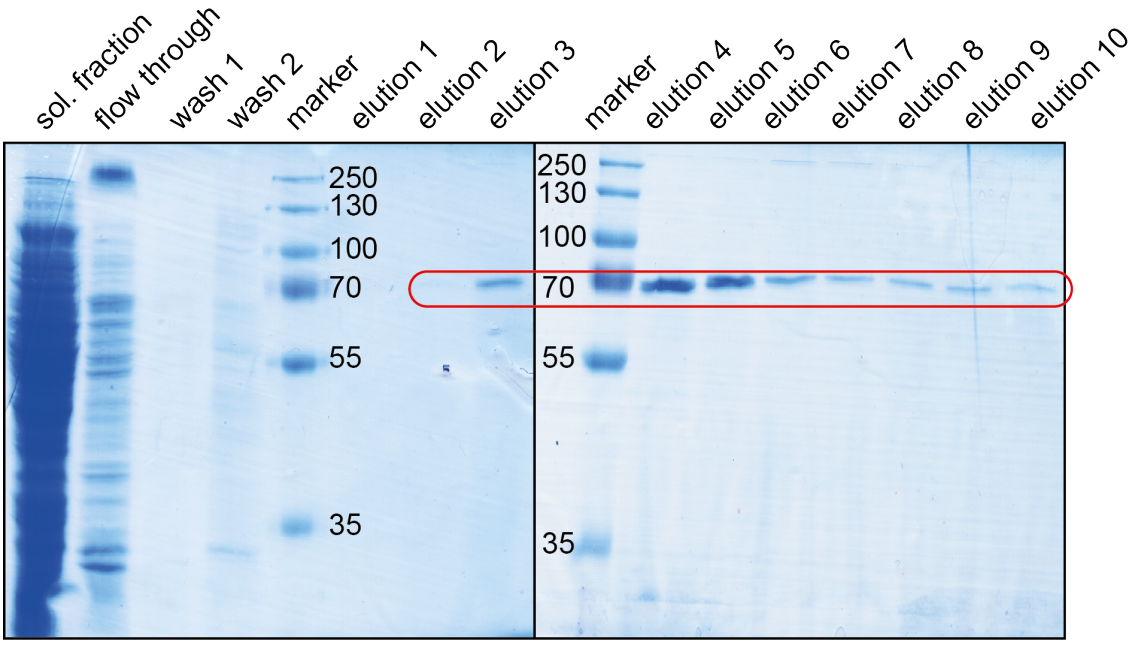

Figure 5.1: SDS gels of KcsA purification. The lanes show the protein content of the different samples taken at each step of purification. The marker works as a references to determine the molecular weight. The molecular weight in kDa is shown in numbers next to the marker bands. The left gel shows the soluble fraction together with the flow through and washing fractions of the Ni-NTA column as well as the first three elution fraction. The right gel shows the elution fraction performed with 500 mM imidazole. The KcsA is visible as a band at around 70 kDa which corresponds to the tetramer (marked by red box).

5.2 Light-gated KcsA

5.2.1 KcsA interaction with artificial photoswitches

Photoswitches suitable for blocking potassium channels all consist of a quaternary ammonium group (TEA) to bind either the external or internal TEA binding site and the photoactive azobenzene. By modification of the group bound to the opposite site of the TEA group to the azobenzene, chemical properties of the photoswitches can be influenced. So photoswitches with a shifted visible absorption spectrum or higher penetration yield into cells are created (for overview see [70, 71]). In collaboration with the group of Prof. Dr. Dirk Trauner at the Ludwig-Maximillians-Universität Munich four non-covalently bound (AAQ, BENAQ, BzAQ, and DENAQ) and one covalently bound (MAQ) photoswitches were used for the experiments (s. fig. 2.7).
To probe the affinity of the non-covalently attached photoswitches to purified KcsA in a detergent micelle, microscale thermophoresis (MST) experiments were performed. Figure 5.2 shows the results of the MST experiment for the different photoswitches. For each photoswitch concentration the ratio of fluorescence before the temperature jump F_{cold} and in the equilibrium while heating the sample with an infrared laser F_{hot} are shown. By fitting the data points with equation 3.22 K_D values are obtained (see table 5.1).

Table 5.1: K_D values for photoswitch to KcsA binding

photoswitch	K_D
AAQ	606±147 μM
BzAQ	1.1±0.2 mM
BENAQ	1.47±0.05 mM
DENAQ	no binding

5.2.2 Monitoring channel opening and closing

Patch clamp measurements demonstrated that photoswitches control opening and closing of potassium channels by light [56, 72]. To obtain a deeper understanding how these channels work at molecular level, opening and closing by light of the artificial light-gated KcsA channel is observed by SEIRAS. With this technique, it is possible to probe oriented monolayer of proteins bound to a gold surface by IR absorption spectroscopy. To immobilize proteins onto the gold surface a Ni-NTA self assambled monolayer (SAM) is formed. This formation occurs in three steps. First,

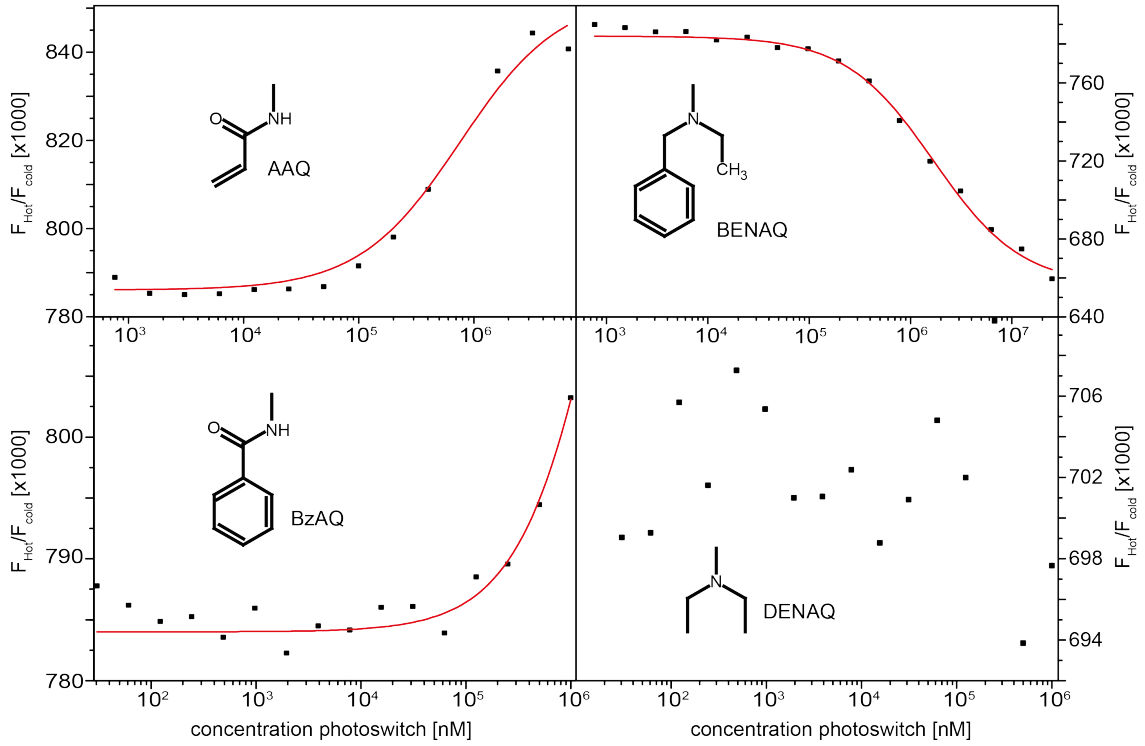

Figure 5.2: Results of microscale thermophoresis of KcsA in detergent micelles with different photoswitches AAQ, BzAQ, BENAQ and DENAQ. Response of the thermophoresis is plotted against the concentration of photoswitch. The curves are fitted with equation 3.22 and the corresponding K_D values are listed in table 5.1.

3',3-Dithio-bis(N-succinimidylpropionate) (DTSP) is reduced by the gold surface and covalently binds via its thiol group (see fig. 5.3A). Afterwards, the reaction of thio-(N-succinimidylpropionate) (TSP) with Nα,Nα-bis(carboxymethyl)-*L*-lysine (ANTA) takes place. The succinimidyl group acts as a leaving group and a peptide bond between the amide group of ANTA and the carbonyl group of TSP is formed, building up a nitrilotriacetic acid (NTA) SAM (fig. 5.3B). The three carboxylic acid groups of the end of the linker can chelating divalent ions such as Ni^{2+} or Co^{2+}. By binding a nickel ion to the NTA surface a monolayer similar to the Ni-NTA sepharose is created (fig. 5.3C). All steps are followed by SEIRAS. Each component shows specific bands in the infrared for detailed band assignment see [73]. For later analysis the impedance spectrum of the Ni-NTA layer is measured at pH 4 and 7.5. The data is fitted with a RC circuit corresponding to the solution resistance (R) and capacity (C) of the monolayer. For pH 7.5 the fit delivers a solution resistance of 11.4 $\Omega\pm5$ % and a capayity of 214 μF±5 %. These values just change slightly with a drop to pH 4 to 29.6 $\Omega\pm3$ % and 103 μF±3 %, respectively.

With the Ni-NTA linker on the gold surface it is possible to immobilize His-tagged proteins. The binding of the proteins is followed by SEIRAS. The spectrum contains the typical amide I and amide II bands that corresponds mainly to the C=O stretching and N-H bending vibration of the peptide backbone. Figure 5.4 shows the spectra recorded over time after adding KcsA solubilized into DDM to the surface. The protein binding is complete after approximately 5 h. In the spectrum the amide I band is about three fold higher in intensity compared to amide II. This effect is caused by the surface selection rule that applies in SEIRAS. Vibrations with a dipole moment perpendicular to the surface normal are enhanced more than those parallel to it. KcsA is as a mainly α helical protein with its membrane helices and cytosolic helices all aligned in one direction (see crystal structure [48]).Thus, the C=O vibrations of amide I are more enhanced than the N-H and C-N vibration of amide II.

After binding of KcsA a membrane of two phospholipids is built around the protein monolayer. This process is called reconstitution. For this purpose a POPC and POPG lipid mix in chloroform/methanol is dried on a glass flask with a rotational evaporator. This procedure creates a multilayer film of lipids on the gals surface of the flask. In the next step, the lipids are dissolved into KcsA buffer by sonification in an ultrasonic bath. The created vesicles are multilaminar. Finally, big unilaminar vesicles are created by using a tip ultrasonicator. For reconstitution of a 2D-membrane the lipid mixture is first added to the solution on the surface and then the detergent molecules are removed by adding biobeads stepwise. The biobeads are polystyrol beads with distinct cavities that allow small detergent molecules to diffuse in, but not bulky lipid molecules.

The steps of the membrane reconstitution are followed by SEIRAS (see fig. 5.5). The

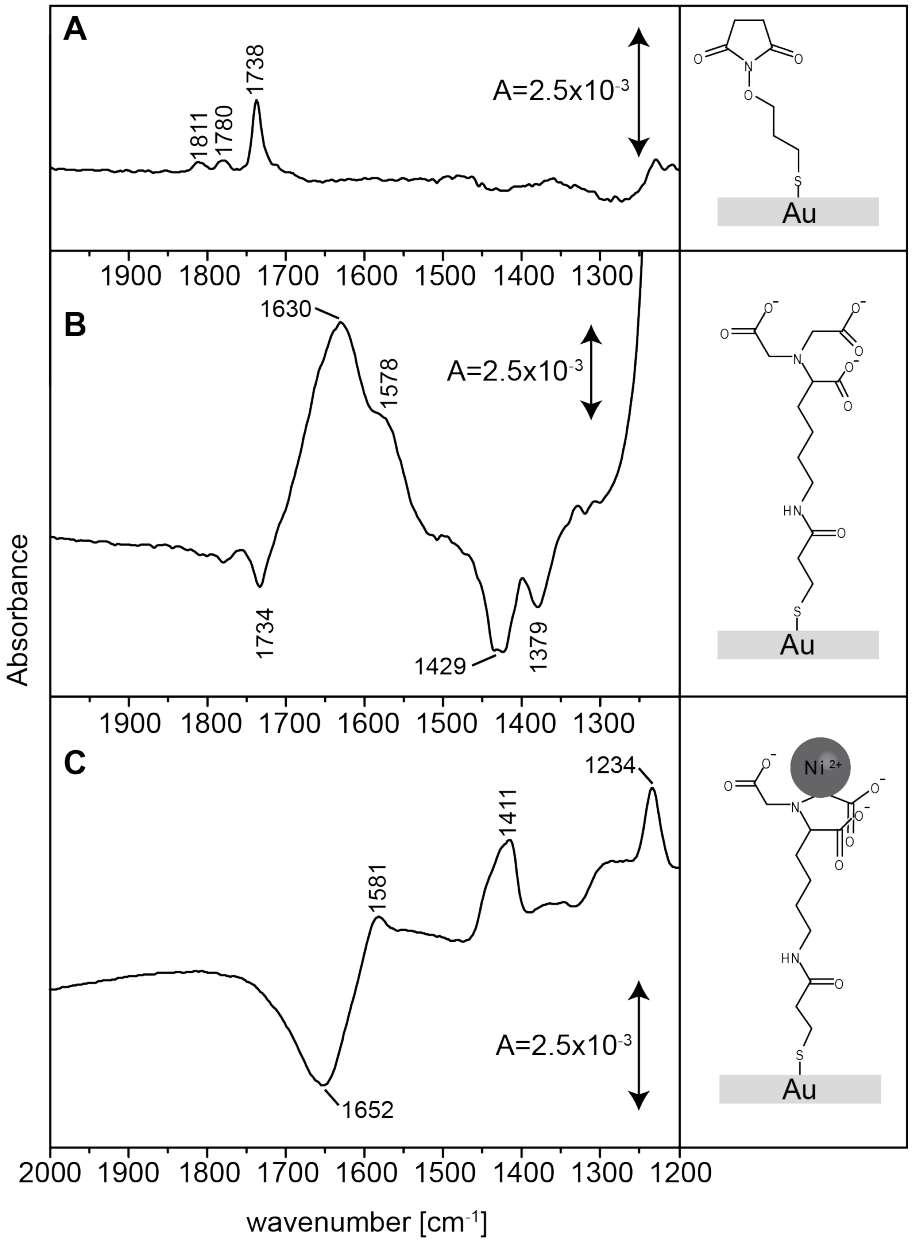

Figure 5.3: Steps of the Ni-NTA formation on a gold surface observed by SEIRAS. The spectra show the new species that is bound to the surface. (A) Binding of TSP by a sulfur bond. (B) Reaction with ANTA by formation of a peptide bond. (C) Chelating of nickel ion by by three carboxylic acid groups from the NTA. For detailed band assignment see Ataka et al. [73].

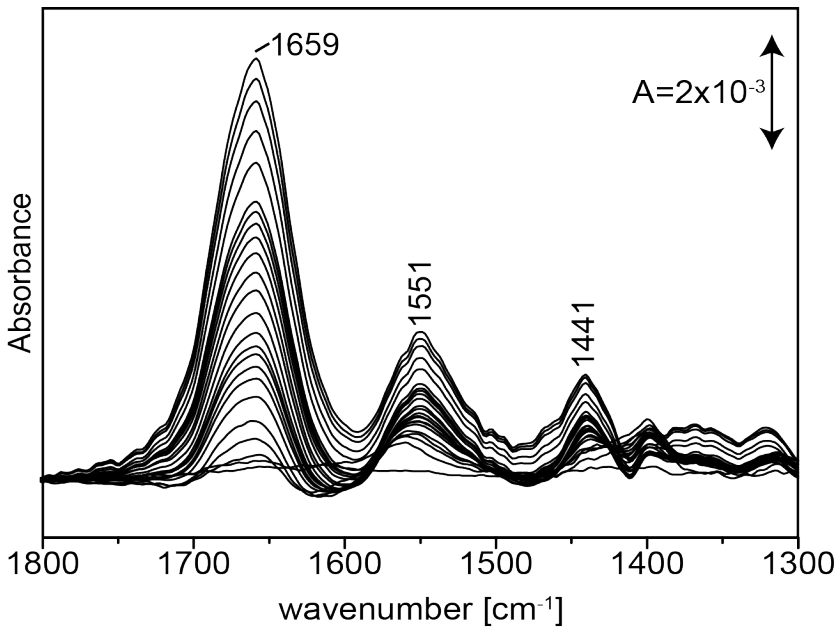

Figure 5.4: SEIRAS spectra of KcsA binding to a Ni-NTA linker on a gold surface. The spectra are recorded over 5 h. The first 15 are measured each 10 s, the next 15 spectra each 60 s, the next 15 spectra each 5 min and the last 8 spectra each 30 min. The amide I (1659 cm^{-1}) and amide II (1549 cm^{-1}) increase over time.

marker bands for phospholipids are CH_2 and CH_3 stretching vibration from the fatty acids side chains as well as C=O stretching vibration of the ester bond. The phosphate stretching vibration are not visible in the SEIRAS spectrum because they occur in the region between 1100 and 1200 cm^{-1} where the silicon prism exhibit strong absorption and therefore almost no photons reach the detector. The SEIRAS spectra proof the successful reconstitution. First, the addition of the POPC/POPG mixture leads to water (broad bands around 1650 and 3500 cm^{-1}) as well as lipid molecule (band at 1740 cm^{-1}) accumulation onto the surface. By adding biobeads, water is removed from the surface and lipid molecules start forming a lipid bilayer between the immobilized KcsA. Further addition of biobeads leads to removement of the detergent DDM that also contains a aliphatic side chain but no C=O group from an ester bond. Therefore the spectrum contains negative peaks in the C-H stretching region that overlapped with positive bands from the lipids and a positive peak at 1740 cm^{-1}. Washing away biobeads from the surface does not effect the reconstituted membrane.

To build-up a light-gated potassium channel on the surface the photoswitch has to bind to the channel. In order to reach the TEA binding site the channel has to be in its open conformation. Therefore, BzAQ is bound to KcsA at pH 4 where the channel is in its open conformation. Figure 5.6 shows the SEIRAS spectrum obtained after addition of BzAQ. The positive peaks between 1800 and 1200 cm^{-1} can be clearly assigned to

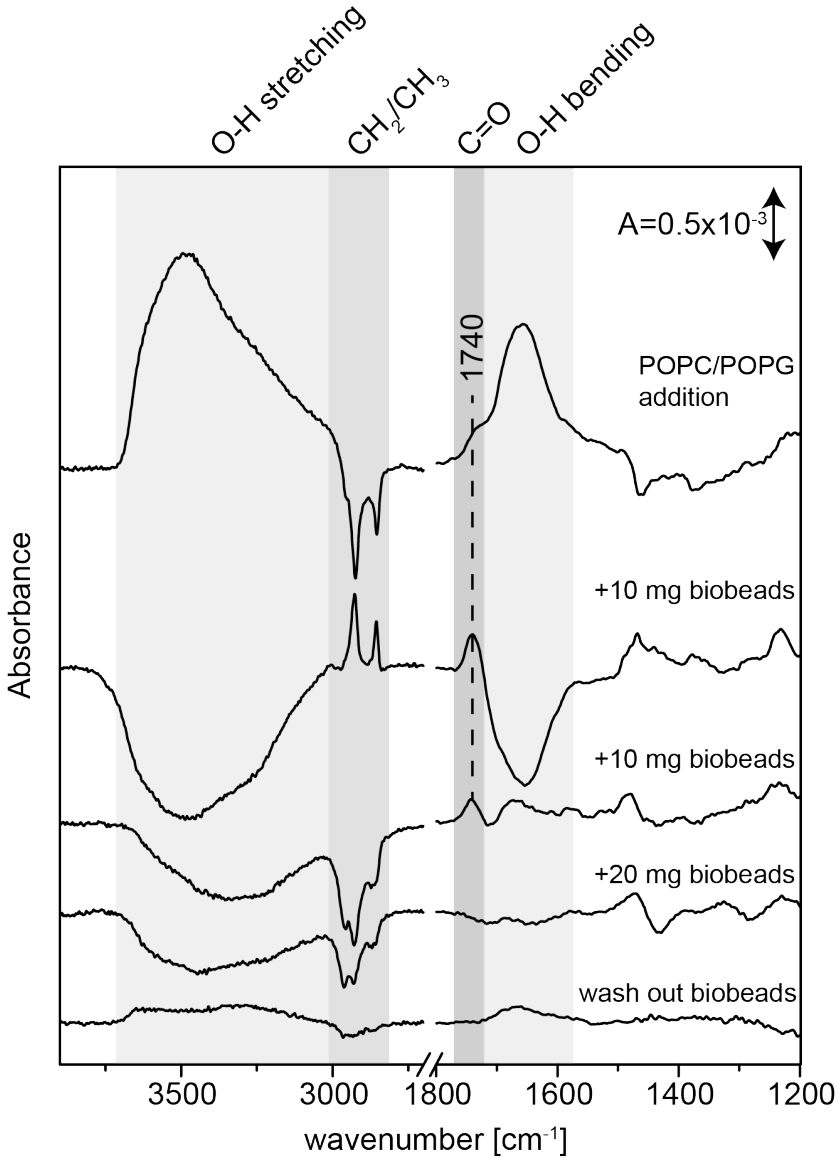

Figure 5.5: Reconstitution of KcsA into POPC and POPG lipid bilayer. The SEIRAS spectra shows the step of addition of the lipids to the solution and then the following steps of biobeads addition of first 10 mg, second 10 mg and finally 20 mg. The lowest spectrum was taken after the biobeads were removed from the solution. A background was taken before each step of addition and washing. The spectral range can be divided into 3 different parts indicated by colored background in the figure. The blue section are vibrations corresponding to the water on the surface mainly O-H banding and stretching modes. The green region markers the wavenumbers where C-H stretching of CH_2 and CH_3 appears. This region as well as red one that corresponds to the C=O stretching contain marker bands for phospholipids that formate at the surface.

vibration of the photoswitch (for pure absorption spectrum of BzAQ see A.4 in the appendix). The bands at 1697 cm^{-1} and 1554 cm^{-1} correspond to the C=O stretching and N-H bending vibration of the amide bonds. The peaks at 1597 and 1502 cm^{-1} are the C=C valence vibrations of the aromatic rings of the azobenzene, while the band at 1533 and 1448 cm^{-1} are the ones of the attached benzole ring. At 1410 cm^{-1} deformation vibrations of CH_3 of the triethylammonium group are located. The band at 1319 cm^{-1} is characteristic for the C-N stretching vibration of azobenzenes. The appearance of those characteristic bands proves that the photoswitch binds the surface. Nevertheless also negative peaks at 1744 cm^{-1} and in the C-H stretching region of long alkyl chains appear. These band positions fit well with figure 5.5).

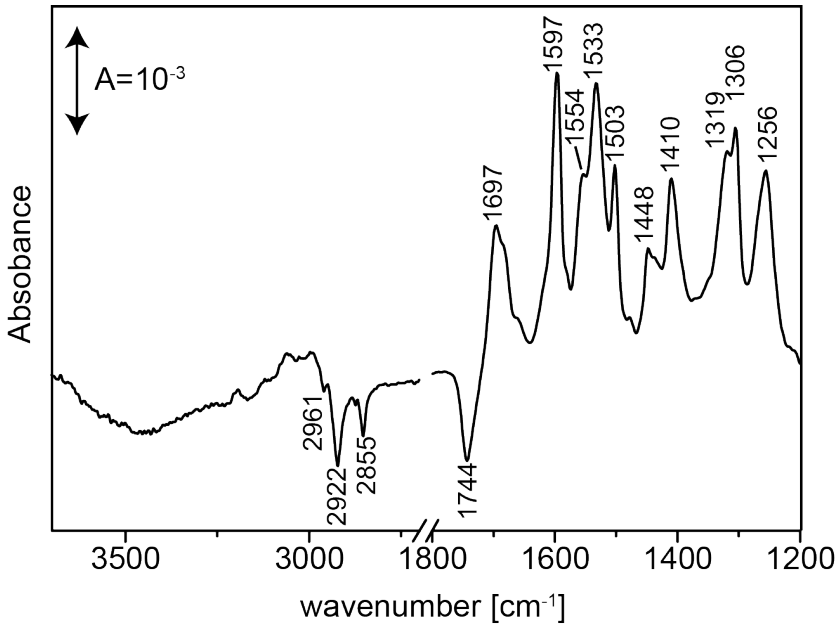

Figure 5.6: Binding of BzAQ to KcsA reconstituted into POPC/POPG membrane on a gold surface via Ni-NTA linker at pH 4. The positive peaks belong to vibrations of BzAQ the negative ones to the lipid bilayer.

To proof if BzAQ is active on the surface, light-induced difference spectra are recorded. Therefore the surface is illuminated with either a LED with a wavelength of 370 or 505 nm. By illumination with 370 nm the photoswitch isomerizes into *cis* configuration while thermal conversion or illumination with 505 nm switches the azobenzene group into *trans* conformation. Figure 5.7 shows the obtained spectra. The isomerization works well and is reversible while KcsA without BzAQ shows no response to the illumination (fig.5.7, dashed line).

To control opening and closing of the channel during isomerisation of the photoswitch, impedance spectroscopy is applied. The solid-supported membrane in this experiment can be described by an electric circuit R(RC)C. The first resistance corresponds to the

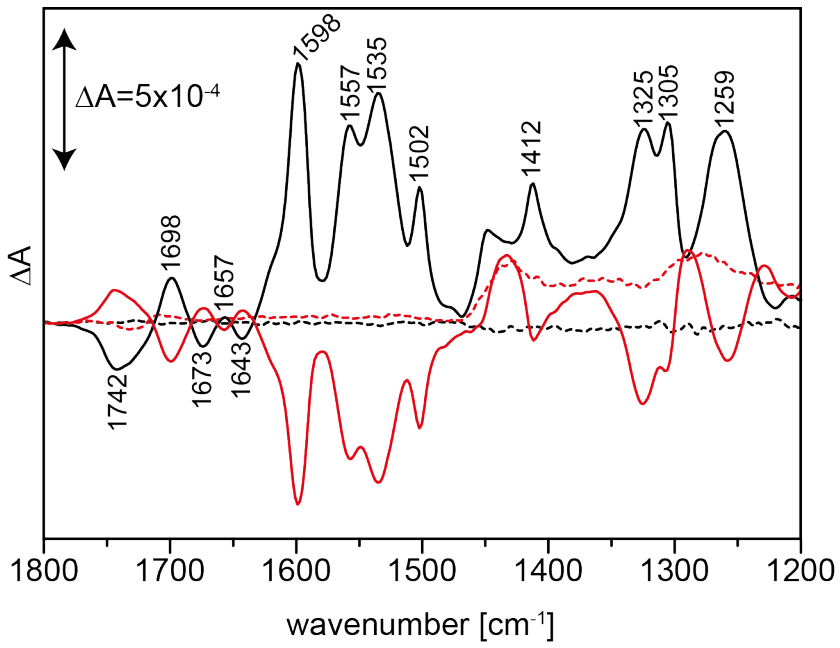

Figure 5.7: Photoswitching of BzAQ by two LEDs (505 and 370 nm). The black spectrum corresponds to the *cis-trans* isomerisation while the red one shows the conversion into the opposite direction. The dashed lines show the difference spectra obtained by illumination with 370 and 505 nm of KcsA reconstituted into POPC/POPG.

solution resistance R_s while the parallel connected resistance R_m and capacity C_m reflect the membrane parameters. The in series connected capacity is caused by the Ni-NTA linker. Solution resistance and capacity of the Ni-NTA linker was already determined for the different pH (s. above). These values are now used for further analysis, although the capacity of the linker and of the membrane are indistinguishable due to the high value of R_m. With the assumption that the capacity of the linker is stable the circuit is reduced to R(RC). Table 5.2 summarize the obtained values for the three parameters at different pH and different illumination wavelength.

Table 5.2: Values of the electric circuit of KcsA and BzAQ

pH	LED λ [nm]	Configuration BzAQ	R_s [Ω]	R_m [kΩ]	C_{m+NTA} [μF]
7	-	-	32±6%	157±16%	85±6%
4	-	-	28±5%	49±9%	78±5%
4	505	trans	22±6%	216±11%	72±5%
4	370	cis	22±7%	302±17%	82±8%

The solution resistance is quite small and almost the same for all measurements due to the identical concentration of electrolytes in both buffer solutions. Also the capacity of around 80 μF is quiet stable. However, we expect a membrane capacity of around 1-2 μF

due to the roughly estimated membrane area of about 1 cm^2 and in addition a capacity of the Ni-NTA layer of around 50 μF that was determined by impedance measurement of the bare Ni-NTA surface fitted with a RC circuit. The resistance of the membrane with embedded KcsA without the photoswitch is determined to about 160 kΩ at pH 7 and 50 kΩ at pH 4. Considering the fact that the channel opens at low pH the measured resistance reflects the light-independent formation of pores due to channel opening inside the supported membrane. After binding of the BzAQ to the surface the impedance measurement was repeated under continuous illumination with either 370 or 505 nm. The resistance is in both measurements higher than before. During illumination with 505 nm the photoswitch is in the *trans* conformation and therefore able to reach the TEA blocking side of the KcsA. Thus, the channel should be open but blocked, resulting in a higher membrane resistance in comparison to the *cis* conformation. However, the impedance data shows an opposite behavior.

The MST, SEIRAS and impedance measurements give a clear picture of the reactions on the surface. First the binding constant of the BzAQ to the KcsA obtained by MST measurements is about 3 mM which indicates a very weak interaction. Second the infrared spectra of the binding of BzAQ to the surface-tethered KcsA show the typical BzAQ bands but also negative lipid peaks. This gives rise to the conclusion that the binding affinity of the relative hydrophobic photoswitch to the lipid bilayer is higher than to the TEA binding site of KcsA. This conclusion is supported by the impedance measurement that showed a change in the membrane resistance after binding as well as an increase in the membrane resistance when the photoswitch is in the *cis* configuration and therefore unable to block the channel. Thus, the weak binding constant does not lead to a functional artificial light-gated potassium channel on the SEIRAS surface.

The MST measurements (see fig.5.2) also result in low binding constants for the other photoswitches AAQ and BENAQ. DENAQ does not show binding to KcsA at all. Therefore the approach of building an artificial light-gated potassium channel is changed. To ensure binding of the photoswitch to the channel, a P55C mutant of the KcsA is cloned and expressed according to [68] (see fig.A.1). The expression gave sufficient yield (about 0.5 mg/l cell culture) and purity to perform spectroscopy. Like the wild type the variant also forms stable tetramers that show as a single band in the SDS gel (data not shown). However, the sample has to been treated with reductive agents to prevent polymerization and precipitation. Most reductive agents like dithiothreitol (DTT) and β-mercaptoethanol can react with the maleimide group of the photoswitch or reduce the Ni-NTA layer and destroy it. Therefore a low concentration of tris(2-carboxyethyl)phosphine (TCEP) was chosen to reduce the disulfide bonds.

Binding of the KcsA P55C mutant to the Ni-NTA layer works analog to the wild type and shows the same bands with a maximum of about 9 mOD for amide I band (data

not shown). Afterwards the reaction with the MAQ takes place on the surface. The spectrum recorded by SEIRAS after the reaction of MAQ with the KcsA P55C variant are shown in figure 5.8. The big negative band in the region between 3000-3600 cm^{-1} as well as at 1650 cm^{-1} correspond to replaced water molecules due to the binding of the MAQ. The bands at 1502, 1553, 1597, 1416, 1321, 1304 and 1256 cm^{-1} are also present in the BzAQ spectrum, while the positive band at 1709 and 1782 cm^{-1} are characteristic for MAQ. They can be assigned to the C=O stretching of the maleimide ring (see fig. 5.3). The negative band around 1650 cm^{-1} overlaps with the 1697 peak of the photoswitch and corresponds to O-H bending mode of water that is displaced from the surface. After exchanging the solution containing the MAQ and washing several times with buffer, the spectrum shows that all MAQ that is not covalently bound to KcsA is washed away from the surface (see fig.5.8 lower spectrum).

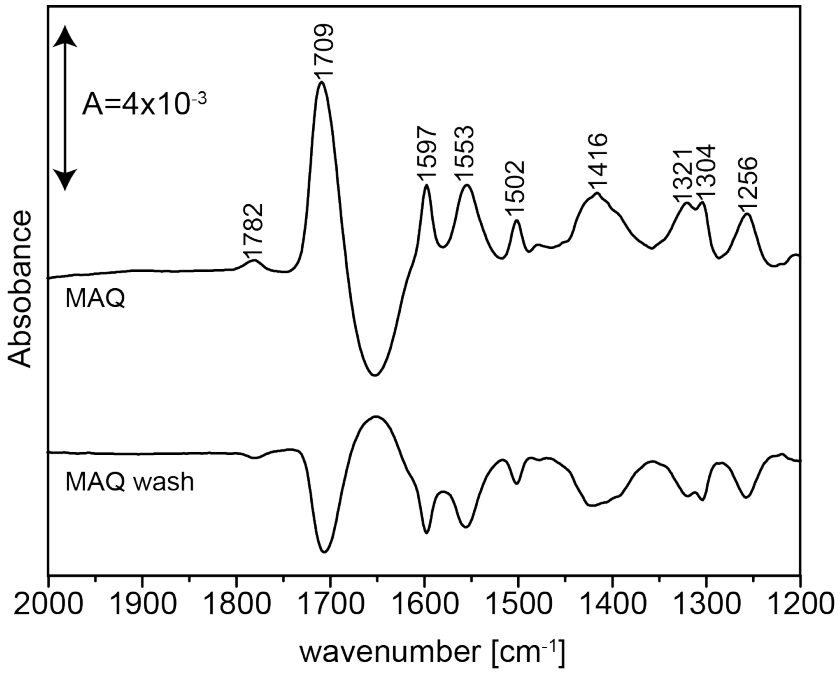

Figure 5.8: SEIRAS spectrum of the reaction of MAQ with KcsA P55C mutant that was immobilized by a his tag to a Ni-NTA modified gold surface. The spectrum after 1 h of incubation and the difference spectrum after washing the surface with buffer is shown.

Next the light induced switching of the photoswitch between *cis* and *trans* is recorded by SEIRAS. The corresponding spectra are shown in figure 5.9. Besides a reaction of the Ni-NTA layer below 1450 cm^{-1} there are bands of the photoswitch at 1595 and 1562 cm^{-1}. Additionally the spectra look like mirror images which demonstrate the reversible switching. Compared to the intensity of the absorption bands the difference bands are around 100 times smaller. Thus only the strongest band are visible while the others are covered by the noise.

The impedance spectra for reconstituted KcsA with attached MAQ are recorded and

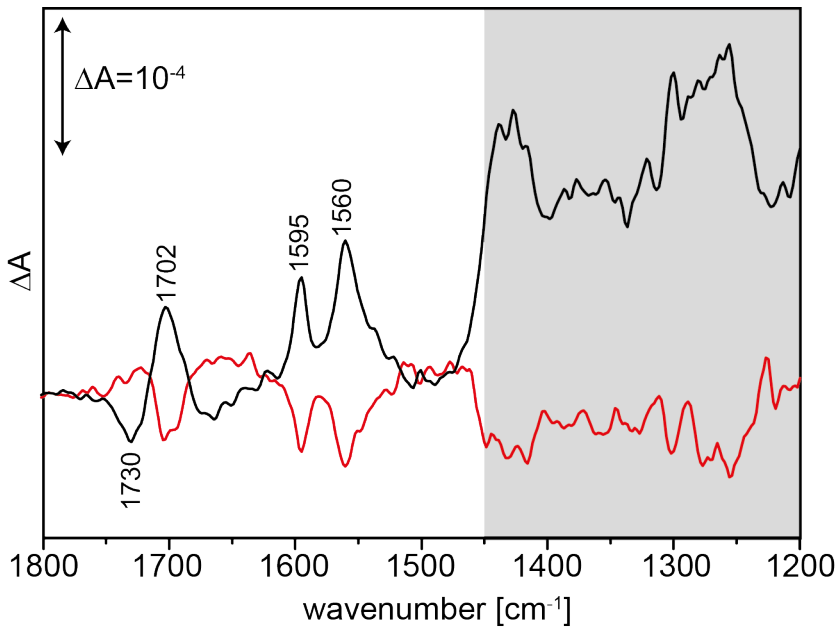

Figure 5.9: SEIRAS spectrum of MAQ bound to KcsA P55C mutant illuminated with 505 and 380 nm LED.

anaylsed with a $R_s(R_mC_m)C_{NiNTA}$ circuit. The solution resistance R_s and the capacity of the Ni-NTA layer are kept constant with the determined values from the Ni-NTA surface without protein at pH 7.5 and 4. At pH 7 when the channel is closed the resulting membrane resistance is 584±3% kΩ and capacity is 66±1% μF. The drop to pH 4 opens the KcsA channel. The ion flux through the membrane is considered by an additional (RC) pair that describes the situation at the membrane interface (see chapter 3.3.2). However, the fit with these additional parameters is not convergent. Therefore the equivalent circuit is facilitate to $R_s(R_mC_m)C_{NiNTA}$ and the resulting membrane resistance and capacity is 95.7±3% kΩ and 102±3% μF, respectively. The compairson of the capacity of the membrane shows that it does not change significant with the drop in pH. The membrane resistance in contrast decreases at lower pH. This behavior reflects the opening of the channel that creats pores in the double layer and therefore lowers the resistance significantly.

To probe the influence of the photoswitch on the membrane parameters, impedance spectra were recorded while the surface was illuminated. Illumination with 380 nm switches the azobenzene into *cis* configuration. In this configuration the photoswitch is bended (V shape), preventing the TEA group of reaching the external site and therefore blocking of the channel. On the contrary, illumination with 505 nm drives the photoswitch into *trans* conformation. The switch is stretched, the TEA site can bind to the external blocking site and the ion flux is blocked. Similar to the former analysis the impedance data is fitted with an R(RC)C circuit. Using the solution resistance R_s and Ni-NTA ca-

Table 5.3: Values of the electric circuit of KcsA and MAQ

pH	**4**		**7**	
light [nm]	380	505	380	505
R_s [Ω]	68±2%	68±2%	77±2%	75±2%
R_m [kΩ]	27±20%	30±18%	78±20%	113±18%
C_m [μF]	111±8%	107±8%	87±9%	72±8%
C_{NiNTA} [μF]	90±7%	95±6%	100±10%	128±14%
channel	open		close	
blocking	unblocked	blocked	unblocked	blocked

pacity C_{NiNTA} as fixed parameter does not lead to a satisfactory fit. Therefore these two parameter were also determined by the analysis. The results are presented in table 5.3. Like expected the solution resistance and the capacity of the Ni-NTA layer stay constant in all measurements. However, the reason for an increase in the solution resistance of about 60 Ω remains inexplicable.

At pH 7 the channel is in its closed confirmation. Thus, the configuration of the photoswitch cannot open or close the channel and should therefore have no influence on the membrane resistance. This indeed is true for the capacity that is stable in both experiments. The membrane resistance slightly drops due to the illumination with 380 nm light from 113 to 78 kΩ. Additionally both values are much lower than the previously determined membrane resistance of the reconstituted KcsA at pH 7 in the dark (about 580 kΩ). Nevertheless, the resistance further decreases with decreasing pH to about 35 kΩ, as expected. But switching the channel from *cis* to *trans* conformation has no influence to none of the determined parameters.

5.3 Expression of mPAC

While YF1 and aureochrome 1 were expressed and purified by collaboration partners at the Humboldt University Berlin (Prof. Dr. Andreas Möglich) and Max-Planck-Institute Heidelberg (Prof. Dr. Ilme Schlichting), expression and purification of the mPAC $\Delta 457-483$ was performed in-house. The gene of mPAC $\Delta 457-483$ is cloned inside a pET 28b(+) vector to create a construct with with a N-terminal His-tag and thrombine cleavage site. The cloning of the gene was performed by the lab of Prof. Dr. Wolfgang Gärtner (Max-Planck-Institute Mülheim) who kindly to provided the vector.

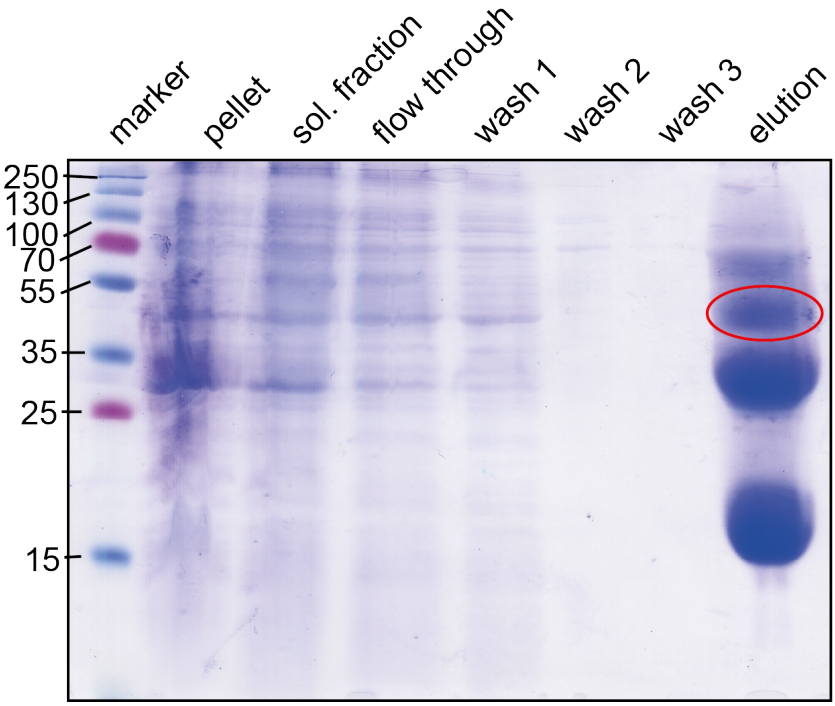

Figure 5.10: SDS gel of mPAC $\Delta 457-483$ purification. The lanes show the protein content of the different samples taken at each step of purification. The marker works as a references to determine the molecular weight. The molecular weight in kDa is shown in numbers next to the marker bands. The gel shows the proteins in the pellet of cell debris, the soluble fraction together with the flow through, washing fractions and the elution fraction of the Ni-NTA column. The mPAC elution fraction contains besides other impurities the protein with a molecular weight of about 55 kDa (marked by red cycle).

The expression takes place in *E. coli* for over 48 h. Harvesting the cells leads to about 10 g of cell mass per liter culture. Cells are cracked and the soluble fraction is separated from membrane and cell debris by centrifugation. The soluble fraction is loaded onto a Ni-NTA column. This first step of purification leads to a specific protein yield of about 21 mg/l culture as determined by UV/vis spectroscopy with an extinction coefficient of $\epsilon_{450} = 12500\ \mathrm{M^{-1}cm^{-1}}$ for the FMN chromophore [74].

The SDS gel of the fractions from the Ni-NTA column shows that the elution fraction contains a lot of impurities (see fig. 5.10). To increase the purity, size exclusion chromatography (SEC) is performed. SEC makes it possible to separate proteins of different sizes. Large proteins cross the column matrix very fast while smaller particles penetrate the pores of the matrix and therefore migrate slower through the column. Figure 5.11 shows the elution profile of the SEC run. The absorption at 450 and 280 nm of the flow through is detected and fractions of 0.5 mL are collected. Three fraction with the highest absorption at these two wavelength are used and the concentration of the protein is determine by UV/vis spectroscopy. Besides the fraction containing mPAC there are a peak of smaller proteins that elute after the mPAC $\Delta 457 - 483$ fraction (13.5-17.5 mL) and some bigger particles (8-12 mL) that also reveal absorption at 450 nm.

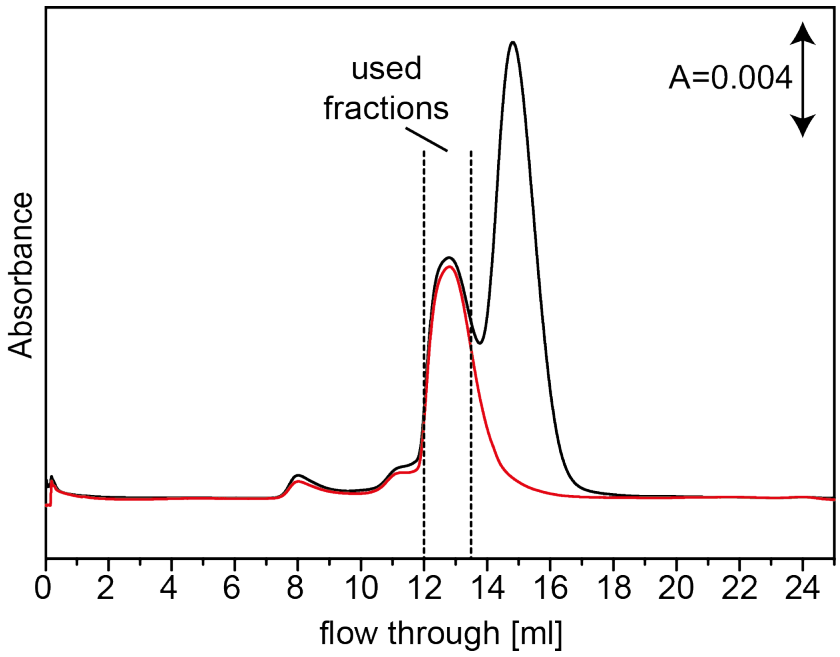

Figure 5.11: Chromatogram of the SEC run of mPAC. The black curve shows the absorbance at 280 nm and the red one the absorbance at 450 nm multiplied by a factor of 8. Each fraction contained 0.5 mL. The fractions between the dashed lines were collected and used for spectroscopic analysis.

To demonstrate the increase in purity the absorption spectrum of sample before and after the SEC run are recorded. The absorbance ratio $A_{280/450}$ is a measure to judge the amount of fully chromophore assembled protein. The theoretical value of this ratio can be calculated with the extinction coefficient of FMN and the extinction coefficient of the protein at 280 nm (ϵ_{280}(apoprotein)= 67850 $M^{-1}cm^{-1}$ calculated by Protein calculator v3.3). flavin mononucleotide also absorbs in the UV range and therefore the extinction coefficient of FMN at 280 nm (ϵ_{280}(FMN)= 21000 $M^{-1}cm^{-1}$ [75]) has to been taken into account. Thus, absorbance ratio $A_{280/450}$ of pure and fully assembled haloprotein is 7.1.

For the Ni-NTA column elution it is about 27.3, while after SEC elution a ratio of 10.3 is achieved. Therefore the SEC improved the purity by a factor of 3 and the sample can be used for spectroscopic analysis. However, a huge amount of protein gets lost during the size exclusion chromatography run. In total 9.3 mg were loaded on the column while the protein yield afterwards was just 1.9 mg. Therefore almost 80 % gets lost during the purification step.

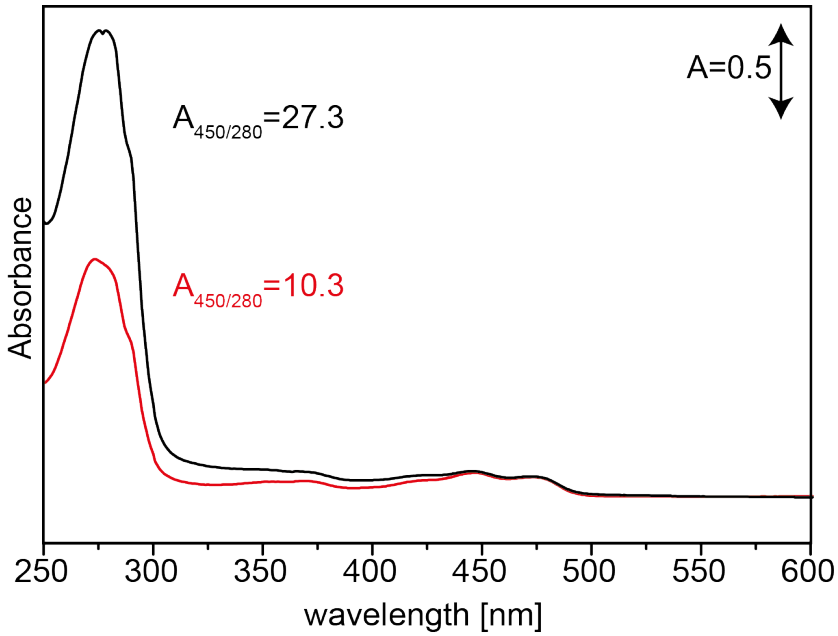

Figure 5.12: Absorption spectrum of mPAC sample before (black line) and after (red line) SEC column. The spectra were scaled to the absorption at 450 nm. The determined ratio of $A_{280/450}$ is 27.3 and 10.3, respectively.

5.4 Diversity of the LOV domains

In this work, three different LOV domains together with their effector domains were studied. Although the LOV domains of aureochrome 1, mPAC and YtvA show high homology, there are distinct differences. This is obvious from the absorption spectra. All three show the typical FMN peak with three maxima of the vibronic fine structure around 450 nm as well as an additional band around 370 nm, corresponding to a $\pi\pi*$ transition of the flavin of $S_0 \rightarrow S_1$ and $S_0 \rightarrow S_5$, respectively. However, the exact maxima differ among the LOV domains and especially in the UV region around 370 nm they show different features (see fig. 5.13). While in aureochrome 1 and YF1 the peak maximum is at 374 and 377 nm with a small shoulder around 355 nm, this peak shows a double-peak structure with maxima at 370 and 355 nm for mPAC $\Delta 457-483$. These differences in the shape of the peak around 370 nm were reported already for the LOV1 and LOV2 domains

of phototropin [76, 77]. Recent studies identified a threonine side chain that is located in the chromophore binding pocket as the main determinant for the spectral features in the UV region [78]. This residue is conserved in YF1 (T30) and aureochrome 1 (T222) while it is a replaced by a apolar alanine in mPAC (A162). Therefore aureochrome 1 and YF1 reveal LOV domains that are more similar to LOV2 while mPAC shows similarities to LOV1 of phototropin.

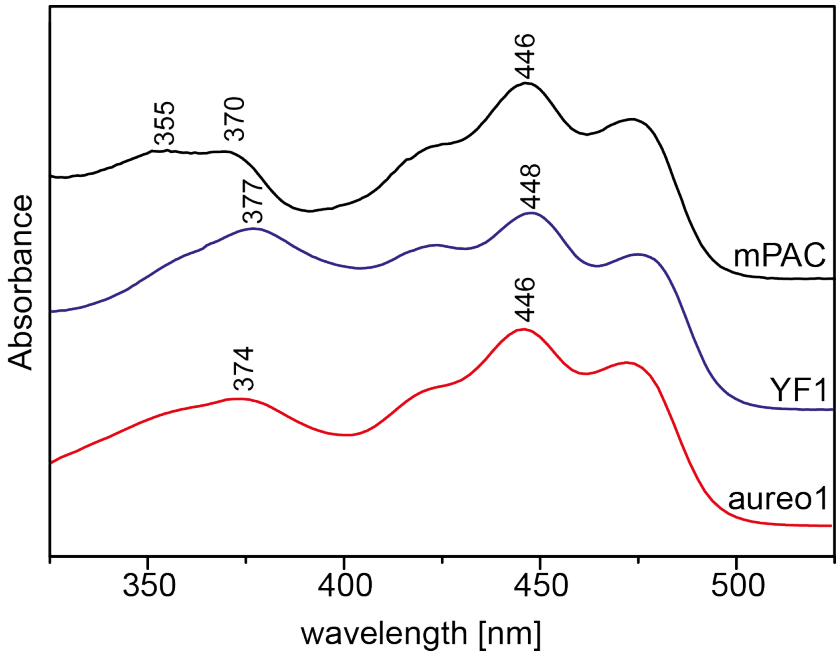

Figure 5.13: UV/vis absorption spectra of mPAC $\Delta 457 - 483$ (black), YF1 (blue) and aureochrome 1 (red) in the blue and UV region.

5.5 Kinetic of the LOV domain

The LOV domain photocycle consists of three different species. The ground state LOV_{445} exhibit an absorption maximum around 450 nm with three bands that corresponds to the vibronic fine structure of the chromophore flavin mononucleotide. After blue-light absorption FMN is excited and converts via inter system crossing into the triplet state. This triplet intermediate is called LOV_{715} due its absorption maxima at 715, 660, and 390 nm. Within several hundred ns to few μs the triplet state decays into the adduct state LOV_{390} with a single absorption maximum at 390 nm. The adduct state is characterized by a covalent bond between a nearby cysteine and the C4a of the isoallaxazine ring of the FMN. The mechanism of adduct formation was under debate over several years. However, time-resolved UV/vis spectroscopic data and quantum

mechanical calculations gave evidence for a neutral radical mechanism [79, 17].

Aureochrome 1

To determine the kinetics of the full-length aureochrome 1 as well as for mPAC $\Delta 457-483$, flash photolysis measurements were performed. This technique allows to follow absorption changes after an exciting laser pulse with a time resolution of up to 50 ns. The triplet state is formed within a few nanoseconds and cannot be detected with our system. Decay of the triplet state LOV_{715} can be monitored by recording absorption changes at 390, 660 and 715 nm (see fig. 5.14). The decay fits to time traces with a mono exponential decay. A time constant of 1.4 ± 0.2 μs is obtained that agrees well with the time constant of 2.8 μs as derived by light-induced transient grating spectroscopy [28]. This value is in the range of other LOV domains like phototropin1 LOV1 (4 μs), LOV2 (1.9 μs), and YtvA (2 μs) [80, 19, 81]. Formation and decay of the adduct state LOV_{390} cannot be observed with flash photolysis because the absorption of the triplet overlaps with the adduct state at 390 nm. Furthermore, decay of the adduct state is too slow to be followed by flash photolysis. However, the adduct state is visible in the time trace at 390 nm as a plateau after decay of the triplet (see fig. 5.14 first trace).

The decay of the adduct state was followed by steady state UV/vis absorption spectroscopy. Each 45 s a whole spectrum is recorded after illumination of the sample with a high power LED of 455 nm for 5 s. The spectra are shown in figure 5.15. After illumination a pure spectrum of the adduct state LOV_{390} is recorded with the maximum at 390 nm and no absorption around 450 nm. Over time the adduct state decays and the absorption of the ground state is recovered. By plotting the absorbance at 450 nm of each spectrum over time a kinetic curve is obtained. Fitting the trace with an mono exponential decay produces a time constant of around 22 min.

This values is in excellent agreement with the time constant for the LOV-Jα from *Phaeodactylum tricornutum* construct of Herman et al. [27] but differs significantly from the time constants determined for free LOV domain of aureochrome 1 from *Vaucheria frigida* that was determine by Takahashi and Mitra [24, 7]. In comparison to the half-life times of 4.9 and 9 min the photocycle of the full-length aureochrome 1 is prolonged by the bZIP domain.

mPAC $\Delta 457-483$

For mPAC $\Delta 457-483$ the photocycle is much faster in comparison to aureochrome 1. It takes about 50 s until the ground state is recovered. Therefore it is possible to observe even the decay of the adduct state by flash photolysis. Figure 5.16 shows the important time traces for the ground state (ΔA at 440 nm), the triplet state (ΔA at

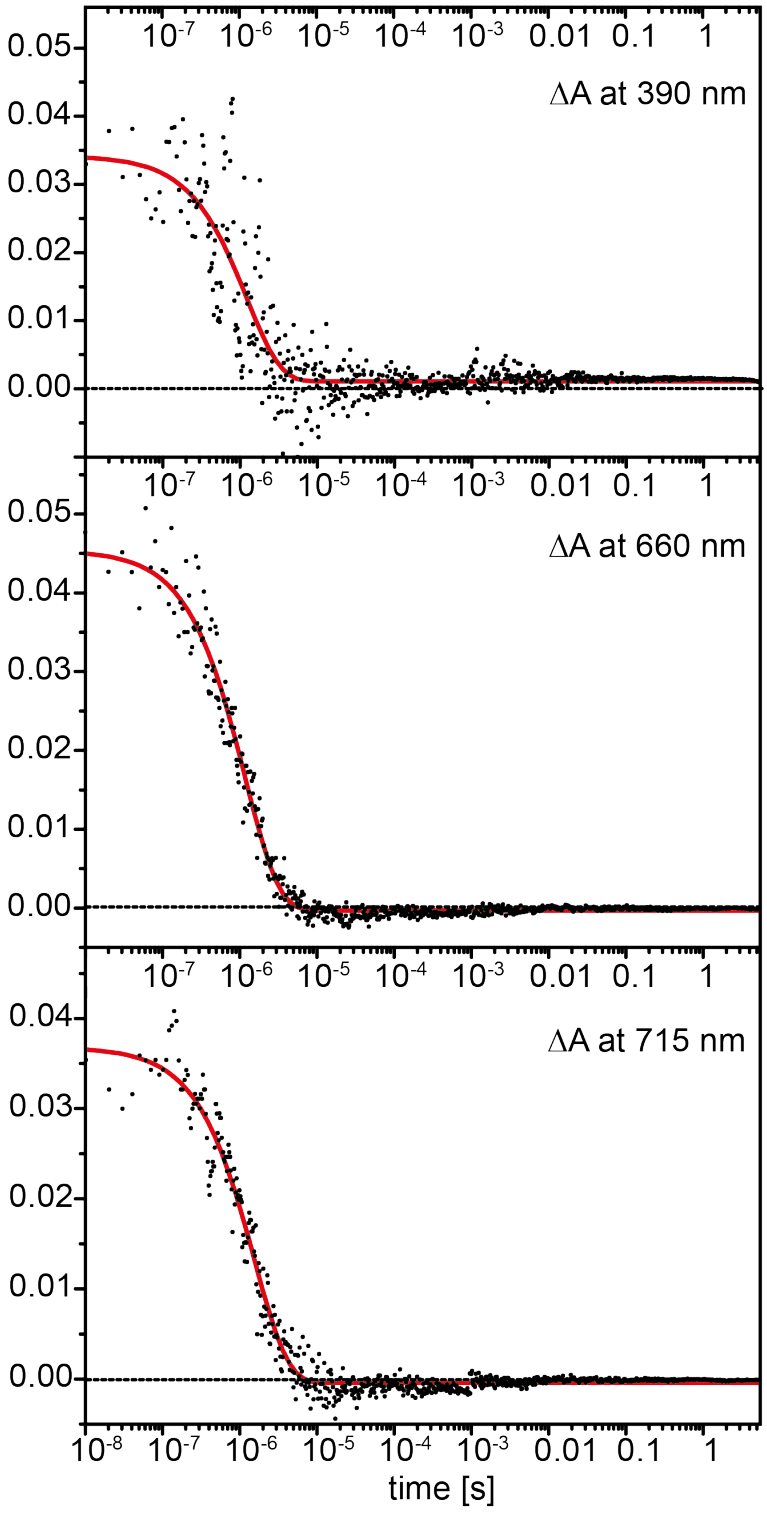

Figure 5.14: Fast kinetics of aureochrome 1 measured with flash photolysis at three different wavelength. The dots corresponds to the raw data, the red line is a mono exponential decay fit to this data. The time constants are 1.5 μs, 1.2 μs and 1.5 μs for 390, 660 and 715 nm, respectively.

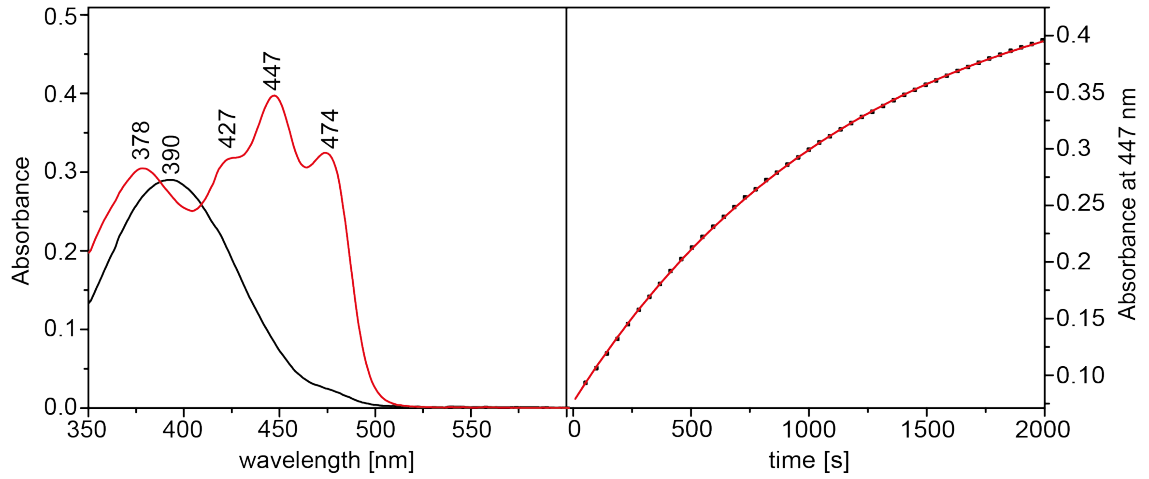

Figure 5.15: Kinetics of the recovery of the ground state. Left: Absorption spectrum of the ground state LOV_{445} (red line) and the adduct state LOV_{390} (black line) of aureochrome 1. Right: Kinetics of the recovery of the ground state after illumination with LED 455 nm for 5 s. The time constant of the recovery is about 20 min.

390, 660 and 720 nm) and the adduct intermediate (ΔA at 390 nm). The rise of the triplet state is too fast to be observed. The decay is visible at three wavelength and the corresponding time constants are 570±11, 790±20, and 640±15 ns for 390, 660 and 720 nm, respectively. The time trace at 390 nm also includes the decay of the adduct state. Therefore this curve was fitted with an two exponential decay with a second time constant of 8.2±0.5 s for the adduct decay. The time trace at 440 nm corresponds to the ground state that recovers with a time constant of 8.2±0.2 s. This value agrees well with the decay of the adduct state. In comparison to other LOV domains the decay of the triplet state is significant faster. Typically the triplet state decays within in a couple of μs like aureochrome 1 and phototropin.

Influence of imidazole on the thermal decay

Imidazole accelerates the thermal decay of the adduct state in some LOV domains via a base-catalyzed mechanism. Imidazole takes up a proton from N5 of the isoallaxazine ring of FMN. In the following step the free electron pair creates a double bond between the C4a and the N5 which breaks the bond between C4a and the sulfur atom of the reactive cysteine (s. fig5.17). The influence of imidazole on the kinetics of the recovery of the ground state is shown in fig. 5.18. Following the time trace at 390 nm the influence of imidazole on the kinetics of the triplet state as well as the adduct state becomes visible. The decay of the triplet state τ_1 varies around 650 ns and is not changed significantly by addition of imidazole (see fig. 5.18 table). The kinetics of the adduct decay show an influence starting from concentration as high as 500 mM imidazole. The time constant τ_2 decreases from about 8 s to 2 s at concentrations of 1 M imidazole. However, this

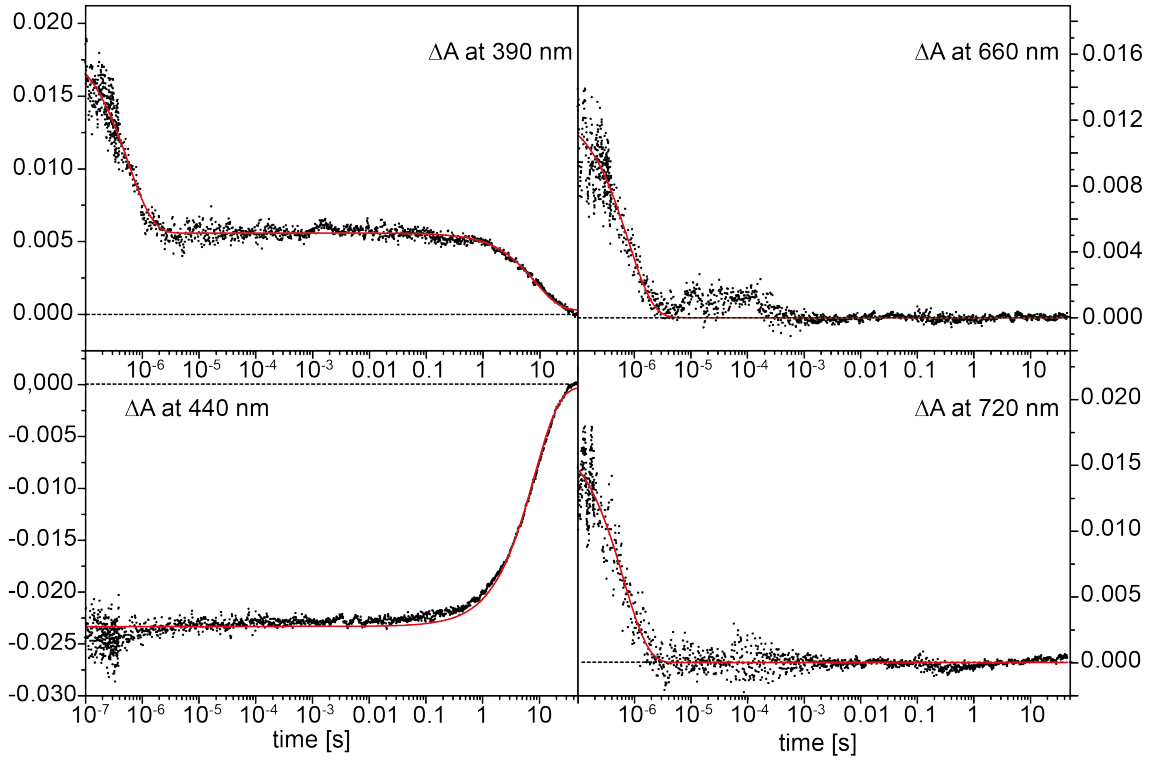

Figure 5.16: Kinetics of the mPAC $\Delta 457 - 483$ photocycle intermediates. The four time traces correspond to the different intermediates. The time trace at 390 nm shows the LOV_{715} and the LOV_{390} while the trace at 440 nm corresponds to the ground state LOV_{445}. The traces at 660 and 720 nm contain the maxima of the triplet state. The traces were fitted with a bi exponential decay in case of the 390 nm trace and with a mono exponential decay for the others. The resulting time constants for the triplet state are 570±11, 790±20, and 640±15 ns for 390, 660, and 720 nm, respectively. The decay of the adduct state was determined with 8.2±0.5 s and the recovery of the ground state is 8.2±0.2 s.

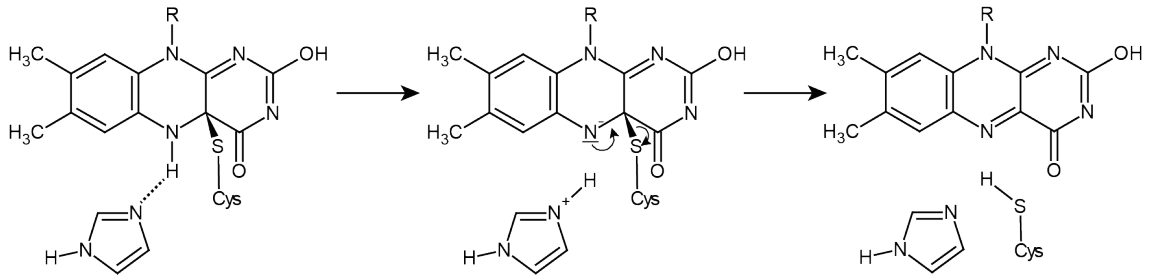

Figure 5.17: Scheme of the base-catalyzed mechanism of the thermal decay of the adduct state LOV_{390}. Imidazole acts like a base and accepts a proton of N5. Afterwards resulting electron pair at the nitrogen flips over to form a double bond with C4a, which leads to a break of the bond between C4a and the sulfur from the cysteine. In the final step the imidazole donates its proton to the cysteine and the ground state is recovered.

influence is small in comparison to other LOV domains like that one of Aureochrome 1 from *Phaeodactylum tricornutum* and LOV2 domain of phototropin from *Avena sativa* that is 20 fold and 3 fold fast at an imidazole concentration of 1 mM, respectively [27, 82].

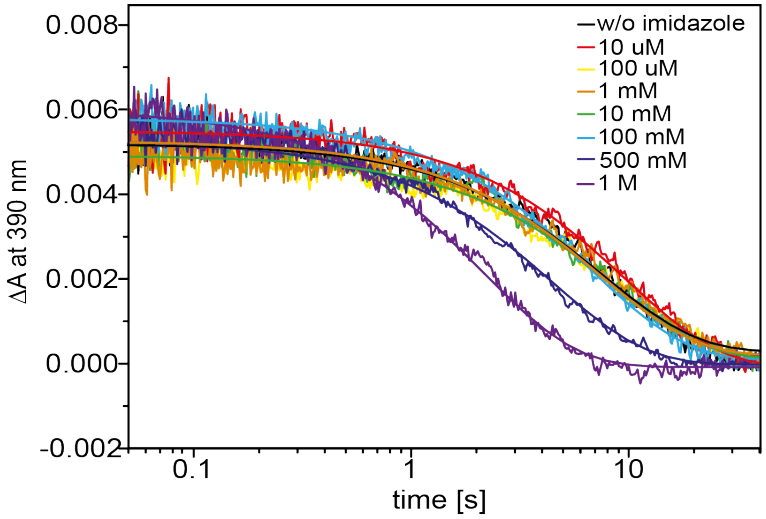

$c_{imidazole}$ [M]	τ_1 [ns]	τ_2 [s]
0	786±26	7.6±0.5
10^{-5}	659±18	9.8±0.8
10^{-4}	657±16	7.6±0.7
10^{-3}	671±18	8.4±0.7
10^{-2}	623±15	7.5±0.6
0.1	639±17	6.8±0.5
0.5	515±15	4.5±0.3
1	664±21	2.1±0.2

Figure 5.18: Decay of LOV_{390} of mPAC $\Delta 457-483$ in dependence of imidazole concentration. The different traces show the kinetics with the corresponding mono exponential decay fits (lines) for a sample without (black), with 10 μM (red), 100 μM (yellow), 1 mM (orange), 10 mM (green), 100 mM (bright blue), 500 mM (dark blue) and 1 M (purple) imidazole at 20 °C. The determined time constants are listed in the table on the right.

5.6 Reaction of the LOV domains

Vibrational spectroscopy is the ideal method to follow structural changes of proteins as well as their chromophores. Therefore the steady-state difference spectra of three different LOV domains were recorded. They all show the differences between the dark state LOV_{445} (negative bands) and the long lived intermediate LOV_{390} (positive bands). For a better view the spectra were split into three different wavenumber regions (see fig. 5.19, 5.20, 5.21).

Figure 5.19 shows the region between 1800 and 900 cm^{-1}. This region contains the amide I and amide II region as well as the so-called fingerprint region. Although the spectra of YF1, aureochrome 1 and mPAC $\Delta 457-483$ reveal certain differences a number of bands can be assigned to the LOV domain. The spectra share the following positive bands at 1725, 1426, 1377, 1304, 1191, and 1092 cm^{-1} and negative peaks at 1715, 1695, 1583, 1551, 1404, 1351, 1273, 1248, 1223, and 1083 cm^{-1}. These vibrations are related to FMN vibrations as shown in table 5.4. However, the spectra show several differences, mostly located in the amide I and amide II region (dark and light grey). This region is

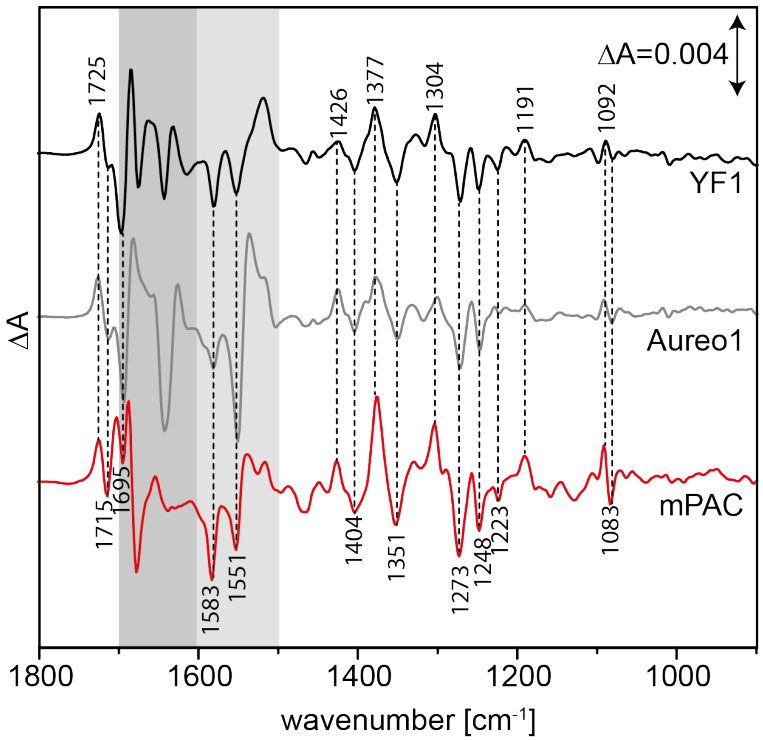

Figure 5.19: Steady-state light-minus-dark difference spectra of YF1 (black line), aureochrome 1 (grey line) and mPAC $\Delta 457 - 483$ (red line) in the region between 1800 and 900 cm^{-1}. Bands that appear in all spectra are labeled with wavenumbers and dashed lines. The grey fields represent the area where vibrations from the protein backbone occur, amide I (dark grey) and amide II (light grey), respectively.

Table 5.4: Vibrational assignment of FTIR difference bands of LOV domains

Infrared difference bands of the LOV_{390} (pos) and the LOV_{450} (neg) intermediate		
pos	neg	vibrational assignment
1725	1715	symmetric C=O stretch (mainly νC(4)=0)
	1695	symmetric C=O stretch (mainly νC(2)=0)
	1583	mainly νC(4a)=N(5) with νC(10a)=N(1)
	1551	νCN, νCC(ring I, 8b)
1426	1404	νC(4)-N(3), νC(4)-C(4a), νC(2)-N(3), δC(9)-H, δC(4)=O
1351	1304	νC(10a)-N(10), νC(1)-C(10), νC(5a)=C(9a), νC(10a)=C(4a)
	1273	mainly δC(6)-H and δC(9)-H with contributions of νN(1)-C(2), νN(3)-C(4)
	1248	νC(4)-N(3), νC(2)-N(3), νC(4)-C(4a), νC(2)-N(1), δC(2)=O
	1223	νC(7)-CH_3, νC(10a)-C(4a), νC(1)-N(10), νC(9a)-N(10), νC(2)-N(3)
1191		vibrations of the ribityl moiety
1092	1083	probably νP-O-Alkyl

sensitive for structural changes of the peptide backbone. The YF1 chimera protein consists of the LOV domain of YtvA from *Bacillus subtilis* and the effector domain of FixL from *Bradyrhizobion japonicum* that functions as histidine kinase [83]. Aureochrome 1 contains a bZIP domain as its effector domain that binds DNA and probably acts as transcription factor. mPAC is a photoactive adenylyl cyclase that catalyzes the reaction of ATP to cAMP. The variety in effector domains gives rise to the observed differences in the amide I and II region (see fig. 5.19 grey areas). However, also vibrations of the FMN chromophore are visible in this region, for example the negative peaks at 1583 and 1551 cm^{-1}.

All LOV domains form the adduct state LOV_{390} after light absorption that is characterized by a covalent bond between a nearby cysteine and the C4a atom of the isoallaxazine ring. Because the region between 2500 and 2600 cm^{-1} is sensitive for S-H vibrations, it is possible to follow this band formation by IR spectroscopy. The S-H vibration of the cysteine in the ground state LOV_{450} gets lost in the LOV_{390} intermediate and appears as a negative band in the light minus dark spectrum (see fig. 5.20). These bands are assigned to C65 in YF1, C254 in aureochrome 1, and C197 in mPAC.

The frequency of the band is sensitive to outer coordination sphere. Thus, a hydrogen bond formed between S-H and a nearby residue shifts the frequency to higher energies, or lower wavenumbers. Like expected all LOV proteins show a negative band in the S-H stretching region. However, their minima vary by about 10 cm^{-1}. Especially the S-H vibration in the aureochrome 1 spectrum is shifted to lower wavenumbers. Normally, S-H stretching frequency in other LOV domains occurs around 2570±2 cm^{-1} [84, 15]. The surrounding of the cysteine in the FMN binding pocket is mainly composed of hydrophobic amino acids and a hydrogen bond can only been formed with N(5) of the isoallaxazine ring of the FMN that is nearby. In the crystal structures the distance is about 3.8 Å in aureochrome 1. Bednarz et al. observed a small shoulder in the S-H stretching band in the light-minus-dark difference spectrum of LOV1 from phototropin from *Chlamydomonas reinhardtii*. They fitted the peak with two bands with a minimum at 2570 and 2562 cm^{-1}, corresponding to two different rotamers of C57. Based on the crystal structure the distance of the two rotamers to the N(5) was determined to be 3.9 and 3.5 Å. The reduced distance of one rotamer to N(5) strengthens the hydrogen bond between S-H and the nitrogen atom and shifts the vibration to lower frequencies. A similar effect is observed for the cysteine of mPAC $\Delta 457 - 483$. While the bands of aureochrome 1 and YF1 can be fitted with one Gaussian function, the negative signal in the difference spectrum of mPAC $\Delta 457 - 483$ is asymmetric and can only be described by two Gaussian functions, like in phototropin LOV1. The minima of the Gaussian functions are 2558 and 2573 cm^{-1} with a full width at half maximum (FWHM) of 12 and 15 cm^{-1}, respectively. The relative area of the two vibrational bands is 12 and 88 %. Therefore two conformers in mPAC $\Delta 457 - 483$ seems likely as well.

The region between 2800 and 3800 cm^{-1} shows the C-H stretching vibrations of alkyl side chains, the amide A/B, and also O-H stretching of alcoholic residues and water molecules that are trapped inside the molecules, so-called dangling water. The interpretation of bands in this region is difficult because of the overlapping water band. However, like in the other regions the three LOV domains share several difference bands even in this region. YF1 and mPAC $\Delta 457 - 483$ share negative bands around at 3496/3499 and at 3358 as well as at 3283, while these bands are lacking or are shifted in the aureochrome 1 spectrum. Overall the aureochrome 1 spectrum is quite different in this region. This finding supports the special character of this LOV protein.

All three spectra share a positive band above 3600 cm^{-1} that differs slightly in its maximum of about 20 wavenumbers. This region is prominent for O-H stretching vibrations of weakly bound water molecules. The mPAC $\Delta 457 - 483$ spectrum additionally shows a smaller negative one at 3657 cm^{-1}. The FTIR difference spectrum of phy3-LOV2 showed a positive band at 3621 cm^{-1} that was assigned to an internal water molecule nearby FMN [85]. To proof that the difference band of mPAC $\Delta 457 - 483$ also corre-

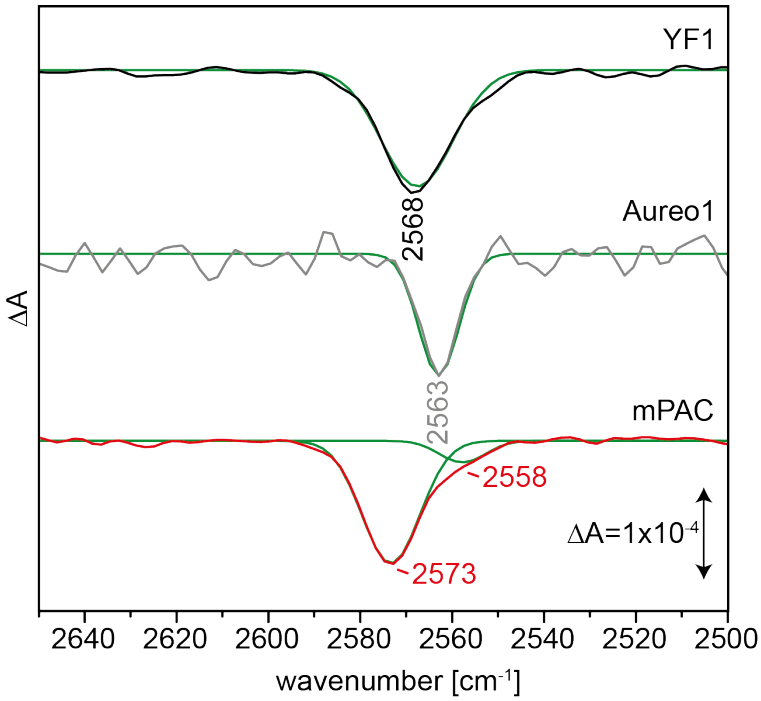

Figure 5.20: Steady-state light-minus-dark difference spectra of YF1 (black line), aureochrome 1 (grey line) and mPAC $\Delta 457 - 483$ (red line) in the region between 2650 and 2500 cm^{-1}. In this region only S-H stretching vibrations occur. The negative band in each spectrum corresponds to the S-H stretching vibration in the ground state of the active cysteine that forms a covalent bond in the adduct state and therefore disappears.

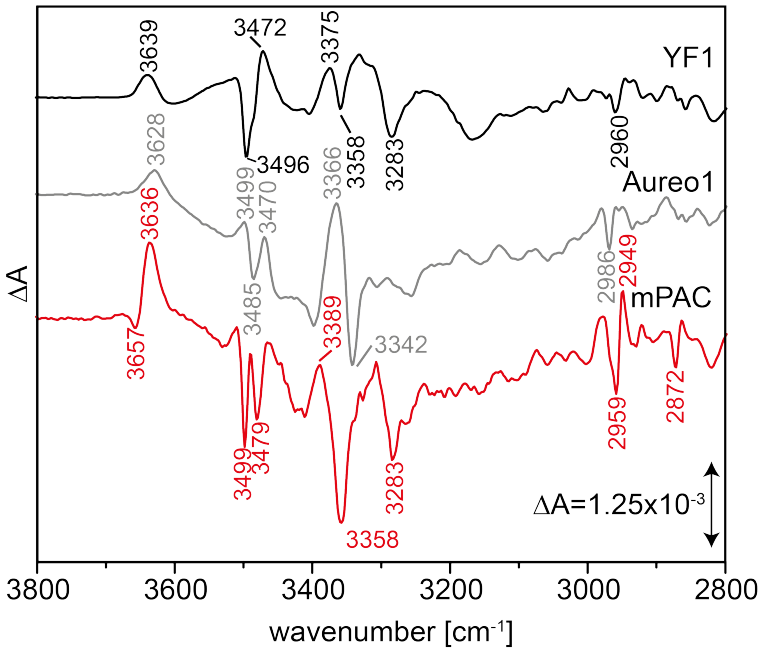

Figure 5.21: Steady-state light minus dark difference spectra of YF1 (black line), Aurochorme 1 (grey line) and mPAC $\Delta 457 - 483$ (red line) in the region between 3700 and 2800 cm^{-1}. In this region only changes in the amide A and B and the C-H stretching vibrations occur.

sponds to internal water, FTIR difference spectra in D_2O and $H_2^{18}O$ were recorded (see fig. 5.22). In the D_2O sample the peak of the putative water shifts from 3657/3636 to 2705/2694 cm^{-1}. That corresponds to an H/D exchange of an O-H group. Additionally the S-H band shifts from 2572 to 1870 cm^{-1}, a typical frequency of a S-D vibration. At 2572 there is still a small band of the S-H stretching. This demonstrate that the H/D exchange was not complete and a few molecules still contain a C197 protonated with a $^1H^+$. To proof if the band at 3657/3636 cm^{-1} is caused by a dangling water like in phototropin, the water in the film was exchanged by $H_2^{18}O$. The rehydration with $H_2^{18}O$ will only influence vibrations of water but not that one corresponding to O-H stretching vibrations of alcohol side chains. The spectrum shows a small shift of about five wavenumbers for the 3636 cm^{-1} peak and a shift of one wavenumber for the 3657 cm^{-1} band to lower wavenumbers. This shift is not as prominent as in the phy3-LOV2 domain where a shift of 12 wavenumbers was observed [85], but gives still enough evidence to assign this band to a dangling water molecule. This conclusion is also right for the positive band at 3628 cm^{-1} in the aureochrome 1 difference spectrum that is down shifted by five wavenumbers due to hydration with $H_2^{18}O$ (data not shown).
However, the negative peak is not effected by $H_2^{18}O$ but D_2O exchange. This fact and the much higher intensity of the positive band give rise to the assumption that the band

of the dangling water overlaps with a difference band of a O-H vibration of an alcohol side chain that changes its hydrogen bond strength during the reaction.

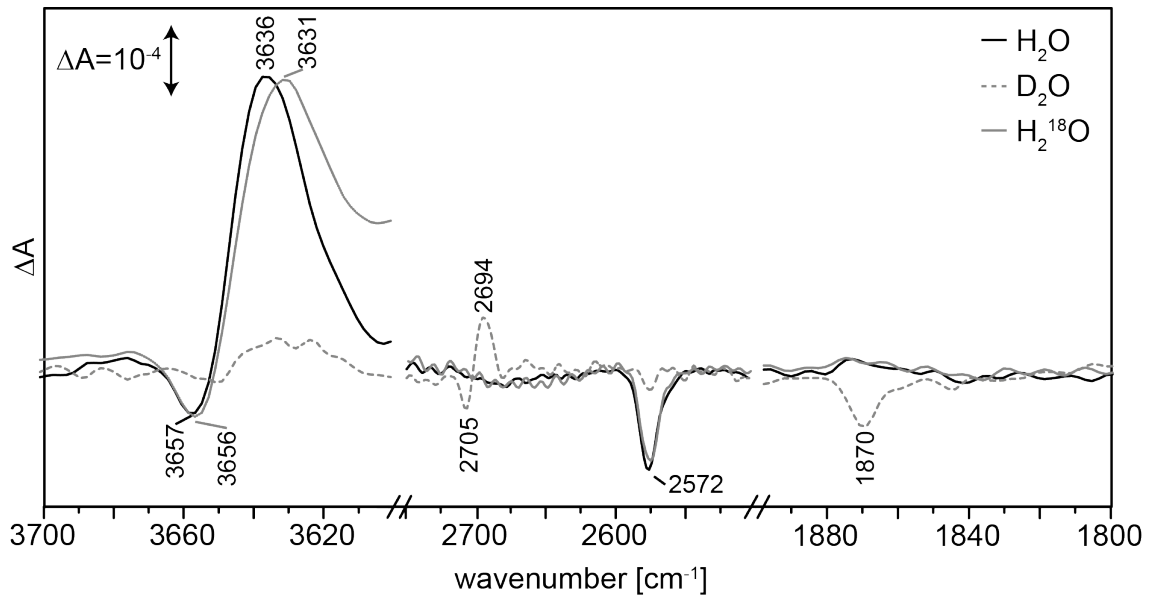

Figure 5.22: Steady-state light minus dark difference spectra of mPAC $\Delta 457 - 483$ in H_2O (black line), D_2O (dashed grey line) and $H_2^{18}O$ (grey line) (black line). The regions of dangling water molecule and the S-H/S-D stretching are shown.

The region between 1800 and 900 cm^{-1} gives additional information when the spectra of mPAC $\Delta 457 - 483$ in H_2O, D_2O and $H_2^{18}O$ are compared. The corresponding difference spectra are shown in figure 5.23. The $H_2^{18}O$ exchange leads to no significant changes while the D_2O exchange shows minor changes. In the LOV_{390} intermediate, new positive bands appear at 1639, 1391, 1323 and 1215 cm^{-1}, while the band at 1190 cm^{-1} is shifted upwards to 1194 cm^{-1}. For the ground state the three bands at 1273, 1248 and 1228 cm^{-1} are shifted to higher frequencies to 1275, 1261 and 1227 cm^{-1}. Additionally the band negative band at 1083 cm^{-1} disappears.

5.7 Reaction of the effector domains

To elucidate on the mechanism of the effector domain, FTIR difference spectra in the presence of substrate are recorded. Aureochrome 1 comprises a DNA-binding bZIP domain. Thus, the presence of DNA containing the target sequence TGACGT should influence the light-minus-dark difference spectrum (see fig. 5.24).
The spectra share several similarities, especially in FMN bands. However, some bands are significantly increased in intensity or shifted in their frequencies, while also new bands arise. Signals at 1684, 1655, 1643 and 1550 cm^{-1} almost double their intensities and a

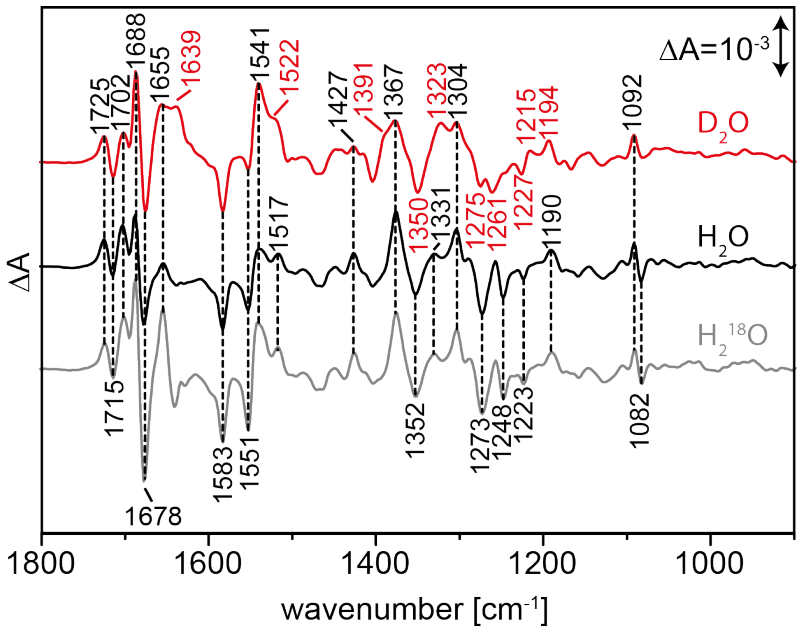

Figure 5.23: Steady-state light minus dark difference spectra of mPAC $\Delta 457 - 483$ in H_2O (black line), D_2O (red line) and $H_2^{18}O$ (grey line) (black line). The bands that are similar in the spectra are marked with dashed lines and the corresponding wavenumbers. The bands shifting upon H/D exchange are marked with red numbers.

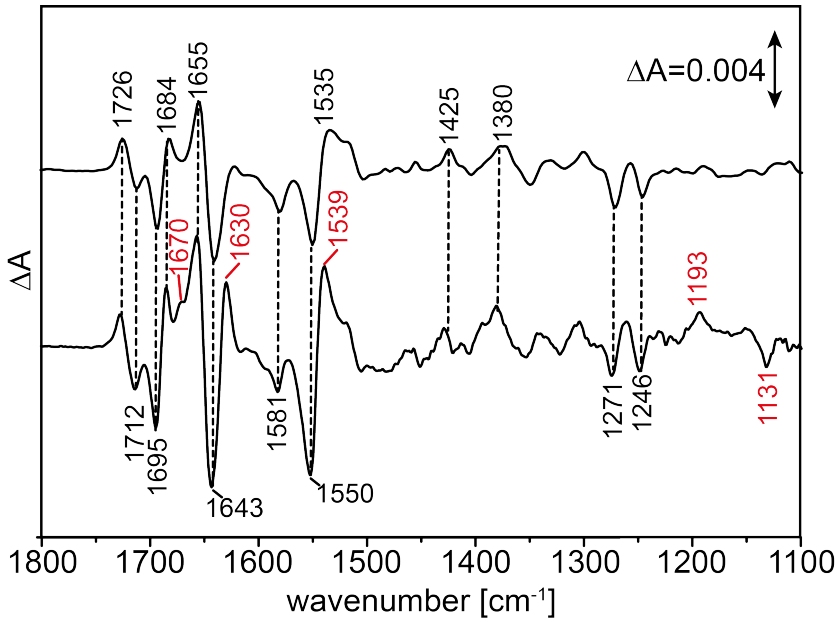

Figure 5.24: Steady-state light-minus-dark difference spectra of aureochrome 1 in the absence (upper trace) and presence of its target DNA. The bands that are similar in the spectra are marked with dashed lines and the corresponding wavenumbers. Signals arising from the DNA binding are marked in red.

shoulder at 1670 cm^{-1} as well as peaks at 1630 and 1539 cm^{-1} appear in the difference spectrum in the presence of DNA. As additional features, the C4=O4 stretching vibration of thymine bases (1671-1655 cm^{-1}) and the C6=O6 stretching vibration of guanine bases (1678-1689 cm^{-1}) appear in this frequency range of amide I [86]. In addition to the shoulder at 1670 cm^{-1}, a positive band rises at 1630 cm^{-1}. These two vibrational bands absorb in the region of the asymmetric and symmetric vibrations of arginine side chains, respectively [87, 88]. A positive band appears at 1539 cm^{-1} which might be indicative for the symmetric N-H deformation vibration of the terminal amino groups of lysine side chains (about 1530 cm^{-1}) [33]. The asymmetric deformation vibration of the NH_3^+ group lies at around 1629 cm^{-1} and overlaps with the symmetric vibrations of arginine residues[35]. In the phosphate/sugar region, two bands at 1193 (pos.) and 1131 (neg.) cm^{-1} appear due to DNA addition. In this region PO_2 stretching vibrations of the DNA backbone occur. The frequency of 1193 cm^{-1} corresponds to P=O stretch of a POOH group, while at 1131 cm^{-1} P-O stretching vibrations with single-bond character are located.

To interpret these changes the binding mechanism will be discussed on the basis of the interaction of General Control Protein 4 (GCN4) to its target DNA. GCN4 from *S. cerevisiae* has a bZIP domain like aureochrome 1 and they share identity in their target sequence:

GCN4:	A	TGAC	TCAT
aureochrome 1:		TGAC	GT

The crystal structure of GCN4 bound to its target DNA was solved in 1992 [40]. The structure unravels the interaction of R243 and N235 (R139 and N131 in aureochrome 1) of the bZIP motif with the DNA bases and backbone. Furthermore, R234 (aureochrome 1: R130) forms hydrogen bonds to the O6 and N7 of the guanine O´ (nomenclature see [40]) and N235 connects the N4 of cytosine 2L´ with the O4 of the thymine 3L. Also other basic amino acids like R232, R234, R241, R245, K246 (aureochrome 1: R128, R130, R137, R141, K142) are involved in the DNA recognition by interaction with the backbone. A sequence alignment of the bZIP domain of aureochrome 1 and GCN4 (see fig. A.3) illustrates that these amino acids are conserved in both proteins. Thus, a similar binding complex is likely. In respect to the FTIR data this mechanism can be confirmed. The interaction between R163 to the C6=O6 could cause the intensity increase of the band at 1684 cm^{-1} assigned to the C=O stretching of the guanine base, while the rise of the band at 1670 cm^{-1} and 1630 cm^{-1} fits well with the position of the asymmetric $\nu_{as}(CN_3H_5^+)$ and symmetric $\nu_s(CN_3H_5^+)$ stretching vibration of arginine side chain [87]. This interpretation is supported by FTIR studies on Ras-specific GTPase activating protein [89]. They assigned a band at 1677 cm^{-1} to an guanidinium group of an arginine

that flips into the binding pocket to interact with γ-phosphate of GTP. However, an overlap with the C=O stretching vibration of asparagine side chain (1677-1678 cm^{-1}) as well as C4=O4 stretching vibration of thymine bases (1671-1655 cm^{-1}) cannot be ruled out. In addition the positive band at 1535 cm^{-1} fits to asymmetric bending vibration of NH_3^+ of lysine side chain [90] and can be assigned to K142 that the differences in the amide I and II bands are detected at around 1650 and 1550 cm^{-1} reflect an influence of the DNA on the structure of the adduct state.
The two signals below 1200 cm^{-1} are located in the region typical for PO_2 stretching vibration. Normally these vibrations are characteristic markers for nucleic acid backbone conformation. However, in a oligo of only 10 base pairs arguable to speak in terms of A-, B- and Z-helical form. P=O stretching vibrations of PO_2H appear between 1180-1240 cm^{-1} while symmetric in phase vibration are measured around 1130 cm^{-1} [91, 92]. From the GCN4 crystal structure it is known that R245 (in aureochrome 1 R164) forms a hydrogen bond with the oxygen of the backbone of guanine (AT**G**ACTCAT) [40]. Thus the infrared bands can be interpreted as a lost of the symmetric stretching vibration of PO_2^- due to the hydrogen bond to the hydrogen of the arginine which leads to a HO-P=O structure and therefore to a rise of a P=O stretching band with full double band character.

Chapter 6

Discussion

6.1 Artificial light-gated KcsA

The optogenetic approach, to use native channels and receptors and modify them by small organic light-sensitive molecules, comprises a number of advantages. For example, this approach circumvents the difficulties that arise from invecting cells and expression of alien proteins. By using organic molecules that imitate natural stimuli like ligands or blockers, light-gated ion channels can be engineered.
Tetraethylammonium (TEA) is a well known blocker of all types of potassium channels [53]. Connecting this group to a photosensitive azobenzene moiety creates a photochromic ligand that is able to block potassium channels in its *trans* configuration [56]. In order to understand the function of these photochromic blockers in the openening and closing of potassium channels, the KcsA, a minimal potassium channel, is build up in an artificial membrane and observed by infrared and impedance spectroscopy.
The expression and purification of KcsA and its variant led to samples containing the functional tetramer in high quality that was demonstrated clearly by the tetramer band in the SDS gel that even appears when the sample was treated with a harsh detergent like sodium dodecyl sulfate and heated up for 5 min to 95 °C.
Surface-enhanced infrared spectroscopy (SEIRAS) combines infrared spectroscopy of a monolayer with an electrochemical setup. Former studies have shown that proteins can be bound to the surface via a Ni-NTA layer [73]. This leads to an oriented monolayer of membrane protein embedded into a lipid bilayer. To apply this technique to the KcsA, the channel was expressed in *E.coli* with a C-terminal His-tag. The expression and purification via an affinity chromatography resulted in a sufficient amount and purity of the KcsA tetramer (see chapter 5.1). The remaining steps of building the Ni-NTA monolayer on the gold surface are well documented in existing literature. Binding of KcsA tetramer was follwed by IR spectroscopy that took about 5 h. Thereafter the

KcsA was reconstituted by building up a lipid bilayer of POPC and POPG, phosphate lipids that are crucial for channel function [93].
The binding of photochromic blockers was executed for BzAQ. The infrared spectrum provided evidence that the organic molecule bound to the surface and also stayed in the vicinity after several washing steps. Furthermore, switching between *cis*- and *trans*-conformation by two different LEDs led to an expected difference spectrum that was fully reversible (see fig. 5.7). However, impedance measurements of the system showed an inverted behaviour of the photoswitch. Instead of a decrease in membrane resistance due to the opening of the channel in the *cis* configuration, the resistance increased and the bilayer became more dense and tight. Thus, hinting at the possibility that the photoswitch may not have bound to the channel. This hypothesis was supported by FTIR data from the binding of the photoswitch to the surface. The SEIRAS depicted, in addition to the positive band assigned to Benzoyl-Azo-Quarternary ammonium (BzAQ), negative bands in the region of the phospholipids. This observation confirmed that the BzAQ tends to bind inside the lipid bilayer, probably due to its hydrophobic tail. If we assume a binding inside the lipid bilayer the hydrophobic tail and azobenzene points into the hydropobic fatty acid chains, while the TEA headgroup binds at the interface of the membrane (see fig. 6.1). POPC and POPG are unsaturated lipids, both containing one fatty acid that exhibit a double bond. This particular fatty acid has a kink, making the lipid more bulky than its fully-saturated counterparts. The geometry of the unsaturated lipids probably led to not densly packed bilayer with small cavities. The experiments indicated that the membrane resistance increase when the BzAQ is in the *cis* configuration suggesting BzAQ could fill the cavities more efficiently in this conformation than when it was in its *trans*.

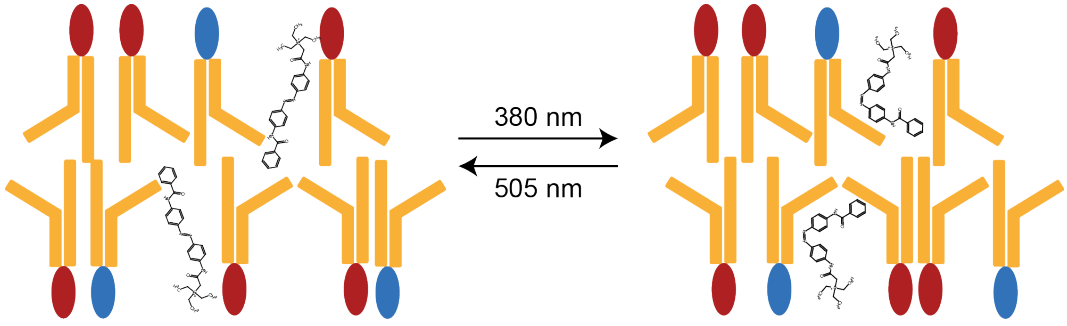

Figure 6.1: Model of BzAQ binding inside the POPC/POPG bilayer. The BzAQ is depicted schematically by its chemical structure, while the lipids are illustrated as models with the fatty acids colored in orange and the headgroups in blue (POPC) and red (POPG). When the BzAQ is switched to its *cis* conformation, it is smaller and fits better into the cavities created by the kinked fatty acids, while in the *trans* conformation it behaves as a rigid stick, pointing into the bilayer.

The SEIRAS experiments demonstrated that the affinity of the BzAQ to the KcsA

channel was too low. Thus, building an artifical light-gated channel on the SEIRAS surface failed. However, the group of Prof. Trauner at the Ludwig-Maximilian-University in Munich reported photoswitches that differ in their chemical groups that are attached to the azobenze moiety [71, 70]. In order to determine binding constants of the photoswitches to the KcsA microscale thermophoresis (MST) measurements were performed. The data suggested that the binding affinity is quite low for all the four photoswitches, at times almost not detectable. The K_D of the photoswitches to the solubilized KcsA in DDM micelles were around 1 mM, corresponding to a very poor binding. Therefore an alternative approach was attempted to build an artificial light-gated KcsA. Accordingly to the former created synthetic photoisomerizable azobenzene-regulated K^+ (SPARK) the KcsA was modified with a cysteine at position P55 to covalently bind maleimide-Azo-Quaternary ammonium (MAQ) to it. MAQ possesses a maleimide group on one end of the azobenzene that can react with cysteine side chains. The covalently bound photoswitch can then reach the external TEA binding site in its *trans* conformation, while in its *cis* conformation the length of the switch is to short to block the channel.

To replace P55 by a cysteine the codon code CCG was replaced by TGC via a quick exchange protocol. Sequencing of the plasmid confirmed the point mutation, so that expression of the P55C variant was performed accordingly to the wild type. The presence of the surface exposed cysteine necessitated the addition of DTT or TCEP as reduction reactant to the purified protein. In the absence of any reduction reactants, the variant started to aggregate and denature at higher concentrations. Building the KcsA P55C reconstituted in POPC/POPG double layer functions with the same efficency as for the wild type. However, the binding of MAQ to the surface showed distinct differences in comparison to BzAQ (see fig. 5.8). There was no evidence of negative bands corresponding to lipids such as C=O and C-H stretch, suggestiong that the photoswitch has not been incorporate into the lipid bilayer.

After washing the surface MAQ stays bound showing typical difference spectra during swtiching by LEDs. While the switching was reversible, the resulting bands were much lower in intensity due to the smaller amout of bound MAQ, making only the strongest bands detectable. Additionally there were bands observed below 1450 cm^{-1} that were absent in the BzAQ spectrum. These spectral bands possibly resulted from the Ni-NTA linker [73]. A precice assignment is difficult because the absorption of the silicon prism led to a higher noise level in the region of the spectrum where the bands appeared.

To observe the opening and closing of the channel at different pH and with different configuration of the MAQ impedance spectra were recorded. The data indicated that at pH 7, the membrane resistances were about 5 times lower compared to the KcsA reconstituted into lipids before the addition of the photoswitch, while the capacity of

the membrane stays stable in the presence of MAQ. As expected, Decreasing the pH to 4 led to a further decrease of the membrane potential. Switching of the MAQ in its *trans* configuration at pH 4 did not lead to changes in any of the fitted parameters. The membrane resistance of the closed KcsA channel embedded in the POPC/POPG monolayer was not restored by blocking the channel with the tetraethylammonium group. This suggests that either the photoswitch did not react with the cysteine and therefore did not bind to the intended binding site at C55 or the inserted cysteine is too far away from the selectivity filter such that the MAQ could not reach the external blocking site even in its *trans* configuration. To prove the first hypothesis MAQ and KcsA P55C mutant were mixed in a batch and afterwards purified via a size exclusion column. The experiment showed that almost no KcsA P55C with a covalently bound MAQ could be purified. This is probably caused by fast degeneration of the reactive maleimide group due to storage.

6.2 Blue-light receptors

6.2.1 Aureochrome 1

Aureochromes from *Vaucheria frigida* are blue-light receptors that control photomorphogenesis in the stramenopile algea. Sequence comparison revealed that aureochrome 1 and aureochrome 2 consists of a light-, oxygen- and voltage-sensitive domain as well as a bZIP domain that binds double stranded DNA with the sequence TGACGT. In this work moleculare spectroscopy was utilized to investigate the primary photoreaction of the full-length aureochrome 1. The visible absorption spectrum indicated that the LOV domain of aureochrome 1 is similar to the LOV2 domain and to YtvA. Time-resolved UV/Vis measurements were performed to determine the kinetics of the photocycle intermediates. The decay of the LOV_{715} triplet state was characterized by a time constant of 1.4±0.2 μs. This value is in agreement with time constant obtained from light-induced transient-grating (TG) spectroscopy, which is 2.8 μs [28], and is in the range of other LOV domains like phototropin1 LOV1 (4 μs), LOV2 (1.9 μs) and YtvA (2 μs) [80, 19, 81]. Unfortunately, it was impossible to record the rise kinetics of the LOV_{390} state because the triplet state, LOV_{715}, exhibits an absorption in this region that negates former changes [8]. The time constant of the decay of LOV_{390} was determined to be 22 min which is in excellent agreement with the time constant of the LOV-Jα construct [27]. This value is higher than previously reported half-life times of the truncated variants of aureochrome 1 by Takahashi and Mitra, which were 4.9 min and 9 min, repectively [7, 24]. We conclude from these experimental results that the presence of the bZIP domain prolongs the life time of the signaling state LOV_{390}.

FTIR difference spectroscopy clarified the LOV_{390} as the adduct state with the typical bands of the FMN chromophore in the range between 1000-1800 cm^{-1}. The spectrum shares several similarities with other LOV protein spectra such as YF1, mPAC as well as phototropin and YtvA [94, 84]. In the amide I and amide II region, however, the spectra differ from each other due to their different effector domains. The FTIR spectrum is sensitive to structural changes that appear mostly as bands in this region due vibrational changes of the protein backbone. Unfortunately it is impossible to assign these vibrational changes to specific regions of the molecule. For further investigation of the conformational changes occuring during the photocycle by FTIR the vibrational Stark effect could be employed. This effect describes changes of a vibrational frequency due to changes in the local electric field. Insertion of Stark probes at different position in the protein could elucidate structural changes within the protein.

For aureochrome 1 the typical negative band around 2565 cm^{-1} is due to the covalent bond formation of the cysteine 254 and the isoalloxazine ring (see fig. 5.20). The

band position at 2563 cm^{-1} is quite low in comparison to other LOV domains. The downward shift of about 7 cm^{-1} suggests a strongly hydrogen bonded S-H vibration. In previous FTIR studies of the LOV1 domain of phototropin 1 from *Chlamydomonas reinhardtii* a asymmetric S-H difference band was observed [84]. The peak was fitted to two Lorentzians with minima at 2570 and 2562 cm^{-1} and a relative area of 74 and 26 %. It was concluded that these two bands corresponds to the two rotamer conformations of C57. One of the rotamers is closer to FMN (the distance between S to N5 is 3.5 Å instead of 3.9 Å[11]) and forms a stronger hydrogen bond than the other. The band position in the aureochrome 1 spectrum at 2563 cm^{-1} suggests that all reactive cysteines are in the rotamer conformation that is closer to FMN and thus have a stronger hydrogen bond. While the crystal structure of the aureochrome 1 LOV domain does not reveal electron density for two rotamer configurations of C254 [7], the resolution of this structure with 2.8 Å, which is lower in comparison to the one of phototropin LOV (1.9 Å) [11]. It is possible that the second rotamer might not be resolved.

Previous studies have already demonstrated that aureochrome 1 forms dimers in the dark as well in light. However, it is still under debate which part of the protein is critical for dimerization. Herman et al. showed by size exclusion chormatography that dimerization under blue-light takes place for a construct carrying the LOV domain with the Jα helix (LOV-Jα) and not for the truncated LOV domain [27]. On the other hand measurements by Hisatomi et al. proposed the LOV-Jα construct to be monomeric [26]. However, both agree together with Toyooka, who performed transient-grating measurements, on that aureochrome constructs carrying the bZIP domains as well as full-length aureochrome are dimers even in the dark [28]. This result agrees well with the structure for bZIP proteins that form a coiled coil structure by their leucine zipper consisting of hepta repeats of the aliphatic amino acid. The dimerization allows the basic region located upstream to the leucine zipper to make contacts with the DNA at its major grove.

To elucidate the binding mechanism for aureochrome 1 the FTIR difference spectrum of full-length aureochrome 1 was recorded in the presence of a DNA oligo carrying the target sequence TGACGT. The vibrational intensities and frequencies are sensitive to changes in their environment, for example formation of H-bonds, strengthening or weakening of H-bonds, protonation reactions, and conformational changes. Thus, the FTIR difference spectrum reveals even subtle changes of single amino acids during a reaction. In the difference spectrum of aureochrome 1 with its target DNA vibrational bands assigned to asparagine side chains as well as to the phosphate-sugar backbone were detected. Following the binding mechanism known from other bZIP domains like GCN4 a binding model is proposed. The interaction formed in the binding complex of

aureochrome 1 and its target DNA are illustrated in figure 6.2. It shows the binding complex of the dimeric bZIP domain with the oligonucleotide strand modeled on the basis of the crystal structure of GCN4 (PDB:1YSA, [40]).

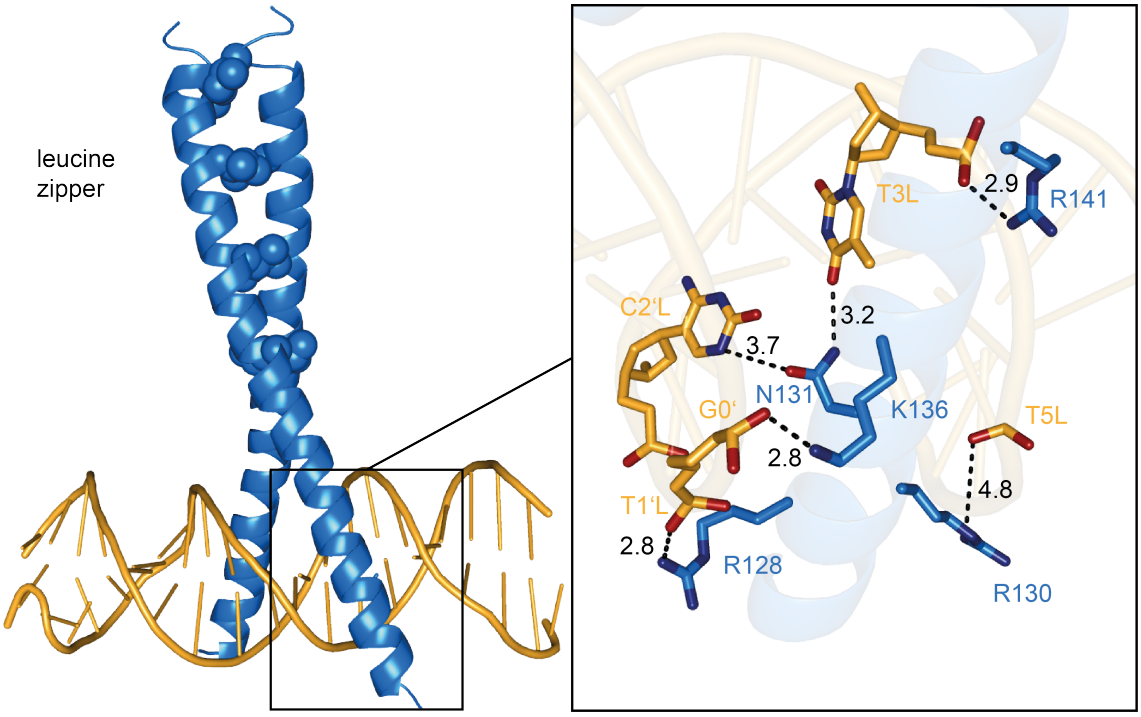

Figure 6.2: Homology Model of aureochrome 1 interacting with its target DNA strand. The structure was modeled on the basis of the GCN4 crystal structure (PDB:1YSA, [40]) with the software SWISS-MODEL [42, 43]. The figure on the left depicts the overall binding complex. The basic region is magnified and illustrated with licorice representation on the right. The nucleobasis are shown in orange and the amino acid side chains are shown in blue. The important H-bonds are indicated as dashed lines along with their distances.

Figure 6.2 summarizes the interactions between the basic region of aureochrome 1 and its target DNA as inferred by FTIR spectroscopy. The spectral bands of the asymmetric and symmetric vibrations of arginine side chains confirmed that these residues form hydrogen bonds to the phosphate backbone as shown for R128, R130 and R141. Further evidence of these interactions arise from the observed phosphate bands below 1200 cm^{-1}. The loss of the asymmetric P-O stretching vibration (neg. band at 1131 cm^{-1}) due to these interactions lead to an increase of the double bond character in the P=O bond (pos. band at 1193 cm^{-1}) the oxygen of which does not act as an H-bond acceptor for the arginine. Addtitonally, K142 interacts with the phosphate backbone of guanine (TAT**G**ACTG) and therefore a additional band of the assymmetric stretching vibration of the NH_3^+ appears at 1539 cm^{-1} (see fig. 5.24). However, for a detailed assignment of these difference bands to a particular lysine, systematic variant studies are required. Unforunately mutations of amino acids that are crucial for DNA

recongnition can lead to complete loss of binding and therefore can be a challenging task. Nevertheless, the FTIR data demonstrate that a light-induced binding takes place during the lifetime of the LOV_{390} intermediate and that this adduct state is the signalling state of aureochrome 1.

6.2.2 mPAC

mPAC is a recently discovered photoactivated adenylyl cyclase from the cyanobacterium *Microcoleus chthonoplastes*. This protein is unique because it is the first known photoactivated adenylyl cyclase (PAC) that reveals a LOV domain as light-sensitive domain. Typically, PAC use a BLUF domain for sensing light. mPAC $\Delta 457-483$ was expressed and purified from *E. coli* cells with a high yield. However, after purification via the His-tag column technique, the purity was not sufficient for spectroscopic analysis. Thus, a second purification step using size exclusion chromatography was necessary. Finally a protein sample with a ratio of A_{450}/A_{280} of about 10 was achieved that is close to the theoretical value of 7,1 of a fully chromophore assambled protein. However, purification step via SEC leads to a high loss percentage of sample (80 %) possibly due to the interaction of the protein with the active sites of the column material. These circumstances can be avoided by saturating the column with "conditioning" protein before using or minimizing the binding of mPAC $\Delta 457-483$ to the column by addition of EDTA to the sample in the future.

The LOV domain of mPAC $\Delta 457-483$ undergoes a photocycle when it is activated by a blue photon. The kinetics of the intermediates of the photocycle were observed by flash photolysis. The photocycle contains, besides the ground state, two intermediates, LOV_{715} and LOV_{390}. The formation of the triplet state LOV_{715} after excitation of the ground state takes place within a few nanoseconds as shown for other LOV domains [9] and is too fast to detect for our experimental setup. The decay of triplet state was determined to be 670±112 ns. In comparison to other LOV domains like aureochrome 1 (1.4 μs), phototropin1 LOV1 (4 μs), LOV2 (1.9 μs) and YtvA (2 μs) [80, 19, 81] the decay of mPAC $\Delta 457-483$ is significantly faster. However, Kottke et al. observed in their studies a second triplet species $LOV1_{715a}$ that decays to the adduct state within 800 ns [80]. These two triplet states, that cannot be distinguished by their absorption spectra, were assigned to two different conformers supported by FTIR data from Bednarz et al. [84]. The FTIR difference spectrum of mPAC $\Delta 457-483$ suggested to two rotamers of the cysteine. The negative S-H stretching peak in the mPAC $\Delta 457-483$ difference spectrum (see fig. 5.20) was asymmetric as well, like in LOV1 of phototropin. A fit to two gaussian functions with minima at 2558 and 2573 cm^{-1} was satisfactory. The relative area of the two vibrational bands were 12 and 88 % which is consistent with the presence of the two conformers. However, the fit of the kinetics of the triplet state decay was monoexponential and did not show any evidence of a second species.

The mechanism of adduct formation is still under discussion. Recent studies suggested a reaction pathway via a neutral radical, in which either a hydrogen atom transfer or electron transfer followed by a proton transfer occurs before bond formation to the

nearby cysteine [17]. In both cases the distance between the isoalloxazine ring and the cysteine 194 will influence the kinetics of bond formation. Thus the fast decay kinetics of the triplet state as well as the low frequency of one cysteine band at 2558 cm^{-1} suggest that the cysteine is in close vicinity in one of its rotamer conformation. However, in order to prove this hypothesis a model based on a crystal structure will be helpful.
The recovery of the ground state takes place by thermal decay of the adduct state due to strained protein conformation. This decay varies by several order of magnitude between different species [5]. Previously studies have shown that the decay of the adduct state can be accelerated by a base catalyzed mechanism [82]. It was proposed that imidazole as well as other hydrophobic bases can enter a cavity of the PAS fold close to the FMN. The base can abstract the proton from the FMN N(5) atom, leading to a double bond formation between N(5) and C(4a) and thus to a breakage of the C(4a)-S bond. To investigate if this mechanism is possible in the LOV domain of mPAC $\Delta 457-483$, the kinetics of the adduct decay was studied with different imidazole concentrations. The kinetics were unaffected by the imidazole concentration up to 100 mM (see table in figure 5.18). Thus, either the adduct decay in mPAC $\Delta 457-483$ takes place via a different mechanism or there is no cavity in the FMN binding pocket that is accessible from outside. In the LOV2 domain of phototropin from *Chlamydomonas reihardtii* and *Avena sativa*, base catalysis in the absence of any external bases is proposed to take place via a particular histidine residue at the surface and an intramolecular water molecule [82, 8]. However, this specific histidine is not conserved in the LOV domain of mPAC $\Delta 457-483$. Furthermore, no other basic amino acids are in close vicinity to FMN chromophore (distance <15 Å) considering a SWISS model of the LOV domain based on the LOV1 domain of phototropin from *Chlamydomonas reinhardtii* (PDB:1N9L, [11]). Therefore the base catalyzed mechanism cannot be responsible for the fast decay of the adduct state of the LOV domain of mPAC $\Delta 457-483$. It is probable that the strained protein conformation has a critical role in these types of LOV domains and is responsible for the bond breakage between C(4a) and the sulfur of C194.
The FTIR data shows the typical features of a LOV domain with expected differences in the amide I and II region due to the diversity of the effector domains in LOV proteins. Surprisingly the mPAC $\Delta 457-483$ difference spectrum of the LOV_{390} minus LOV_{450} states reveals an additional negative band close to the band of the intrinsic water at 3636 cm^{-1} that is visible in all other LOV domains (aureochrome 1: 3628 cm^{-1}, YF1: 3639 cm^{-1}; see fig. 5.21). However, due to band broadening of loesly bound water, there is no negative peak visible that can be assigned to the same water molecule in the dark state.
To investigate whether the negative signal in mPAC $\Delta 457-483$ arises from a second

dangling water, a sample rehydrated with $H_2^{18}O$ was prepared. By calculation of the second derivative of the spectra, only two peaks in this area are obtained. A fit with two Gaussian peaks with a minimum at about 3653 cm^{-1} and with a maximum at 3641 or 3633 cm^{-1} for H_2O and $H_2^{18}O$, respectively. The shift of the positive band by eight wavenumbers clearly assigns it to an internal water molecule, while the negative band, which does not undergo a vibrational shift due to $^{16}O/^{18}O$ exchange, corresponds to an O-H stretch of an alcoholic side chain (see fig. 6.3). This change in an alcoholic side chain is characteristic for mPAC $\Delta 457 - 483$ and was never observed for a LOV protein before, thus we concluded that this residue is part of changes taking place in the adenylyl cyclase domain. Threonine 318 might be a possible candidate, because this residue points into the dimer interface and forms a hydrogen bond to the β-phosphate of the ATP [44]. However, to confirm this hypothesis, site-directed mutagenesis experiments are necessary.

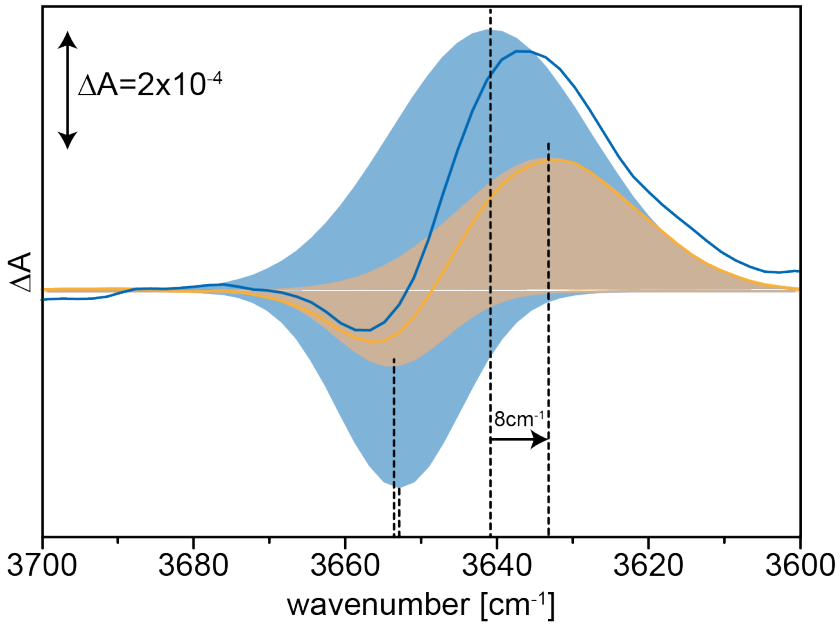

Figure 6.3: Difference bands in the region between 3600 and 3700 cm^{-1} of the baseline corrected steady-state difference spectra of mPAC $\Delta 457 - 483$ in H_2O (blue line) and $H_2^{18}O$ (orange line). Both spectra are fitted by two Gaussian (filled curves with corresponding colours) with peak minima at 3653 cm^{-1} and maxima at 3641 and 3633 cm^{-1} for H_2O and $H_2^{18}O$, respectively. The negative signal corresponds to an O-H stretching vibration of an alcoholic side chain, while the positive bands are assigned to intrinsic an intrinsic water molecule according to Iwata et al. [85].

The structure of mPAC derived from a SWISS-Model on the basis of the crystal structure of phototropin 1 LOV1 domain from *C. reinhardtii* (PDB:1N9L) contains two water molecules in close vicinity to FMN (see fig. 6.4). Those seem to be suitable candidates for the dangling water visibile in the FTIR difference spectrum. Furthermore,

the figure shows the cofactor flavin mononucleotide and the reactive C194 with the two closest water molecules (red spheres). It is likely that these hydrogen bonded water molecules are effected by the reaction and therefore appear in the difference spectrum. However, it is unclear why mPAC $\Delta 457 - 483$ shows two bands in that region while other in LOV proteins like YF1, aureochrome 1 and Phy3-LOV2 reveal just a single band.

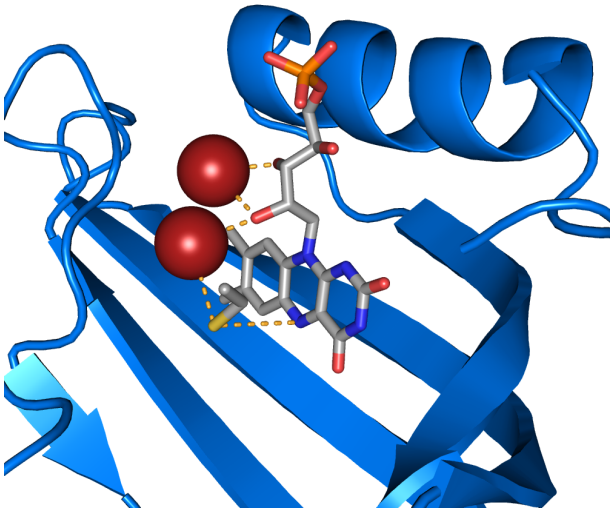

Figure 6.4: Cutout of the SWISS model of mPAC with its chromophore FMN and the reactive cysteine 194 (shown as sticks), as well as the intrinsic water molecules (shown as red sheres). The important H-bond interactions are indicated by the yellow dotted lines. The model based on the structure of phot1 LOV1 domain (PDB:1N9L)[11, 42, 43].

Bibliography

[1] E. Pastrana. Optogenetics: controlling cell function with light. *Nature Methods*, 8(1):24–25, Jan 2011.

[2] G. Nagel, T. Szellas, W. Huhn, S. Kateriya, N. Adeishvili, P. Berthold, D. Ollig, P. Hegemann, and E. Bamberg. Channelrhodopsin-2, a directly light-gated cation-selective membrane channel. *Proceedings of the National Academy of Sciences*, 100(24):13940–13945, Nov 2003.

[3] T. Bruegmann, D. Malan, M. Hesse, T. Beiert, C. J. Fuegemann, B. K. Fleischmann, and P. Sasse. Optogenetic control of heart muscle in vitro and in vivo. *Nature Methods*, 7(11):897–900, Nov 2010.

[4] J. M. Christie. Phototropin blue-light receptors. *Annual Review of Plant Biology*, 58(1):21–45, Jun 2007.

[5] A. Losi. Flavin-based blue-light photosensors: A photobiophysics update. *Photochemistry and Photobiology*, 83(6):1283–1300, Nov 2007.

[6] A. S. Halavaty and K. Moffat. N- and c-terminal flanking regions modulate light-induced signal transduction in the lov2 domain of the blue light sensor phototropin 1 from avena sativa. *Biochemistry*, 46(49):14001–14009, Dec 2007.

[7] D. Mitra, X. Yang, and K. Moffat. Crystal structures of aureochrome1 lov suggest new design strategies for optogenetics. *Structure*, 20(4):698–706, Apr 2012.

[8] T. E. Swartz, S. B. Corchnoy, J. M. Christie, J. W. Lewis, I. Szundi, W. R. Briggs, and R. A. Bogomolni. The photocycle of a flavin-binding domain of the blue light photoreceptor phototropin. *Journal of Biological Chemistry*, 276(39):36493–36500, 2001.

[9] J. T. M. Kennis, S. Crosson, M. Gauden, I. H. M. van Stokkum, K. Moffat, and R. van Grondelle. Primary reactions of the lov2 domain of phototropin, a plant blue-light photoreceptor. *Biochemistry*, 42(12):3385–3392, 2003.

[10] S. Crosson and K. Moffat. Structure of a flavin-binding plant photoreceptor domain: Insights into light-mediated signal transduction. *Proceedings of the National Academy of Sciences*, 98(6):2995–3000, Mar 2001.

[11] R. Fedorov, I. Schlichting, E. Hartmann, T. Domratcheva, M. Fuhrmann, and P. Hegemann. Crystal structures and molecular mechanism of a light-induced signaling switch: The phot-lov1 domain from chlamydomonas reinhardtii. *Biophysical Journal*, 84(4):2474–2482, Apr 2003.

[12] C. Neiss and P. Saalfrank. Ab initio quantum chemical investigation of the first steps of the photocycle of phototropin: A model study. *Photochemistry and Photobiology*, 77(1):101–109, May 2003.

[13] E. Schleicher, R. M. Kowalczyk, C. W. M. Kay, P. Hegemann, A. Bacher, M. Fischer, R. Bittl, G. Richter, and S. Weber. On the reaction mechanism of adduct formation in lov domains of the plant blue-light receptor phototropin. *Journal of the American Chemical Society*, 126(35):11067–11076, Sep 2004.

[14] C. W. M. Kay. Blue light perception in plants. detection and characterization of a light-induced neutral flavin radical in a c450a mutant of phototropin. *Journal of Biological Chemistry*, 278(13):10973–10982, Mar 2003.

[15] Y. Sato, T. Iwata, S. Tokutomi, and H. Kandori. Reactive cysteine is protonated in the triplet excited state of the lov2 domain in adiantum phytochrome3. *Journal of the American Chemical Society*, 127(4):1088–1089, Feb 2005.

[16] A. Pfeifer, T. Majerus, K. Zikihara, D. Matsuoka, S. Tokutomi, J. Heberle, and T. Kottke. Time-resolved fourier transform infrared study on photoadduct formation and secondary structural changes within the phototropin lov domain. *Biophysical Journal*, 96(4):1462–1470, Feb 2009.

[17] C. Bauer, C.-R. Rabl, J. Heberle, and T. Kottke. Indication for a radical intermediate preceding the signaling state in the lov domain photocycle. *Photochemistry and Photobiology*, 87(3):548–553, May 2011.

[18] T. Domratcheva, R. Fedorov, and I. Schlichting. Analysis of the primary photocycle reactions occurring in the light, oxygen, and voltage blue-light receptor by multiconfigurational quantum-chemical methods. *Journal of Chemical Theory and Computation*, 2(6):1565–1574, Nov 2006.

[19] A. Losi, B. Quest, and W. Gaertner. Listening to the blue: the time-resolved thermodynamics of the bacterial blue-light receptor ytva and its isolated lov domain. *Photochemical & Photobiological Sciences*, 2(7):759, 2003.

[20] A. Losi, T. Kottke, and P. Hegemann. Recording of blue light-induced energy and volume changes within the wild-type and mutated phot-lov1 domain from chlamydomonas reinhardtii. *Biophysical Journal*, 86:1051–1060, February 2004.

[21] E. Huala, W. R. Oeller, E. Liscum, I. Han, E. Larsen, and W. R. Briggs. Arabidopsis nph1: A protein kinase with a putative redox-sensing domain. *Science*, 278(5346):2120–2123, Dec 1997.

[22] A. Losi, E. Polverini, B. Quest, and W. Gaertner. First evidence for phototropin-related blue-light receptors in prokaryotes. *Biophysical Journal*, 82(5):2627–2634, May 2002.

[23] S. Raffelberg, L. Wang, S. Gao, A. Losi, W. Gaertner, and G. Nagel. A lov-domain-mediated blue-light-activated adenylate (adenylyl) cyclase from the cyanobacterium microcoleus chthonoplastes PCc 7420. *Biochemical Journal*, 455(3):359–365, Nov 2013.

[24] F. Takahashi, D. Yamagata, M. Ishikawa, Y. Fukamatsu, Y. Ogura, M. Kasahara, T. Kiyosue, M. Kikuyama, M. Wada, and H. Kataoka. Aureochrome, a photoreceptor required for photomorphogenesis in stramenopiles. *Proceedings of the National Academy of Sciences*, 104(49):19625–19630, Dec 2007.

[25] M. Salomon, U. Lempert, and W. Riuediger. Dimerization of the plant photoreceptor phototropin is probably mediated by the lov1 domain. *FEBS Letters*, 572(1-3):8–10, Aug 2004.

[26] O. Hisatomi, K. Takeuchi, K. Zikihara, Y. Ookubo, Y. Nakatani, F. Takahashi, S. Tokutomi, and H. Kataoka. Blue light-induced conformational changes in a light-regulated transcription factor, aureochrome-1. *Plant and Cell Physiology*, 54(1):93–106, Jan 2013.

[27] E. Herman, M. Sachse, P. G. Kroth, and T. Kottke. Blue-light-induced unfolding of the jalpha helix allows for the dimerization of aureochrome-lov from the diatom phaeodactylum tricornutum. *Biochemistry*, 52(18):3094–3101, May 2013.

[28] T. Toyooka, O. Hisatomi, F. Takahashi, H. Kataoka, and M. Terazima. Photoreactions of aureochrome-1. *Biophysical Journal*, 100(11):2801–2809, Jun 2011.

[29] S. Ito, A. Murakami, K. Sato, Y. Nishina, K. Shiga, T. Takahashi, S. Higashi, M. Iseki, and M. Watanabe. Photocycle features of heterologously expressed and assembled eukaryotic flavin-binding bluf domains of photoactivated adenylyl cyclase (pac), a blue-light receptor in euglena gracilis. *Photochemical & Photobiological Sciences*, 4(9):762, 2005.

[30] A. Moeglich and K. Moffat. Structural basis for light-dependent signaling in the dimeric lov domain of the photosensor ytva. *Journal of Molecular Biology*, 373(1):112–126, Oct 2007.

[31] R. P. Diensthuber, M. Bommer, T. Gleichmann, and A. Moeglich. Full-length structure of a sensor histidine kinase pinpoints coaxial coiled coils as signal transducers and modulators. *Structure*, 21(7):1127–1136, Jul 2013.

[32] A. Pfeifer, T. Mathes, Y. Lu, P. Hegemann, and T. Kottke. Blue light induces global and localized conformational changes in the kinase domain of full-length phototropin. *Biochemistry*, 49(5):1024–1032, Feb 2010.

[33] B. D. Zoltowski, C. Schwerdtfeger, J. Widom, J. J. Loros, A. M. Bilwes, J. C. Dunlap, and B. R. Crane. Conformational switching in the fungal light sensor vivid. *Science*, 316(5827):1054–1057, May 2007.

[34] P. L. Freddolino, K. H. Gardner, and K. Schulten. Signaling mechanisms of lov domains: new insights from molecular dynamics studies. *Photochemical & Photobiological Sciences*, 12(7):1158, 2013.

[35] M. A. Jones, K. A. Feeney, S. M. Kelly, and J. M. Christie. Mutational analysis of phototropin 1 provides insights into the mechanism underlying lov2 signal transmission. *Journal of Biological Chemistry*, 282(9):6405–6414, Dec 2006.

[36] F. Takahashi, T. Hishinuma, and H. Kataoka. Blue light-induced branching in vaucheria. requirement of nuclear accumulation in the irradiated region. *Plant and Cell Physiology*, 42(3):274–285, Mar 2001.

[37] T. Alber. Structure of the leucine zipper. *Current Opinion in Genetics & Development*, 2(2):205–210, Jan 1992.

[38] C. Vinson, A. Acharya, and E. J. Taparowsky. Deciphering b-zip transcription factor interactions in vitro and in vivo. *Biochimica et Biophysica Acta (BBA) - Gene Structure and Expression*, 1759(1-2):4–12, Jan 2006.

[39] M. Jakoby, B. Weisshaar, W. Droege-Laser, J. Vicente-Carbajosa, J. Tiedemann, T. Kroj, and F. Parcy. bzip transcription factors in arabidopsis. *Trends in Plant Science*, 7(3):106–111, Mar 2002.

[40] T. E. Ellenberger, C.J. Brandl, K. Struhl, and S. C. Harrison. The gcn4 basic region leucine zipper binds dna as a dimer of uninterrupted alpha helices: Crystal structure of the protein-dna complex. *Cell*, 71:1223–1237, 1992.

[41] C. Steegborn, T. N. Litvin, L. R. Levin, J. Buck, and H. Wu. Bicarbonate activation of adenylyl cyclase via promotion of catalytic active site closure and metal recruitment. *Nature Structural Molecular Biology*, 12(1):32–37, Jan 2005.

[42] K. Arnold, L. Bordoli, J. Kopp, and T. Schwede. The swiss-model workspace: a web-based environment for protein structure homology modelling. *Bioinformatics*, 22(2):195–201, Jan 2006.

[43] F. Kiefer, K. Arnold, M. Kunzli, L. Bordoli, and T. Schwede. The swiss-model repository and associated resources. *Nucleic Acids Research*, 37(Database):D387–D392, Jan 2009.

[44] Y. Liu, A. E. Ruoho, V. D. Rao, and J. H. Hurley. Catalytic mechanism of the adenylyl and guanylyl cyclases: Modeling and mutational analysis. *Proceedings of the National Academy of Science*, 94:13414–13419, December 1997.

[45] J. J. G. Tesmer and S. R. Sprang. The structure, catalytic mechanism and reg-

ulation of adenylyl cyclase. *Current Opinion in Structural Biology*, 8(6):713–719, Dec 1998.

[46] Z. Lu, A. M. Klem, and Y. Ramu. Ion conduction pore is conserved among potassium channels. *Nature*, 413(6858):809–813, Oct 2001.

[47] D. A. Doyle, J. M. Cabral, R. A. Pfuetzner, A. Kuo, J. M. Gulbis, S. L. Cohen, B. T. Chait, and R. MacKinnon. The structure of the potassium channel: Molecular basis of k+ conduction and selectivity. *Science*, 280(5360):69–77, Apr 1998.

[48] S. Uysal, V. Vasquez, V. Tereshko, K. Esaki, F. A. Fellouse, S. S. Sidhu, S. Koide, E. Perozo, and A. Kossiakoff. Crystal structure of full-length kcsa in its closed conformation. *Proceedings of the National Academy of Sciences*, 106(16):6644–6649, Apr 2009.

[49] L. G. Cuello, J. G. Romero, D. M. Cortes, and E. Perozo. ph-dependent gating in the streptomyces lividans k + channel. *Biochemistry*, 37(10):3229–3236, Mar 1998.

[50] A. N. Thompson, D. J. Posson, P. V. Parsa, and C. M. Nimigean. Molecular mechanism of ph sensing in kcsa potassium channels. *Proceedings of the National Academy of Sciences*, 105(19):6900–6905, May 2008.

[51] L. G. Cuello, D. M. Cortes, V. Jogini, A. Sompornpisut, and E. Perozo. A molecular mechanism for proton-dependent gating in kcsa. *FEBS Letters*, 584(6):1126–1132, Mar 2010.

[52] S. Uysal, L. G. Cuello, D. M. Cortes, S. Koide, A. A. Kossiakoff, and E. Perozo. Mechanism of activation gating in the full-length kcsa k+ channel. *Proceedings of the National Academy of Sciences*, 108(29):11896–11899, Jul 2011.

[53] L. Heginbotham. Single streptomyces lividans k+ channels: Functional asymmetries and sidedness of proton activation. *The Journal of General Physiology*, 114(4):551–560, Sep 1999.

[54] M. J. Lenaeus, M. Vamvouka, P. J. Focia, and A. Gross. Structural basis of tea blockade in a model potassium channel. *Nature Structural & Molecular Biology*, 12(5):454–459, May 2005.

[55] F. Zhang, J. Vierock, O. Yizhar, L. E. Fenno, S. Tsunoda, A. Kianianmomeni, M. Prigge, A. Berndt, J. Cushman, J. Polle, J. Magnuson, P. Hegemann, and K. Deisseroth. The microbial opsin family of optogenetic tools. *Cell*, 147(7):1446–1457, Dec 2011.

[56] M. Banghart, K. Borges, E. Isacoff, D. Trauner, and R. H. Kramer. Light-activated ion channels for remote control of neuronal firing. *Nature Neuroscience*, 7(12):1381–1386, Nov 2004.

[57] A. Barth and C. Zscherp. What vibrations tell us about proteins. *Quarterly Reviews of Biophysics*, 35(4):369–430, Nov 2002.

[58] W. K. Surewicz, H. H. Mantsch, and D. Chapman. Determination of protein secondary structure by fourier transform infrared spectroscopy: A critical assessment. *Biochemistry*, 32(2):389–394, Jan 1993.

[59] D. M. Byler and H. Susi. Examination of the secondary structure of proteins by deconvolved ftir spectra. *Biopolymers*, 25(3):469–487, Mar 1986.

[60] A. Hartstein, J. R. Kirtley, and J. C. Tsang. Enhancement of the infrared absorption from molecular monolayers with thin metal overlayers. *Physical Review Letters*, 45(3):201–204, Jul 1980.

[61] M. Osawa and M. Ikeda. Surface-enhanced infrared absorption of p-nitrobenzoic acid deposited on silver island films: contributions of electromagnetic and chemical mechanisms. *The Journal of Physical Chemistry*, 95(24):9914–9919, Nov 1991.

[62] M. Osawa, K. Ataka, K. Yoshii, and Y. Nishikawa. Surface-enhanced infrared-spectroscopy - the origin of the absorption enhancement and band selection rule in the infrared-spectra of molecules adsorbed on fine metal particles. *Applied Spectroscopy*, 47(9):1497–1502, SEP 1993.

[63] H. Miyake, S. Ye, and M. Osawa. Electroless deposition of gold thin films on silicon for surface-enhanced infrared spectroelectrochemistry. *Electrochemistry Communications*, 4(12):973–977, DEC 2002.

[64] C. Steinem, A. Janshoff, W. P. Ulrich, M. Sieber, and H. J. Galla. Impedance analysis of supported lipid bilayer membranes: a scrutiny of different preparation techniques. *Biochimica et Biophysica Acta (BBA) - Biomembranes*, 1279(2):169–180, Mar 1996.

[65] C. Ludwig. Diffusion zwischen ungleich erwärmten orten gleich zusammengesetzter lösungen. *Sitzungsberichte der Kaiserlichen Akademie der Wissenschaften: Mathematisch-Naturwissenschaftliche Klasse*, 20:539, 1856.

[66] S. Duhr and D. Braun. Thermophoretic depletion follows boltzmann distribution. *Physical Review Letters*, 96(16):168301, Apr 2006.

[67] M. Jerabek-Willemsen, C. J. Wienken, D. Braun, P. Baaske, and S. Duhr. Molecular interaction studies using microscale thermophoresis. *ASSAY and Drug Development Technologies*, 9(4):342–353, Aug 2011.

[68] D. L. Fortin, T. W. Dunn, A. Fedorchak, D. Allen, R. Montpetit, M. R. Banghart, D. Trauner, J. P. Adelman, and R. H. Kramer. Optogenetic photochemical control of designer k+ channels in mammalian neurons. *Journal of Neurophysiology*, 106(1):488–496, Jul 2011.

[69] S. C. Gill and P. H. von Hippel. Calculation of protein extinction coefficients from amino acid sequence data. *Analytical Biochemistry*, 182(2):319–326, Nov 1989.

[70] A. Mourot, M. A. Kienzler, M. R. Banghart, T. Fehrentz, F. M. E. Huber, M. Stein, R. H. Kramer, and D. Trauner. Tuning photochromic ion channel blockers. *ACS Chemical Neuroscience*, 2(9):536–543, Sep 2011.

[71] M. R. Banghart, A. Mourot, D. L. Fortin, J. Z. Yao, R. H. Kramer, and D. Trauner. Photochromic blockers of voltage-gated potassium channels. *Angewandte Chemie International Edition*, 48(48):9097–9101, Nov 2009.

[72] J. J. Chambers, M. R. Banghart, D. Trauner, and R. H. Kramer. Light-induced depolarization of neurons using a modified shaker k+ channel and a molecular photoswitch. *Journal of Neurophysiology*, 96(5):2792–2796, Jul 2006.

[73] K. Ataka, F. Giess, W. Knoll, R. Naumann, S. Haber-Pohlmeier, B. Richter, and J. Heberle. Oriented attachment and membrane reconstitution of his-tagged cytochrome c oxidase to a gold electrode: In situ monitoring by surface-enhanced infrared absorption spectroscopy. *Journal of American Chemical Society*, 126:16199–16206, November 2004.

[74] P. Macheroux. *UV-Visible Spectroscopy as a Tool to Study Flavoproteins*. Springer-Verlag, Jul 1999.

[75] P. Cerletti. Properties of riboflavin phosphates. *Analytica Chimica Acta*, 20:243–250, Jan 1959.

[76] J. M. Christie, M. Salomon, K. Nozue, M. Wada, and W. R. Briggs. Lov (light, oxygen, or voltage) domains of the blue-light photoreceptor phototropin (nph1): Binding sites for the chromophore flavin mononucleotide. *Proceedings of the National Academy of Sciences*, 96(15):8779–8783, Jul 1999.

[77] M. Salomon, J. M. Christie, E. Knieb, U. Lempert, and W. R. Briggs. Photochemical and mutational analysis of the fmn-binding domains of the plant blue light receptor, phototropin. *Biochemistry*, 39(31):9401–9410, 2000.

[78] S. Raffelberg, A. Gutt, W. Gaertner, C. Mandalari, S. Abbruzzetti, C. Viappiani, and A. Losi. The amino acids surrounding the flavin 7a-methyl group determine the uva spectral features of a lov protein. *Biological Chemistry*, 394(11):1517–1528, 2013.

[79] M. Dittrich, P. L. Freddolino, and K. Schulten. When light falls in lov: A quantum mechanical/molecular mechanical study of photoexcitation in phot-lov1 of chlamydomonas reinhardtii. *The Journal of Physical Chemistry B*, 109(26):13006–13013, Jul 2005.

[80] T. Kottke, J. Heberle, D. Hehn, B. Dick, and P. Hegemann. Phot-lov1: Photocycle of a blue-light receptor domain from the green alga chlamydomonas reinhardtii.

Biophysical Journal, 84(2):1192–1201, Feb 2003.

[81] Y. Nakasone, T. Eitoku, D. Matsuoka, S. Tokutomi, and M. Terazima. Kinetic measurement of transient dimerization and dissociation reactions of arabidopsis phototropin 1 lov2 domain. *Biophysical Journal*, 91(2):645–653, Jul 2006.

[82] M. T. A. Alexandre, J. C. Arents, R. van Grondelle, K. J. Hellingwerf, and J. T. M. Kennis. A base-catalyzed mechanism for dark state recovery in the avena sativa phototropin-1 lov2 domain. *Biochemistry*, 46(11):3129–3137, Mar 2007.

[83] A. Moeglich, R. A. Ayers, and K. Moffat. Design and signaling mechanism of light-regulated histidine kinases. *Journal of Molecular Biology*, 385(5):1433–1444, Feb 2009.

[84] T. Bednarz, A. Losi, W. Gaertner, P. Hegemann, and J. Heberle. Functional variations among lov domains as revealed by ft-ir difference spectroscopy. *Photochemical & Photobiological Sciences*, 3(6):575–579, 2004.

[85] T. Iwata, D. Nozaki, S. Tokutomi, T. Kagawa, M. Wada, and H. Kandori. Light-induced structural changes in the lov2 domain of adiantum phytochrome3 studied by low-temperature ftir and uv-visible spectroscopy. *Biochemistry*, 42(27):8183–8191, Jul 2003.

[86] M. Banyay, M. Sarkar, and A. Graeslund. A library of ir bands of nucleic acids in solution. *Biophysical Chemistry*, 104:477–488, 2003.

[87] A. Barth. The infrared absorption of amino acid side chains. *Progress in Biophysics and Molecular Biology*, 74(3-5):141–173, Jan 2000.

[88] M. S. Hutson, U. Alexiev, S. V. Shilov, K. J. Wise, and M. S. Braiman. Evidence for a perturbation of arginine-82 in the bacteriorhodopsin photocycle from time-resolved infrared spectra. *Biochemistry*, 39(43):13189–13200, Oct 2000.

[89] C. Kotting, A. Kallenbach, Y. Suveyzdis, A. Wittinghofer, and K. Gerwert. The gap arginine finger movement into the catalytic site of ras increases the activation entropy. *Proceedings of the National Academy of Sciences*, 105(17):6260–6265, Apr 2008.

[90] S. Y. Venyaminov and N. N. Kalnin. Quantitative ir spectrophotometry of peptide compounds in water (h2o) solutions. i. spectral parameters of amino acid residue absorption bands. *Biopolymers*, 30(13-14):1243–1257, 1990.

[91] H. Takeuchi, H. Murata, and I. Harada. Interaction of adenosine 5'-triphosphate with mg2+: vibrational study of coordination sites by use of 18o-labeled triphosphates. *Journal of the American Chemical Society*, 110(2):392–397, Jan 1988.

[92] A. Barth, W. Mäntele, and W. Kreutz. Infrared spectroscopic signals arising from ligand binding and conformational changes in the catalytic cycle of sarcoplasmic

reticulum calcium atpase. *Biochimica et Biophysica Acta (BBA) - Bioenergetics*, 1057(1):115–123, 1991.

[93] F. I. Valiyaveetil, Y. Zhou, and R. MacKinnon. Lipids in the structure, folding, and function of the kcsa k + channel. *Biochemistry*, 41(35):10771–10777, Sep 2002.

[94] K. Ataka, P. Hegemann, and J. Heberle. Vibrational spectroscopy of an algal phot-lov1 domain probes the molecular changes associated with blue-light reception. *Biophysical Journal*, 84(1):466–474, Jan 2003.

[95] S.-Y. Hou, E. G. Govorunova, M. Ntefidou, C. E. Lane, E. N. Spudich, O. A. Sineshchekov, and J. L. Spudich. Diversity of chlamydomonas channelrhodopsins. *Photochemistry and Photobiology*, 88(1):119–128, Nov 2011.

[96] O. A. Sineshchekov, E. G. Govorunova, J. Wang, H. Li, and J. L. Spudich. Intramolecular proton transfer in channelrhodopsins. *Biophysical Journal*, 104(4):807–817, Feb 2013.

[97] T. Althaus, W. Eisfeld, R. Lohrmann, and M. Stockburger. Application of raman spectroscopy to retinal proteins. *Isr. J. Chem.*, 35(3-4):227–251, 1995.

[98] N. A. Nevskaya and Y. N. Chirgadze. Infrared spectra and resonance interactions of amide-i and ii vibrations of alpha-helix. *Biopolymers*, 15(4):637–648, Apr 1976.

[99] E.-L. Karjalainen and A. Barth. Vibrational coupling between helices influences the amide i infrared absorption of proteins: Application to bacteriorhodopsin and rhodopsin. *The Journal of Physical Chemistry B*, 116(15):4448–4456, Apr 2012.

[100] J. F. Hunt, T. N. Earnest, O. Bousché, K. Kalghatgi, K. Reilly, C. Horváth, K. J. Rothschild, and D. M. Engelman. A biophysical study of integral membrane protein folding. *Biochemistry*, 36(49):15156–15176, Dec 1997.

Appendix

Table A.1: Table of standard amino acids with abbreviations

Amino Acid	3-letters Code	1-letter Code
Alanine	Ala	A
Arginine	Arg	R
Asparagine	Asn	N
Aspartic acid	Asp	D
Cysteine	Cys	C
Glutamine	Gln	Q
Glutamic acid	Glu	E
Glycine	Gly	G
Histidine	His	H
Isoleucine	Ile	I
Leucine	Leu	L
Lysine	Lys	K
Methionine	Met	M
Phenylalanine	Phe	F
Proline	Pro	P
Serine	Ser	S
Threonine	Thr	T
Tryptophan	Trp	W
Tyrosine	Tyr	Y
Valine	Val	V

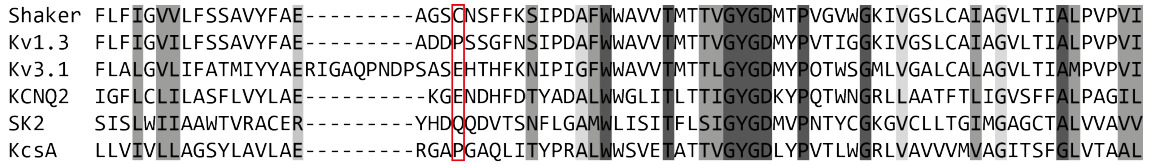

Figure A.1: KcsA alignment with other potassium channels like shaker (*Drosophila melanogaster*), Kv1.3, Kv3.1, KCNQ2 (voltage-gated) and SK2(Ca^{2+}-gated). Conserved amino acids are marked with a grey background. The brightness of the color corresponds to how essential the amino acid is for the function of the channel. The darker the background the more crucial is the amino acid. The red box make the homolog amino acids with the one of Shaker that was replaced by Banghart et al. 2004 to engineer a light sensitive potassium channel with the light switch MAQ, called SPARK

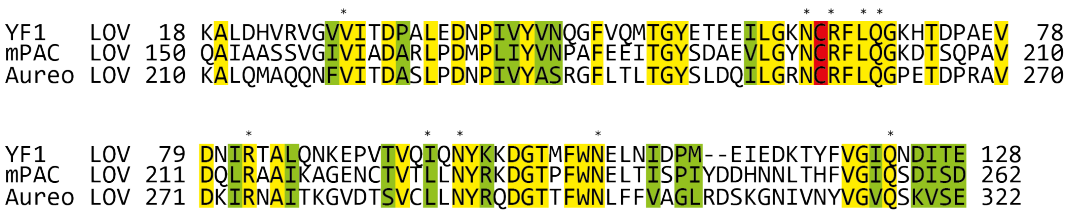

Figure A.2: Alignment of the LOV domains of YF1 (Ytva LOV domain from *Bacillus subtilis*), mPAC (*Microcoleus chthonoplastes*) and Aureochrome 1 (*Vaucheria frigida*). The alignment is based on the BLAST algorithm. Fully conserved residues are marked with yellow background and functionally conserved residues are marked with a green one. The residues marked with a star are the one essential for FMN binding. The reactive cysteine is shown with a red background.

Figure A.3: Sequence alignment of aureochrome 1 with GCN4. Sequence alignment of the bZIP domains of aureochrome 1 from Vaucheria frigida and of GCN4 from S. cerevisiae. The red marked amino acids are involved in the binding of the protein to the ribose phosphate backbone of the target DNA. The blue marked residues interact with the nucleotides [40]. The yellow marked arginines interact with both. The sequences show the typical N-X7-R/K motive with the hepta-repeat of leucines (colored in green) positioned exactly nine amino acids toward the C-terminus [39].

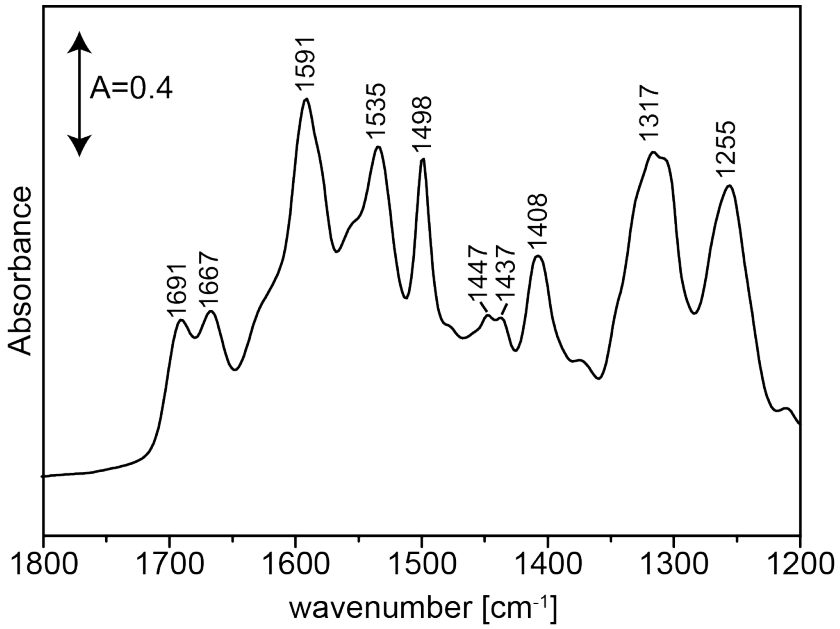

Figure A.4: BzAQ absorption spectrum in the range between 1200 and 1800 wavenumbers. The photoswitch was dried on an ATR cell.

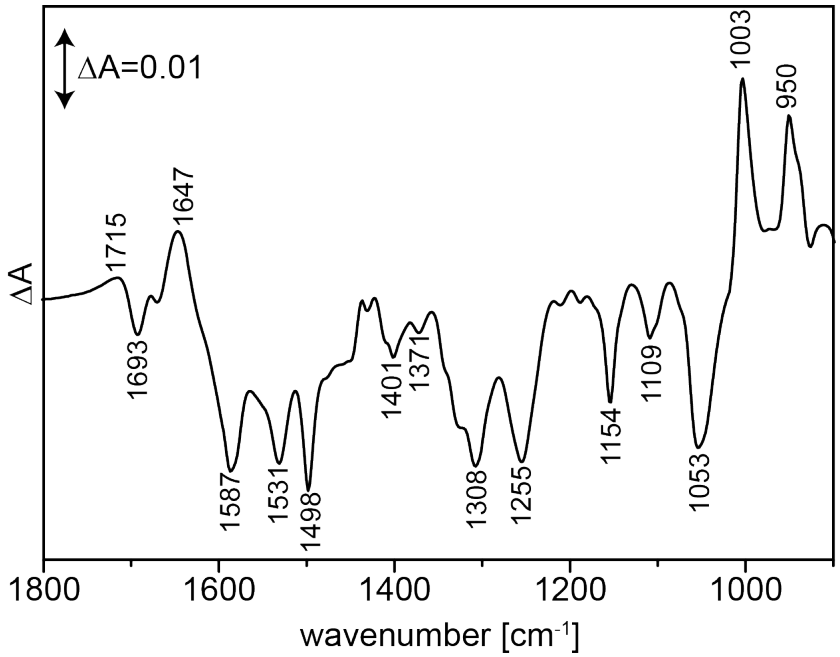

Figure A.5: Light-induced difference spectrum of BzAQ dried on an ATR cell. The background was measured under illumination with 505 nm (LED), the sample spectrum under illumination with 380 nm (LED).

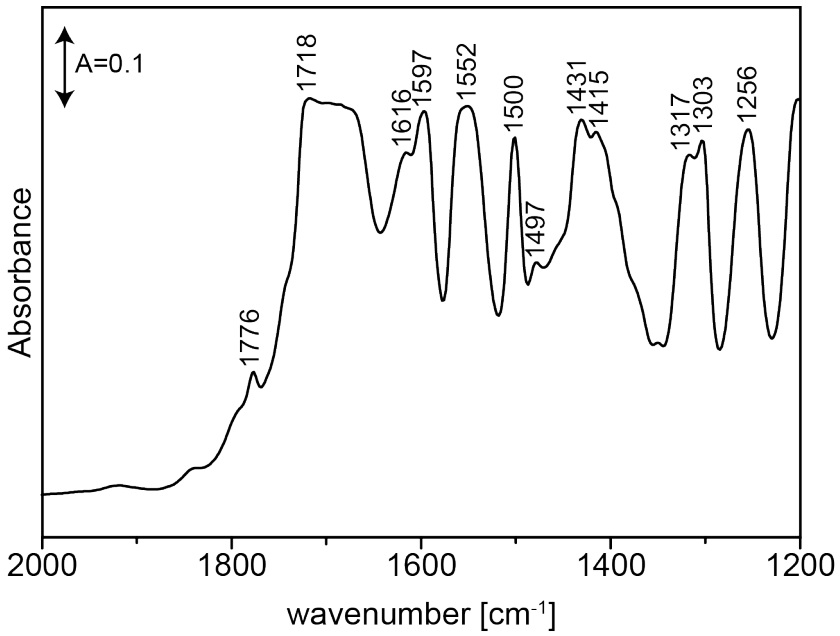

Figure A.6: MAQ absorption spectrum in the range between 1200 and 2000 wavenumbers. The photoswitch was dried on BaF_2 windows and measured in transmission.

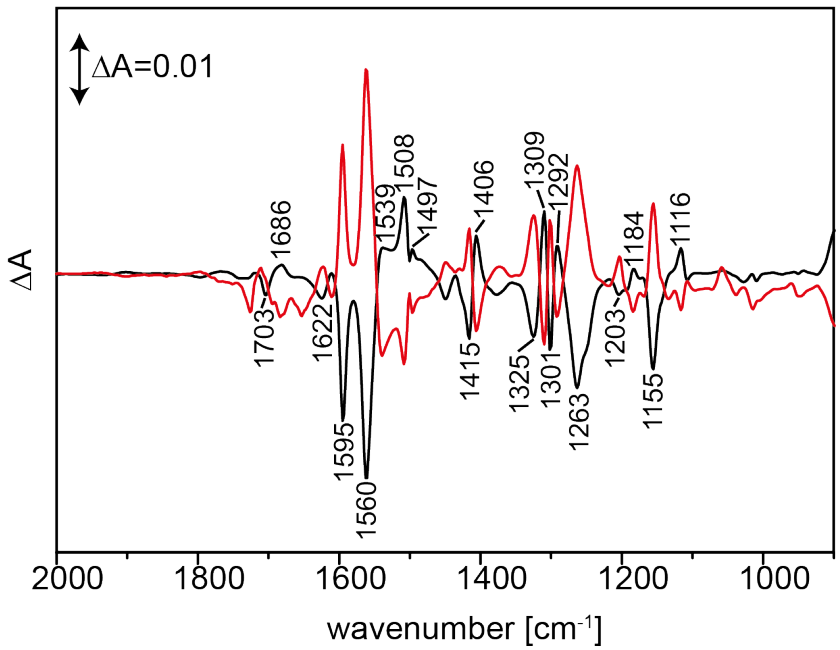

Figure A.7: Light-induced difference spectra of MAQ dried on a BaF_2 window measured in transmission. The black curve shows the 505-380 nm and the red one the 380-505 nm difference spectrum. Illumination was performed with two LEDs.

Further Projects

In collaboration with Vera Muders from the lab of Dr. Ramona Schlesinger of the Freie Universität Berlin and with Axel Baumann from the group of Professor Jörg Fitter from the Forschungszentrum Jülich GmbH I worked on two further projects that will be mentioned shortly in the this chapter. Part of this work was already published, while the other is in preparation.

V. Muders, **S. Kerruth**, V. A. Lórenz-Fonfría Ataka, D. Frey, I. Schlichting and J. Heberle.
Resonance Raman and FTIR spectroscopic characterization of the closed and open states of channelrhodopsin-1. *FEBS letters*, 2014, 588(14), 2301-2306. DOI:10.1016/j.febslet.2014.05.019

A. Baumann and **S. Kerruth**, J. Fitter, G. Büldt, J. Heberle, R. Schlesinger and K. Ataka
Membrane protein insertion and folding into a solid-supported lipid scaffold during cell free expression: *in-situ* observation by Surface Enhanced Infrared Absorption Spectroscopy. in preparation.

B.1 Channelrhodopsin-1

Channelrhodopsin-1 from *Chlamydomonas augustae* (*Ca*ChR1) is a light-activated cation channel and a promising optogenetic tool [95]. The protein consists of seven transmembrane α-helices that enclose the retinal chromophore. Retinal is covalently bound to the side chain of K303 via a Schiff base. Absorption of a green photon induces a photocycle with several intermediates. Upon illumination, an early P_1^{580} intermediate arises, followed by a long-lasting biphasic P_2^{380} intermediate and small contributions of an intermediate at 590 nm (similar to the O-state of bacteriorhodopsin) [96]. A red-shifted intermediate comparable to the conductive P_3^{520} intermediate of ChR2 from *Chlamydomonas reinhartti* (*Cr*ChR2), was not detected. The lifetime of the P_2^{380} state of *Ca*ChR1 correlates with the lifetime of its passive channel current and lies in the ms range. Consequently the P_2^{380} intermediate represents the conductive state of *Ca*ChR1. To elucidate the configuration of the retinal chromophore in the ground/dark and conductive state we performed resonance Raman spectroscopy. The Raman effect describes the inelastic scattering of light. Energy differences of incoming and scattered photons correspond to the frequency of vibrational states. If the energy of incoming light matches the transition to the first excited state, the intensity of the Raman signal is enhanced (up to a factor of 10^5).

The resonance Raman spectrum of the dark state was dominated by the four coupled C=C double bond vibrations of the retinal, called ethylenic stretch. Generally, most of the Raman and infrared intensity concentrate in the in-phase mode [97]. This mode appears at 1532 cm^{-1} for the dark state of *Ca*ChR1 (fig. B.1A). However, the shape of the band is not symmetric. The second derivative revealed three contributions at 1548, 1533 and 1525 cm^{-1}. Two of these bands were assigned to all-*trans* and 13-*cis* retinal and are shown in figure B.1. The band area of these fitted peaks together with retinal extraction followed by high pressure liquid chromatography (HPLC) demonstrated that the isomeric ratio of all-*trans* to 13-*cis* of solubilized *Ca*ChR1 in the dark state was with 70:30 identical to *Cr*ChR2. Critical frequency shifts in the retinal vibrations are identified in the Raman spectrum upon transition to the open (conductive P_2^{380}) state caused by all-*trans* to 13-*cis* isomerization. The C-N stretching vibration of the protonated and deprotonated Schiff base were assigned via H/D exchange and showed a shift from 1646 to 1610 cm^{-1} from the ground to the open state. Thus, resonance Raman showed that in the conductive state P_2^{380} the retinal is in its 13-*cis* conformation and deprotonated.

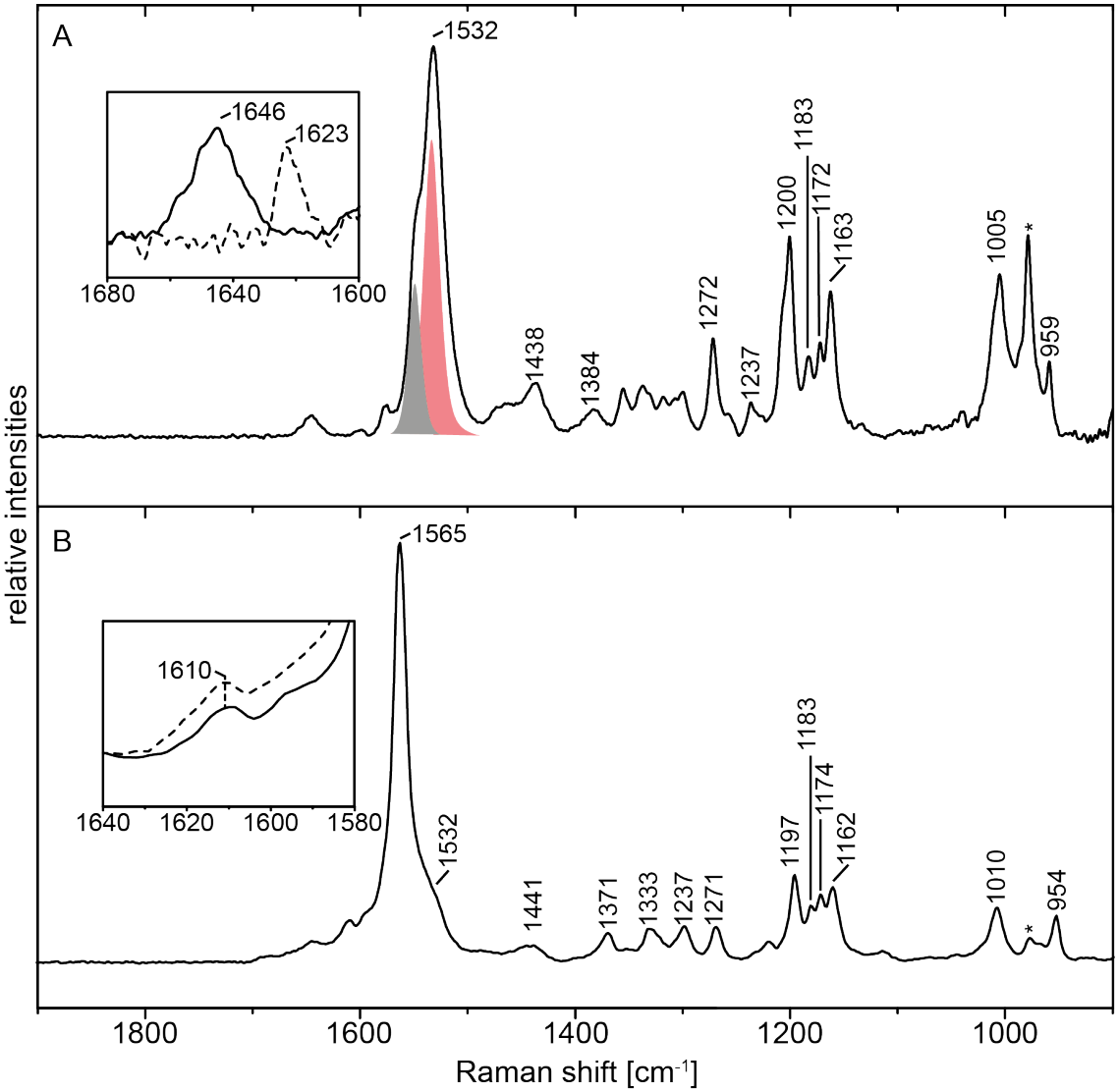

Figure B.1: Resonance Raman spectra of Channelrhodopsin-1 ground state (upper spectrum) and in the conductive state P_2^{380} (lower spectrum). The dark state was probed under pre-resonant conditions using Raman excitation at 647 nm. Raman spectrum of the P_2^{380} intermediate was obtained under photo-stationary conditions by illumination with 532 nm, probing with the laser line at 413 nm. The two filled bands under the ethylenic stretch mode around 1530 cm^{-1} of the ground state represents the fits to the all-*trans* (red) and 13-*cis* (grey) retinal vibration. The fitted bands have 50 % Lorentzian and 50 % Gaussian character and the peak areas correspond to 70 % all-*trans* and 30 % 13-*cis*. The insets show the zoom-out of the frequency regions of 1680-1600 cm^{-1} and 1640-1580 cm^{-1}, respectively. The C=N-H vibrational band of the retinal Schiff base in the ground state at 1646 cm^{-1} experienced a downshift of 23 cm^{-1} upon exchange of H_2O (continuous line) to D_2O (dashed line), while the deprotonated Schiff base vibration at 1610 cm^{-1} is not influenced by the H/D exchange. The band at 979 cm^{-1} (labeled by an asterisk *) is due to the ν_1 vibration of Na_2SO_4 that was added as an internal frequency standard.

B.2 Bacteriorhodopsin folding into nanodiscs

The correct insertion, folding and assembly of functional proteins in biological membranes are essential for many cellular functions. To study the folding of the membrane protein bacteriorhodopsin (bR) into artificial lipid bilayers during cell-free protein expression we used surface-enhanced infrared absorption spectroscopy (SEIRAS). This novel method exclusively observed phenomena on the gold surface where the folding into the lipid bilayer takes place, while the reactions in the bulk are faded out. Hence vibrational bands provided structural information of the folding dynamics at atomic/molecular level. Nanodiscs (ND), which serve as a well-defined lipidic folding milieu for membrane proteins, were attached to the gold surface, while cell-free expression of bR takes place in the bulk solution. Analysis of the obtained spectra reveals three phases at the lipid bilayer after gene transcription and translation have been initiated: (i) pre-conditioning period, a cleaning phase; (ii) phase I, first folding stage, in which newly synthesized protein is inserted into the nanodiscs and gradually forms secondary structures; (iii) phase II, second folding stage in which the protein adopts its tertiary structure.

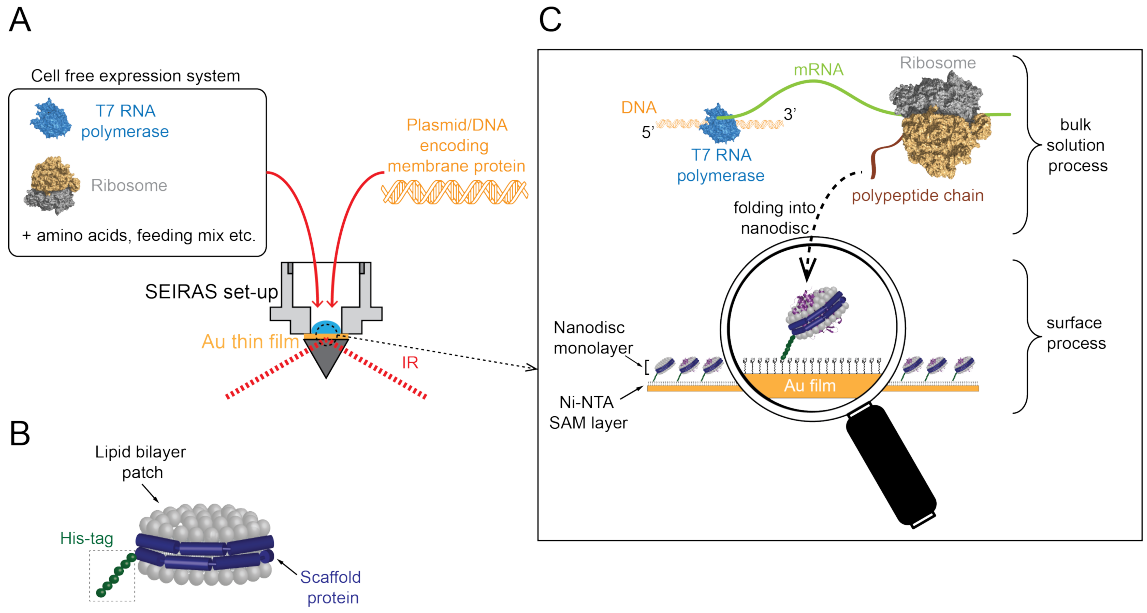

Figure B.2: Outline of the experimental concept. (a) SEIRAS optical cell with a droplet of the cell-free expression system to produce bacterioopsin (bO) after addition of the encoding DNA. (b) Nanodisc as biomimetic membrane comprising a phospholipid bilayer (DMPC) contained by two amphiphilic membrane scaffold protein (MSP). The latter carries an N-terminal His-tag to bind the nanodiscs to a Ni-NTA modified surface. (c) In vitro transcription and translation synthesizing the polypeptide, which inserts into the surface-tethered monolayer of nanodiscs. As the surface enhancement decays exponentially with the distance with an effective length of about 10 nm, processes are exclusively probed by SEIRAS that occur at and within the nanodisc monolayer.

The time-resolved SEIRA spectra in figure B.3 reflects these three phases. After the transcription/translation process was initiated by plasmid injection, pre-adsorbed species were removed from the nanodisc surface (negative bands at 1660 and 1550 cm^{-1} in fig. B.3A). These bands were assigned to amide I and II vibrations of peptide bonds. This pre-phase was identified as "cleaning´´ phase, during which the ND surface is prepared for insertion of the nascent polypetide chain.

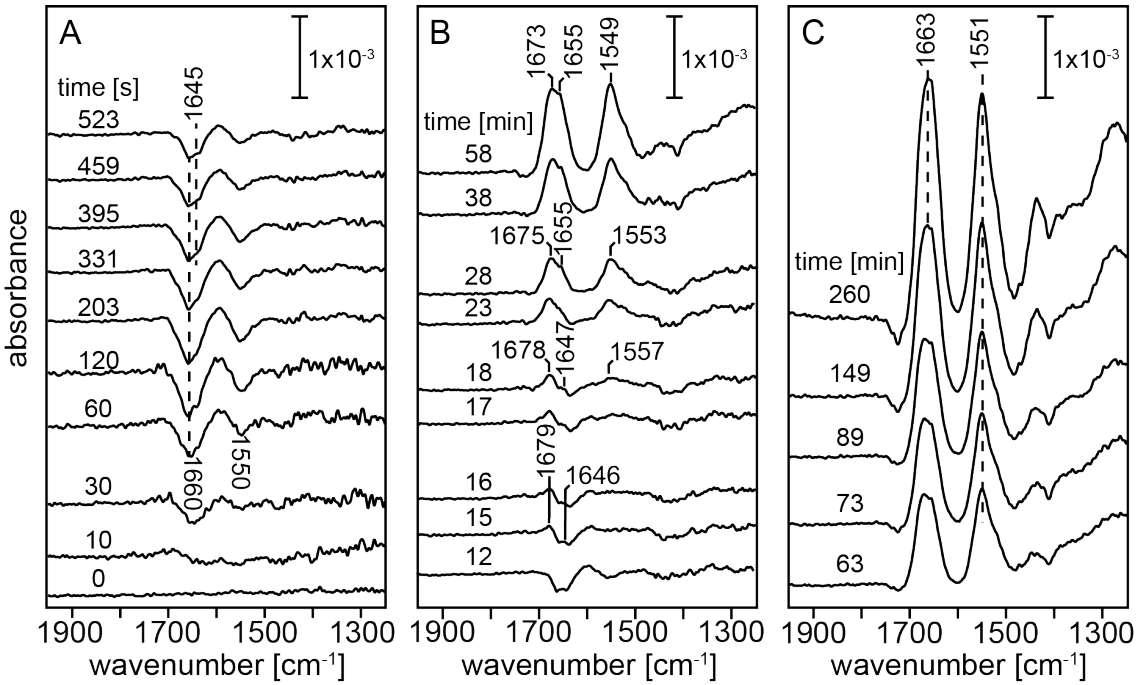

Figure B.3: Time-resolved SEIRA spectra recorded after triggering transcription/translation (time = 0 s) by adding the plasmid encoding for bacterioopsin (bO). In each spectrum, positive peaks represent species adsorbed (inserted) to (in) the surface tethered nanodiscs, while negative peaks represent species removed from the nanodisc surface. A: Pre-conditioning period (0 to 10 minutes). B: Phase I (10 to 60 minutes): insertion and folding of newly synthesized bR were visible by appearance of positive peaks of amide I (1645-1655, 1679-1673 cm^{-1}) and amide II (1557-1549 cm^{-1}). C: Phase II (60 minutes to 5 hours): the frequencies of peak maxima of amide I/II of the newly synthesized bR remained constant at 1663 and 1551 cm^{-1}, respectively. However, the amide I band width decreased with time.

After about 12 min the negative bands were overlapped by positive bands at 1679, 1646, and 1557 cm^{-1} (fig. B.3B). These bands correspond to the amide bands of random coils [59]. Within the following 45 min these bands increased in intensity and shifted in their absorption maxima. The bands at 1679 and 1557 cm^{-1} shifted to lower wavenumbers, while the one at 1646 cm^{-1} was up-shifted. Due to the fact that frequencies of amide vibrations depend on the secondary structure, an increase in the amide band intensity reflects a continuous insertion of polypeptide into the nanodiscs, while the band shift was indicative for secondary structure formation of the protein backbone [59]. Thus,

random structures are converted in α-helices.
In phase II the broad band with the absorption maximum at 1657 and 1673 cm^{-1} sharpened over time and the maximum shifted to 1663 cm^{-1} (fig. B.3 C). The latter frequency is characteristic for polytopic α-helical proteins [98]. The frequency up-shift by 5 cm^{-1} has been explained by vibrational coupling among helices [99]. This result suggested that α-helices and turn structures are converted into a compact structure of a bundle of α-helices, confirming that the tertiary structure of inserted polypeptide has been established during phase II and the folding process has been completed.
Further experiments with the cofactor retinal showed that folding was accelerated, when the chromophore was present in the lipid bilayer. On the other hand, when cell-free expression was performed without retinal in the bulk solution, no folded peptide was detected at the lipid bilayer at all. Therefore accessibility to retinal during synthesis was found essential to influence induction of α-helix formation, consequently for insertion and folding of functional bR and for the kinetics of the entire process.
From our data a model for protein folding and insertion was derived: Before addition of the plasmid, the nanodisc monolayer is covered by non specifically bound protein of the *E. coli* cell extract. As DNA encoding for bacterioopsin is added, transcription and translation are initiated. Subsequently, the nascent polypeptide chain approaches the lipid bilayer surface. Pre-adsorbed species are removed from the surface and the synthesized peptide inserts into the membrane. During insertion in phase I, the peptide folds into individual transmembrane α-helices. In phase II, these α-helices interact with each other, leading to folding of the final two helices G and F and formation of tertiary structure [100]. Retinal binds to apo-protein and fully functional bR is formed. Kinetics of tertiary structure formation is enhanced when retinal is per-bound to the lipid bilayer.

Acknowledgements

In the end I want to thank all the people who supported me during my Ph.D. and made this thesis possible.

Firstly, I wish to thank my advisor Professor Joachim Heberle for introducing me to the exciting field of biophysics and giving me the opportunity to work on such an interesting topic. I would like to thank him for all the fruitful discussions and his constant trust in my scientific skills. I would like to thank Professor Enrica Bordignon for revising my thesis and serving in my Ph.D. committee.

I am grateful to Dr. Kenichi Ataka for supporting my during the almost seven years of my Bachelor, Master, and PhD thesis and introducing me to several techniques, in particular SEIRAS and impedance spectroscopy. Without the weekly meetings where we discussed my research, I would have had lost my way during these years.

All of the works that are presented in this thesis are based on collaborations. I would like to thank the group of Professor Dirk Trauner at the Ludwig-Maximilians-Univeristät in Munich. In particular Dr. Martin Sumser for providing me with the KcsA clone as well as all the various photoswitches. Thanks also to the Max Planck Institut in Heidelberg and to Professor Ilme Schlichting and Dr. Daniel Frey, our collaborations on the aureochrome 1 project. I would specially like to mention Elisabeth Hartman for sending me thousands of milligrams of perfectly purified sample. Lastly, I am also grateful to Professor Wolfgang Gärtner and Dr. Sarah Raffelberg for providing us the mPAC clone and mentoring me on the expression process as well as for constant support.

Two other very fruitful collaborations that are only mentioned shortly in this thesis were performed with Axel Bauman from the group of Professor Jörg Fitter from the Forschungszentrum Jülich GmbH and with Vera Muders from the group of Dr. Ramona Schlesinger from the Freie Universität Berlin. Axel Bauman exposed me to his facinating work on nanodiscs and cell-free expression systems. It was a honor to work with him and I find myself fortunate to become his close friend during our collaboration. Together with Vera Muders we performed Resonance Raman Spectroscopy on Channelrhodopsin-1. I am grateful for the successful collaboration. It was a pleasure to work with her on this exciting optogenetic tool.

A huge “Thank you!” goes to all my colleagues at the Freie Universität Berlin. Each one of them created a working atmosphere that was inspiring and at the same time fun. I am very grateful to have so many amazing people around me every day. Special mention goes to Tom Resler, who has been much more than a colleague. We have shared an office for a long time, and I would like to thank him all my heart for induring my annoying

questions as well as my clumsiness during the last years. I also would like thank Ingrid Wallat for her excellent technical support and her help on any kind of questions related to chemicals or infrastructure, and Dr. Sven Stripp for proofreadings and helpful advices on my thesis. To all the others (I cannot write all names here): I hope you know how much you have helped me to finish this thesis with all your special skills.

During the last five years in Berlin I have met a lot of people and few of them have become really good friends. Xenia, Jens, Annemarie, Vera, and Nils, I would want you to know that you are not forgotten. I thank you for all the nice evenings that we shared together and for patiently listening to all my problems.

Finally, I would like to thank my family. My parents have constantly supported me during all these years and have never stopped believing in me. Without their love and constant advice, I would have never made it so far.

Statement of authenticity

Hiermit erkläre ich, dass ich die vorliegende schriftliche Arbeit in allen Teilen selbständig verfasst und keine anderen als die angegebenen Quellen und Hilfsmittel (einschliesslich elektronischer Medien und Online-Ressourcen) verwendet habe.

Silke Kerruth
Berlin November 24, 2014